SANDIA REPORT

SAND2014-3292
Unlimited Release
Printed March 2014

Experiments to Populate and Validate a Processing Model for Polyurethane Foam: BKC 44306 PMDI-10

Lisa Mondy, Rekha Rao, Bion Shelden, Melissa Soehnel, Timothy O'Hern, Anne Grillet, Mathew Celina, Nicholas Wyatt, Edward Russick, Stephen Bauer, Michael Hileman, Alexander Urquhart, Kyle Thompson, David Smith

Prepared by
Sandia National Laboratories
Albuquerque, New Mexico 87185 and Livermore, California 94550

Sandia National Laboratories is a multi-program laboratory managed and operated by Sandia Corporation, a wholly owned subsidiary of Lockheed Martin Corporation, for the U.S. Department of Energy's National Nuclear Security Administration under contract DE-AC04-94AL85000.

Issued by Sandia National Laboratories, operated for the United States Department of Energy by Sandia Corporation.

Available to DOE and DOE contractors from
U.S. Department of Energy
Office of Scientific and Technical Information
P.O. Box 62
Oak Ridge, TN 37831

Telephone: (865) 576-8401
Facsimile: (865) 576-5728
E-Mail: reports@adonis.osti.gov
Online ordering: http://www.osti.gov/bridge

Available to the public from
U.S. Department of Commerce
National Technical Information Service
5285 Port Royal Rd.
Springfield, VA 22161

Telephone: (800) 553-6847
Facsimile: (703) 605-6900
E-Mail: orders@ntis.fedworld.gov
Online order: http://www.ntis.gov/help/ordermethods.asp?loc=7-4-0#online

SAND2014-3292
Unlimited Release
Printed March 2014

Experiments to Populate and Validate a Processing Model for Polyurethane Foam: BKC 44306 PMDI-10

Lisa Mondy
Thermal/ Fluid Experimental Sciences

Rekha Rao
Fluid Sciences & Engineering

Bion Shelden, Melissa Soehnel, Timothy O'Hern, Anne Grillet
Thermal/ Fluid Experimental Sciences

Mathew Celina
Materials Characterization & Performance

Nicholas Wyatt
Organic Materials Science

Edward Russick
Packaging & Polymer Processing

Stephen Bauer, Michael Hileman, Alexander Urquhart
Geomechanics

Kyle Thompson
Radiography & Modal Testing

David M. Smith
Secure Systems & Embedded Software

Sandia National Laboratories
P.O. Box 5800
Albuquerque, New Mexico 87185-MS0346

Abstract

We are developing computational models to elucidate the expansion and dynamic filling process of a polyurethane foam, PMDI. The polyurethane of interest is chemically blown, where carbon dioxide is produced via the reaction of water, the blowing agent, and isocyanate. The isocyanate also reacts with polyol in a competing reaction, which produces the polymer. Here we detail the experiments needed to populate a processing model and provide parameters for the model based on these experiments. The model entails solving the conservation equations, including the equations of motion, an energy balance, and two rate equations for the polymerization and foaming reactions, following a simplified mathematical formalism that decouples these two reactions. Parameters for the polymerization kinetics model are reported based on infrared spectrophotometry. Parameters describing the gas generating reaction are reported based on measurements of volume, temperature and pressure evolution with time. A foam rheology model is proposed and parameters determined through steady-shear and oscillatory tests. Heat of reaction and heat capacity are determined through differential scanning calorimetry. Thermal conductivity of the foam as a function of density is measured using a transient method based on the theory of the transient plane source technique. Finally, density variations of the resulting solid foam in several simple geometries are directly measured by sectioning and sampling mass, as well as through x-ray computed tomography. These density measurements will be useful for model validation once the complete model is implemented in an engineering code.

ACKNOWLEDGMENTS

The authors would like to acknowledge helpful discussions with Heather Boldt (2153), Christine Mitchell and Joe Fonseca (2128), and personnel at National Nuclear Security Administration's Kansas City Plant, Operated by Honeywell Federal Manufacturing & Technologies, LLC, including James Mahoney, James Tinsley, Audrey Chase, and Vinita Chhahira.

CONTENTS

FIGURES

TABLES

NOMENCLATURE

a_T	time shift factor
ATR	attenuated total reflection
C_p	heat capacity per unit mass
CO_2	carbon dioxide
DSC	differential scanning calorimeter
E	activation energy
$\boldsymbol{g}$	gravity constant
G'	storage modulus
G''	loss modulus
ΔH_{rxn}	heat of reaction
k	thermal conductivity
KCP	National Nuclear Security Administration's Kansas City Plant, Operated by Honeywell Federal Manufacturing & Technologies, LLC
IR	infrared
n	number of moles
P	pressure
R	gas constant
R-component	resin part of the foam kit
PMDI	urethane foam based on polymethylene diisocyanate
SEM	Scanning electron microscopy
t	time
T	absolute temperature
T-component	curative part of the foam kit
u	uncertainty
v	mass averaged velocity
V	volume
Y	liquid mass fraction
α	extent of the gas producing reaction
κ	foam bulk viscosity
η	foam (apparent Newtonian) viscosity
ξ	extent of polymerization reaction
ρ	density of the foam
$\underline{\underline{\boldsymbol{\tau}}}$	fluid stress tensor
ϕ	gas fraction
ω	angular frequency

1. INTRODUCTION

Polyurethanes are chemically blown foams that begin as two-part mixtures, with polyisocyanate in one part (what we will call the curative) and polyol, water, surfactant and catalyst in the other (what we will call the resin). When mixed together, several competing reactions occur simultaneously, the most important of which are the polymerization reaction and the foaming reaction (Figure 1). Polymerization occurs via condensation reaction of polyisocyanate and polyol to form a crosslinked polyurethane. The foaming reaction occurs between polyisocyanate and water, forming carbamic acid which then decomposes to form carbon dioxide (CO_2) and an amine group [Tesser 2004]. The carbon dioxide is a gas, which is responsible for blowing the polymer into a foam.

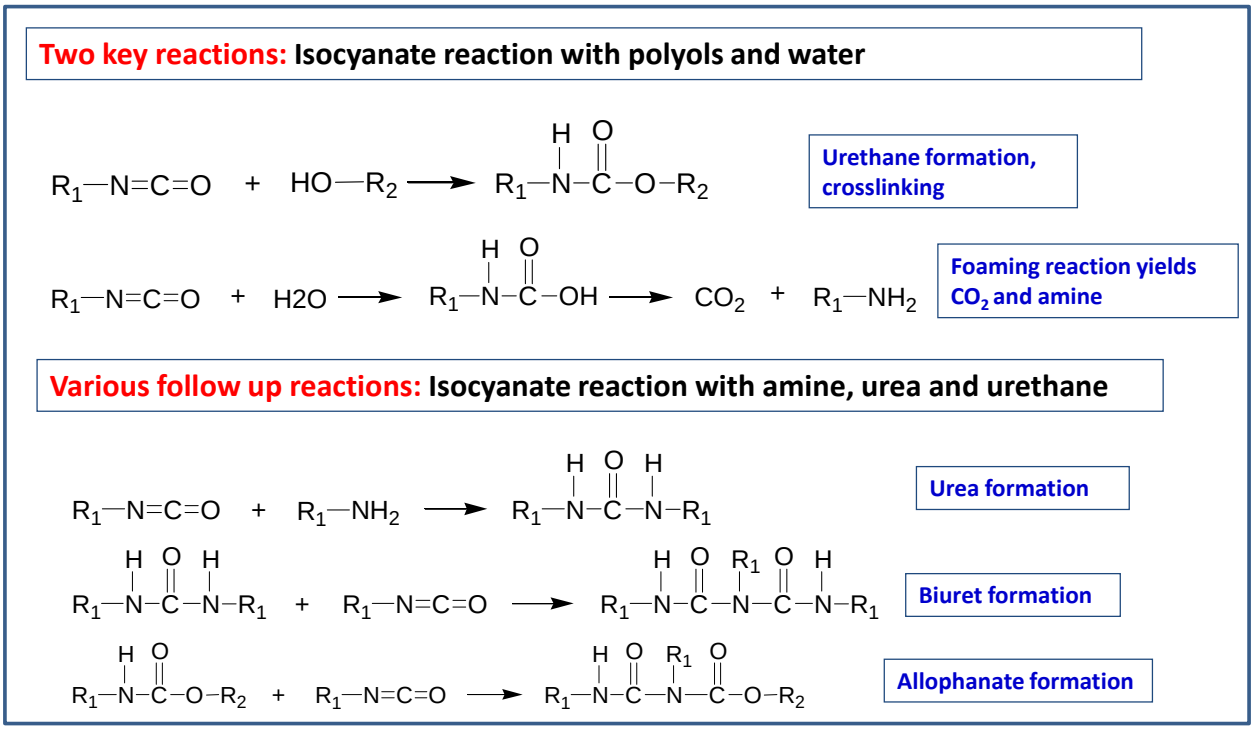

Figure 1. Chemical reactions involved in producing solid polyurethane foam

Rao and coworkers developed an engineering model combining the equations of motion, an energy balance, a density model to represent the foam blowing reaction, and a rate equation for the polymerization reaction [Rao et al. 2010]. This was combined with a level set method to track the location of the free surface as it evolves in time. The equations describing the kinetics of the polymerization reaction were of the form of condensation chemistry and were populated

through micro-attenuated total reflection (ATR) infrared (IR) spectroscopy measurements. Unfortunately, no IR peak is a fingerprint of the gas-forming reaction. Therefore, the blowing reaction effects were approximated through an empirical, temperature-dependent, equation for the density as a function of time, following Seo et al. [2003]. However, this approach leads to prediction of a constant density throughout the foam at any one time.

The original model [Rao et al. 2010] was based on the kinetics and rheology of PMDI-4, nominally a 4-pcf (-lb/ft^3) free rise foam in Series BKC 44307, used for encapsulating electronics. The structural foam Series BKC 44306 contains a faster acting catalyst and no prepolymer in the resin. The differences are enough to warrant characterization of the material to obtain model parameters. In addition, the model has recently been extended to predict density through tracking the gas-forming reaction. Improved parameters were needed, as well as validation data, to continue improvement of this model.

As will be shown, collecting data on this complex system, with chemical reactions inducing phase changes (both liquid to gas and liquid to solid), heterogeneous microstructure of the foam, and temperature changes from the exothermic reactions, is challenging. To simply measure changes as a function of time and temperature to create purely empirical models would not allow the flexibility and accuracy needed in a process model to predict the manufacture of a wide variety of foamed parts. The model, based on the physics as we know them, is difficult to parameterize, but it is hoped that it will allow a robust engineering process model to be developed and refined. The purpose here is to describe the experiments to date used to determine parameters for the current processing model, as well as to provide data and knowledge necessary to continue to refine the model. The model described here only applies to the foam during the expansion phase. Further refinement in the kinetic and rheology models are needed to predict the development of cure stresses after the foam expansion has stopped; and this will not be addressed here except cursorily.

In the next section the model equations will be briefly outlined in order to describe the needed parameters. The third section will discuss measurements of the reactions rates for the two important reactions and evidence that they can be decoupled as approximated in the model.

Rheology is the topic of the fourth section, where we will describe the complexities that are observed and suggest parameters for the foam viscosity in the current form of the model. Input to the energy equation is discussed in the fifth section, including the heat of reaction, heat capacity, and thermal conductivity, and their dependence (or lack of) on the foam density. Measurements of the final density of foam blown in two molds, a simple channel and a quality assurance geometry developed at the Kansas City Plant (KCP), is detailed in the sixth section, for use in validation of the model. The final section offers a summary, discussion, and suggestions for future work.

2. EQUATIONS

This section will describe the equations proposed to model foam filling. Improvements to the model are ongoing; however, this report will serve to document the best-fit parameters for the following set of equations obtained through experiments.

The continuity equation is written to emphasize the change in density as the source of foam velocity generation, where $\boldsymbol{v}$ is the mass averaged velocity and ρ is the foam mixture density and a function of the volume fraction of gas ϕ (equation 13):

$$\nabla \cdot \boldsymbol{v} = -\frac{1}{\rho}\left(\frac{\partial \rho}{\partial t} + \boldsymbol{v} \cdot \nabla \rho\right) \tag{1}$$

Conservation of momentum takes into account gradients in the fluid stress, $\underline{\underline{\boldsymbol{\tau}}}$, and pressure, p, as well as effects of gravity, $\boldsymbol{g}$:

$$\rho \frac{\partial \boldsymbol{v}}{\partial t} + \rho \boldsymbol{v} \cdot \nabla \boldsymbol{v} = \nabla \cdot \underline{\underline{\boldsymbol{\tau}}} - \nabla p + \rho \boldsymbol{g} \,. \tag{2}$$

The stress tensor, $\underline{\underline{\boldsymbol{\tau}}}$, Equation (3), has a generalized Newtonian shear viscosity, η, in addition to a generalized Newtonian bulk viscosity, κ. The bulk viscosity is associated with the facts that the divergence of the velocity field is non-zero and the flow is dilatational [Bird et al. 1960]. The bulk viscosity term produces only normal stresses and not shear stresses.

$$\underline{\underline{\boldsymbol{\tau}}} = \eta\left(\nabla \boldsymbol{v} + \nabla \boldsymbol{v}^t\right) - \left(\frac{2}{3}\eta - \kappa\right)(\nabla \cdot \boldsymbol{v})\underline{\underline{\boldsymbol{I}}} \,, \tag{3}$$

where $\left(\nabla \boldsymbol{v} + \nabla \boldsymbol{v}^t\right)$ is the shear rate and $\underline{\underline{\boldsymbol{I}}}$ is the identity matrix. The generalized Newtonian viscosity models imply that the viscosities vary with local fields, but retain a Newtonian form where stress is proportional to strain. Here, both η and κ are functions of temperature, degree of polymerization, and gas bubble volume fraction, as will be discussed later.

Because the process is nonisothermal, heat transfer effects must be followed as well. The full energy equation for compressible, nonisothermal flow (neglecting viscous dissipation) is:

$$\frac{\partial}{\partial t}\left(\rho C_v T\right) + \left(\nabla \bullet \rho C_v T \boldsymbol{v}\right) = \nabla \bullet \left(k \nabla T\right) - T(\partial P / \partial T)_P (\nabla \bullet \boldsymbol{v}) + \rho T \frac{DC_v}{Dt} + S_{rxn} \ , \tag{4}$$

where T is absolute temperature, C_v is the heat capacity per unit mass at constant volume, and k is thermal conductivity. The energy equation currently solved in Aria is a subset of the above, in which a constant ρ, C_p (the heat capacity per unit mass at constant pressure), and k are assumed. However, we will attempt to determine appropriate, variable properties, as discussed later, in anticipation of improvements to the model.

Heat is generated by the exothermic polymerization reaction (S_{rxn}):

$$S_{rxn} = \Delta H_{rxn} Y \rho \frac{d\xi}{dt}, \tag{5}$$

where ΔH_{rxn} is the heat of reaction (energy/mass), Y is the liquid mass fraction, ξ is the extent of the polymerization reaction and t is time. As will be shown in Section 5, the foaming reaction, although also exothermic, involves very little mass and contributes little to the total heat generation.

The extent of reaction for polymerization is written in the form of condensation chemistry [May 1988; Adolf 1996]:

$$\frac{d\xi}{dt} = k(1-\xi)^q (A + \xi^p) \tag{6}$$

$$k = k_0 e^{E_\xi / RT} \tag{7}$$

where k_o is the rate coefficient, E_ξ is the activation energy, R is the universal gas constant, and q and p are the orders of reaction. The chemical species used to represent ξ will be described in Section 3.2.

The extent of reaction of the gas producing reaction α, defined as the ratio of the number of moles of gas n_{CO2} to the maximum possible from stoichiometry, seems best described by a Michaelis-Menten reaction form [Levenspiel 1972]:

$$\frac{d\alpha}{dt} = \frac{NK(1-\alpha)^n}{(1-\alpha)^m + M} \tag{8}$$

$$K = A_1 e^{E_1/RT} \tag{9}$$

$$M = A_2 e^{E_2/RT} \tag{10}$$

where N is a time delay to approximate the time it takes for bubbles to nucleate:

$$N = 0.5(1 + \tanh(t - t_{nucleation})) \ . \tag{11}$$

Best fit parameters for the exponents n and m, as well as Arrhenius parameters and the characteristic time for nucleation will be given in Section 3.3.3.

Although side reactions enhance both polymerization and foaming reaction rates, the simplifications of equations 6 and 8 are convenient to implementation in a computational framework. Likewise, other forms for the reaction kinetics could produce comparable goodness-of-fit.

If one knows the rate of gas formation, one can then define the gas fraction ϕ and foam density ρ at any time.

$$\phi(t) = \frac{n_{CO_2} MW_{CO_2} / \rho_{CO_2}}{n_{CO_2} MW_{CO_2} / \rho_{CO_2} + V_{liquid}} \tag{12}$$

$$\rho(t) = (\rho_{CO_2} - \rho_{liquid})\phi(t) + \rho_{liquid} \tag{13}$$

Here the subscript *liquid* refers to the polymer phase. In the above equations, one can see the parameters needed to complete the model. In equation 3, we need the shear and bulk viscosity. We will assume η is a function of both the polymerizing continuous phase and ϕ. Rheology measurements will be presented in Section 4, for both a dry polyurethane system that does not foam, representing the polymerizing phase, and for the total foaming system. Our first approximation was to assume that the foam viscosity follows the Taylor-Mooney form derived from emulsion experiments, extrapolating the discontinuous phase viscosity to zero (for gas) [Prud'homme & Khan 1996]:

$$\eta = \eta_{cure} \exp\left(\frac{\phi}{1-\phi}\right) \quad , \tag{14}$$

where η_{cure} is the viscosity of the continuous phase. Data will be compared to this estimate in Section 4. η_{cure} is assumed to change with the extent of cure in a manner typical of other polymerizing systems [Martin et al. 1989]:

$$\eta_{cure} = \eta_0 \left(\frac{\xi_c^b - \xi^b}{\xi_c^b}\right)^x \tag{15}$$

$$\eta_0 = \eta_{00} e^{\left(E_\eta / RT\right)}, \tag{16}$$

where the pre-exponential factor η_{00}, the extent of reaction at the gel point ξ_c, the Arrhenius activation energy E_η and dimensionless fitting parameters *x* and *b* are determined from fitting data in Section 4.

The bulk viscosity is rarely encountered in modeling liquids, which can usually be safely approximated as incompressible, and it is problematic to measure, especially since it is in fact not a true material function for a bubbly liquid but depends on the flow details [Wilson 1997; Martinez & Kraynik 1992]. We choose to simply assume the relationship between κ and η derived by Martinez and Kraynik through mesoscale modeling, and not pursue an experimental measurement as of now:

$$\kappa = \frac{4}{3}\eta\left(\frac{1-\phi}{\phi}\right). \tag{17}$$

Equation 4 requires C_v, k, and ΔH_{rxn}. The first two quantities can be measured for the final solid foam, and the latter can be measured for the reacting foam mixture in a differential scanning calorimeter (DSC). The heat capacity in equation 4 for a compressible material should be that at a constant volume. We don't know this property of the material as it is reacting; however, mixture theory [Gibson & Ashby 1990; Hilyard & Cunningham 1991] can be used to account for the effect of the evolving gas content:

$$C_p = \frac{C_{p,liquid}\rho_{liquid}(1-\phi_{CO_2}) + C_{p,CO_2}\rho_{CO_2}\phi_{CO_2}}{\rho}. \tag{18}$$

$$k = \frac{2}{3}\left(\frac{\rho}{\rho_{liquid}}\right)k_{liquid} + \left(1-\frac{\rho}{\rho_{liquid}}\right)k_{CO_2}. \tag{19}$$

Evaluation of the former for an epoxy foam [Mondy et al. 2010] shows that the effect of gas is small and predicts that the heat capacity per unit mass is virtually independent of the gas content (foam density). If so, we can approximate C_p by measuring the resulting solid foam heat capacity, as will be shown in Section 5. However, k is more dependent on the gas content of the foam. This equation form will also be tested in Section 5, again, however, for the solid foam, where the properties of the solid continuous phase are substituted for those of the liquid.

3. REACTION RATE EXPERIMENTS

3.1. Materials and Typical Manufacturing Conditions

The structural foam studied is nominally 10 pcf foam when allowed to freely rise during the expansion phase. The recipes for the BKC 44306 PMDI-10 foam components R and T are shown in Table 1, in parts by weight. The R to T mix ratio is 40.3 to 59.7 parts by weight. This results in the overall formula also listed in Table 1. Densities of those components listed with specifications are from the manufacturer supplied data [Dow 2001; SpecialChem 2013].

Table 1. BKC 44306 PMDI-10 Structural Foam Formulation

Material	*Specification*	*PBW*	*Density at 25°C (g/cm^3)*
R-Component (resin)			
Voranol 490 (polyol)	2170369	100	1.109
Water		0.8	0.997
Dabco DC-197 (surfactant)	6500617	1.0	1.01
TMPDA (catalyst)	4604246	0.7	
T-Component			
PAPI 27 (isocyanate)	4612092	100	1.23

Overall formula	*Mass fraction*
polyol	0.3932
water	0.0031
surfactant	0.0039
catalyst	0.0027
isocyanate	0.5970

Structural parts are foamed at KCP under conditions that vary somewhat depending on the mold size, shape, features, etc. [Chace 2013]. Typically the two-part material is preheated to 29.4°C (85°F) and the mold is preheated to 37.8°C (100°F). The material is mixed in fairly large batches (at least 250ml, depending on the size of the mold) with an electric mixer equipped with a blade. The mixed material is immediately poured into the mold, which has been taken out of the oven, and the foam is allowed to rise for about 10 minutes. The mold is then placed in an oven at a higher temperature (typically 121°C or 250°F) to cure.

For our experiments we preheat the material as done at KCP. We usually mix in much smaller batches (approximately 2 g) than used at KCP. There were concerns that mixing small batches would not yield results consistent with the foam used in the actual application; however, use of the overhead mixer fitted with a mixing blade appropriate to the container size seemed to be able to create foam of the same approximate density in a range of batch sizes from 2g to 250g. A

mixing study of small batches (3.5 g) in syringes was performed to further evaluate the effects of time (from 10 to 120s) and mixing rpm (from 100 to 1800s). Sufficient mixing was accomplished to foam the material to a maximum foaming capacity for times equal or above 30s and speeds equal or above 1000 rpm.

3.2. Kinetics of Polymerization

3.2.1 Experiments

Micro-attenuated total reflection (ATR) infrared spectroscopy (IR) measurements, taken with a Bruker Equinox 55 spectrometer with a deuterated triglycine sulfate (DTGS) detector (ID301/8) operating at room temperature, were used to establish the cure conversion kinetics and determine the activation energy for PMDI foam formulations. Details of the procedure can be found in Rao et al. [2010]. PMDI formulations in Series 44307 ranging from nominally 4 to 10 pcf free rise, as well as the PMDI BKC 44306 formulation giving a nominal 10 pcf free rise, were tested. The two part foams were mixed and a sample mass of two grams deposited. The sample size actually probed is only about 1 mg at the surface of the temperature-controlled plate, and, therefore, can be brought quickly to a constant temperature. Cure kinetics were examined between 30 and 90°C. Multiple IR bands were examined: carbonyl formation at ~1700cm^{-1}, urethane ester linkage at 1218cm^{-1}, and a non-assigned band at 1308 cm^{-1}. The peak at 1218 cm^{-1} represents the pure curing reaction, as it relates to the C=O-O-R linkage (i.e., the ester side of the urethane) between the polyol and urethane group. Successive IR spectra were acquired over time (Figure 2), and the relative absorbance changes for specific bands provided time dependent cure-state information.

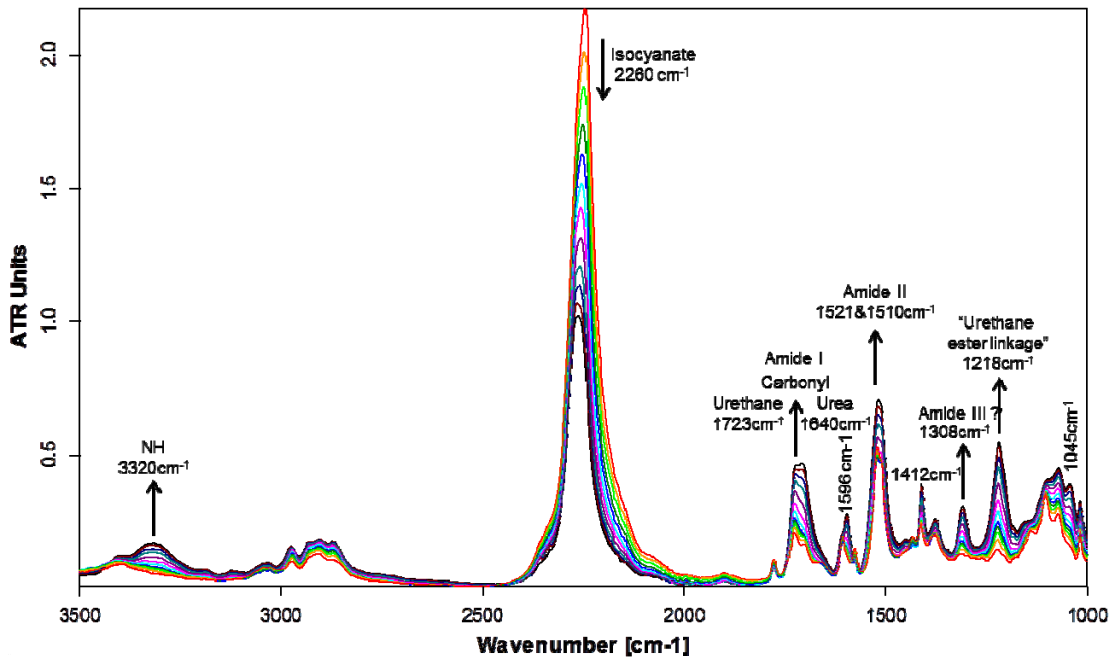

Figure 2. IR-spectra at various times showing the isocyanate peak decreasing as the urethane band and others increase.

3.2.2 Parameter fitting

The height of the 1218 cm^{-1} band as it evolves in time for experiments at several constant temperatures is plotted in Figure 3 (left). These kinetic cure curves were then normalized to range between 0 and 1 to give an estimate of the extent of reaction and then time-temperature shifted (Figure 3, right). It is interesting to note that the maximum peak height is not a clear function of T, so normalization is not introducing a systematic error. Time shifting is performed by multiplying the time at a higher temperature T by a shift factor a_T that causes these higher-temperature data to overlay the data at the lowest temperature tested. These shift factors, or relative reactivity ratios, can then be used to determine the activation energy (E_ξ) for the Arrhenius rate constant in equation 7. A plot of the natural logarithm of the shift factors versus the inverse of temperature in Kelvin yields a linear plot, the slope of which gives E_ξ. Figure 4 shows the resulting Arrhenius plot for the PMDI-10 structural foam data.

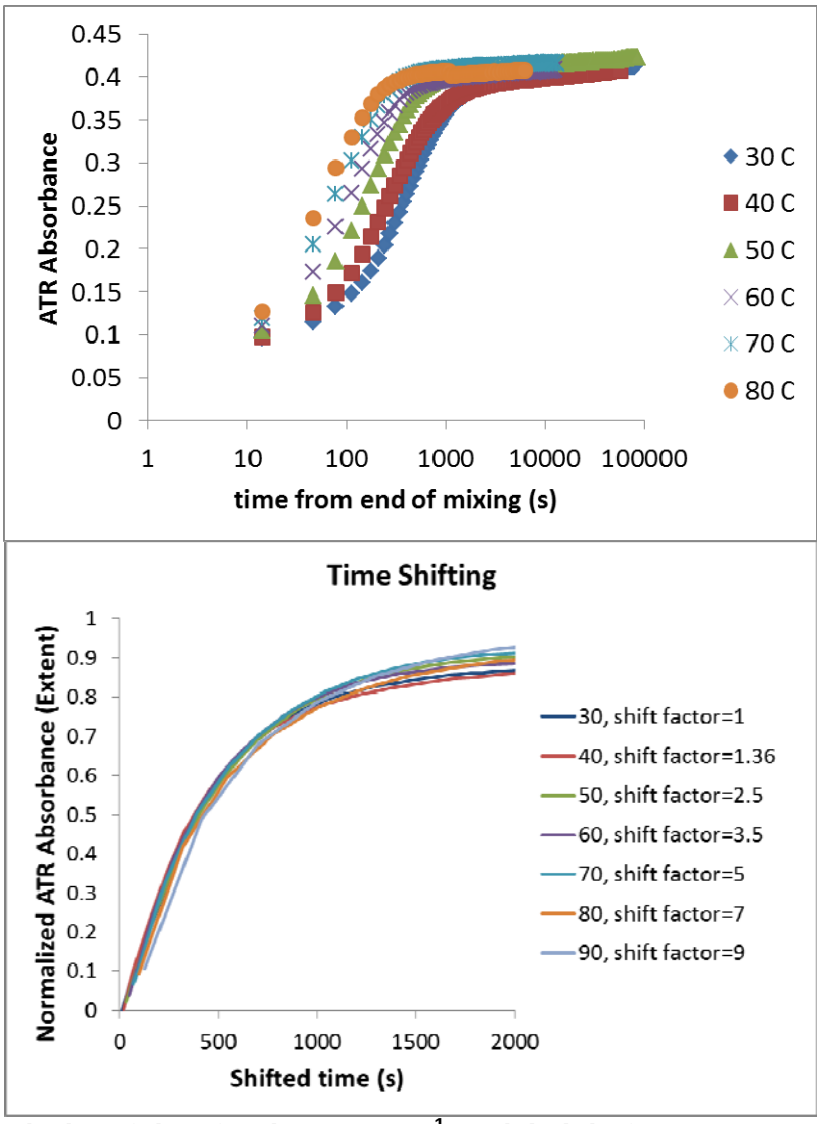

Figure 3. (Upper) Plot of data for the 1218 cm^{-1} peak height for PMDI-10 structural foam. (Lower) Shifted plot for PMDI-10 structural foam, with shift factors noted.

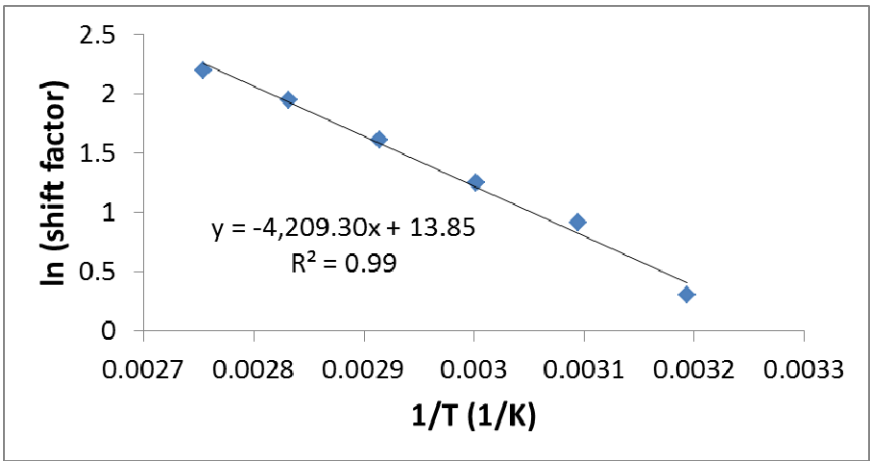

Figure 4. Activation energy (E_ξ/R) given from the time shift factors. Here, E_ξ/R=-4209 K.

The parameters in equations 6 and 7 were then varied until the equations best described the IR data during the foam expansion phase (the first 1000 s or so). The measured rate of reaction was determined numerically from the extent data. Differentiating data can compromise accuracy, so the equation was also compared to the measured extent by observing that

$$\frac{d\xi}{dt} = k(1-\xi)^q(A+\xi^p) \approx \frac{(\xi_i - \xi_{i-1})}{(t_i - t_{i-1})} \quad \text{or} \quad \xi_i = \xi_{i-1} + k(1-\xi_{i-1})^q(A+\xi_{i-1}{}^p)(t_i - t_{i-1}) \tag{20}$$

where ξ_i refers to the data value at time t_i. Then the parameters were evaluated in light of both the rate and extent as will be shown below. The reaction coefficient k was estimated from the initial reaction rates at 30 and 40 °C (close to the manufacturing temperatures at KCP) as shown in Figure 5.

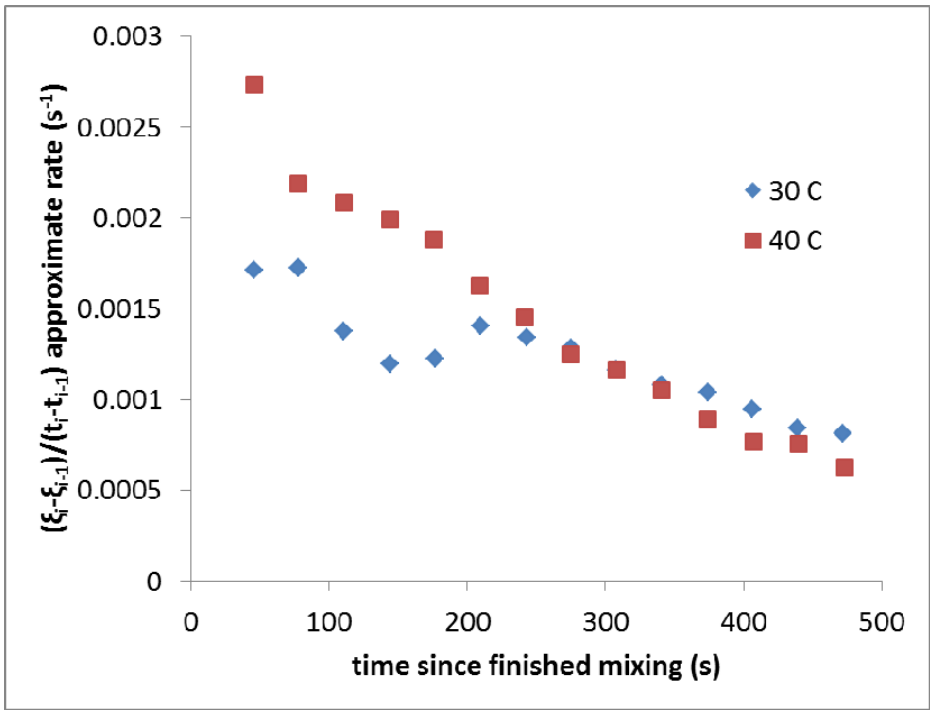

Figure 5. Polymerization rates at early times.

A rough value of k=0.002 s^{-1} at 30°C, combined with the Arrhenius fit from Figure 4, yields a value for k_0 of 2142.24. This value seems to capture the temperature dependency well. The best values to fit the orders of reaction are q=1.7 and p=0.28. Comparison of the theory to data is shown in Figure 6 and Figure 7.

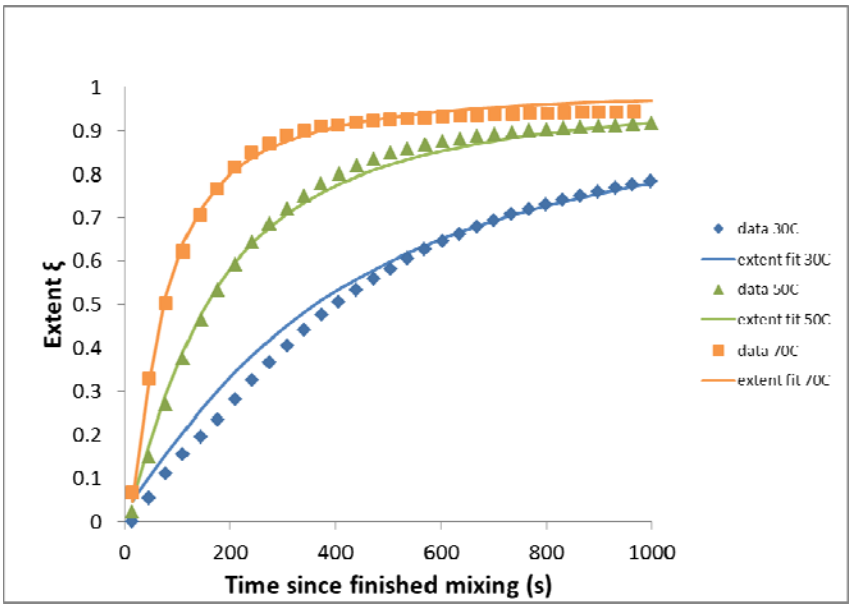

Figure 6. The measured extent of reaction compared to the numerical fit from equation 20 for three different temperatures.

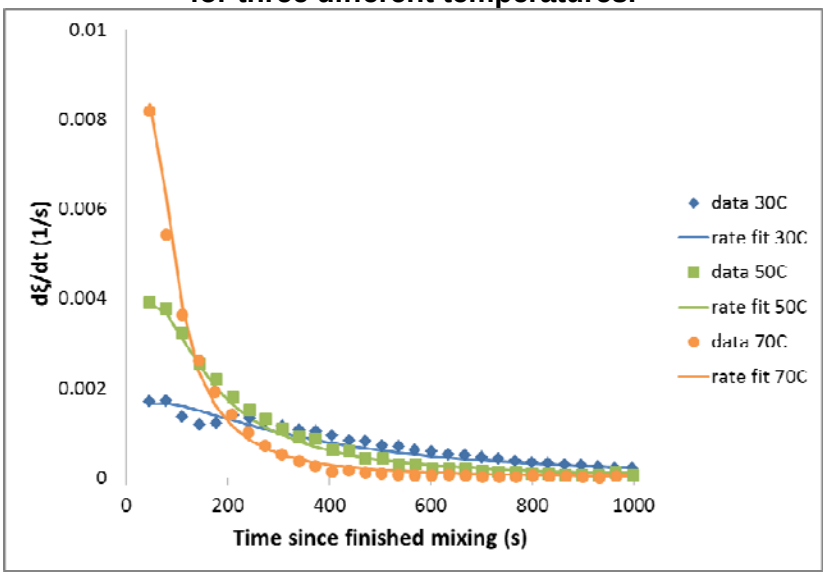

Figure 7. The rate of reaction compared to the numerical fit from equation 6 for three different temperatures.

As mentioned above, the data was fit for the first 1000 seconds to encompass the time during which foam fills a mold. The later curing is predicted to occur too fast, as indicated by the predicted extent reaching a higher value than the data at later times in Figure 8. It is important to keep this in mind, if one is modeling the post-gelation curing.

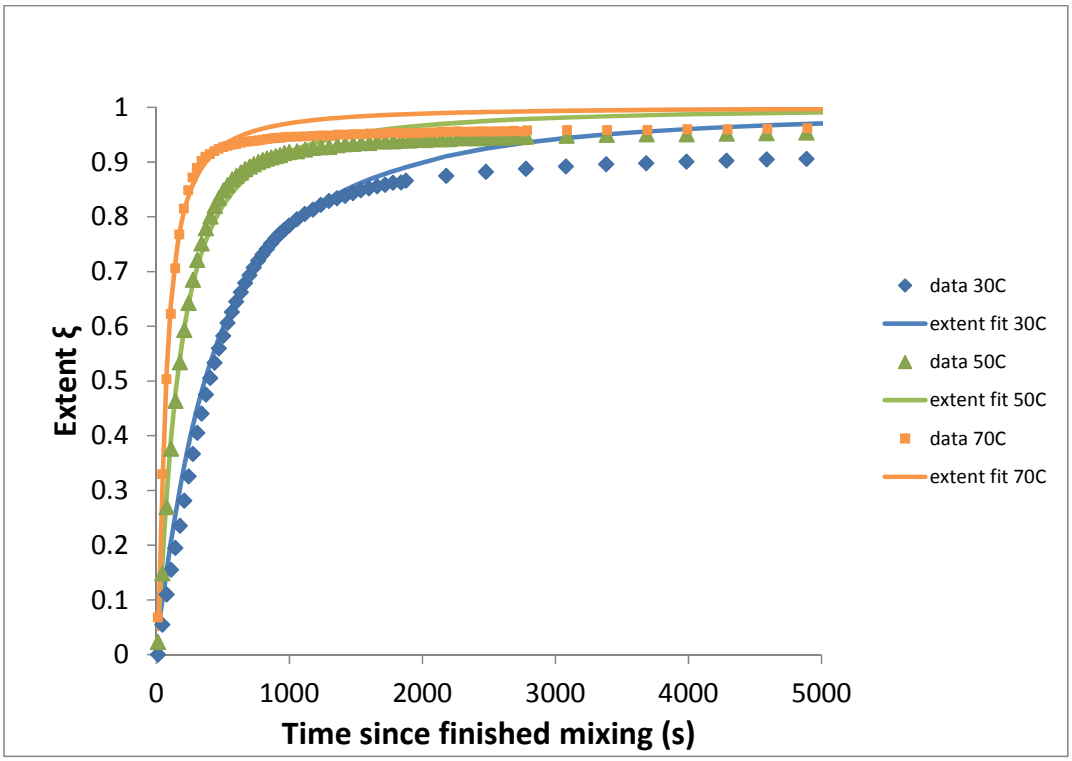

Figure 8. The measured extent of reaction compared to the numerical fit from equation 20 for three different temperatures at longer times.

Unfortunately, no specific peak in the IR spectrum exists for the foaming reaction, first of all since the carbamic acid generating CO_2 is a transient species, and secondly since after decomposition the resulting urea linkages (carbonyl and amide groups) overlap with the urethanes in the spectrum. Therefore, a different method must be used to determine the foaming reaction rates, as will be discussed in the following subsection.

3.3. Foaming Reaction

3.3.1 Experiments

In order to estimate the rate of gas formation, we observe the height evolution of a foam column with time and assume that the increase in volume is solely due to the production of CO_2. This method is somewhat inadequate as it cannot account for all the CO_2 produced as some is lost to the atmosphere through the free surface and does not produce an increase in volume, and some remains supersaturated in solution and does not nucleate to form gas bubbles. Because the reaction is exothermic and because the foam precursor materials cannot be preheated to high temperatures or the water will evaporate and not be available for the foaming reaction, these height-vs.-time experiments cannot be done under isothermal conditions, unlike the IR

spectrophotometry. We were also unsure whether or not the blowing reaction could produce pressurized bubbles, especially after the continuous phase becomes viscous and slows the foam rise. Therefore, not only volume change, but also temperature and pressure are measured. The number of moles of CO_2 is then estimated through the ideal gas law ($n_{CO2}=PV/RT$, where V is volume). By doing this, we are assuming that the volume change due to temperature of the liquid phase is negligible, as is any volume change from reactions not producing gas.

Figure 9 shows a schematic of the experiment, and Figure 10 shows details of two molds used. Foam is injected near the bottom of the mold. Each mold includes two thermocouples and two flush mounted pressure transducers. Because the channel depth is small, all of the sensors are inserted from the back, and since plumbing requires some space, the sensors cannot be placed at the same height in the channel. The thermocouples are inserted to a depth of half the channel depth.

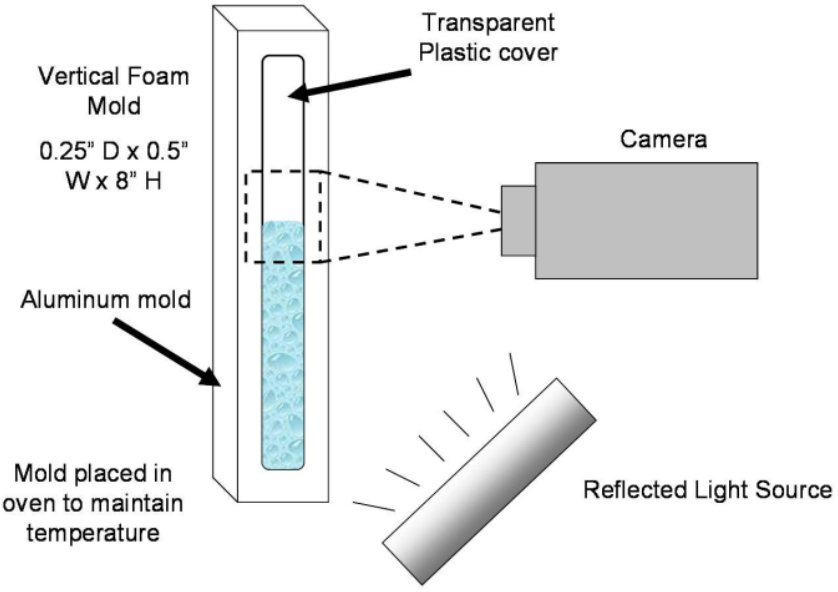

Figure 9. Sketch of channel apparatus and location of thermocouples and pressure sensors.

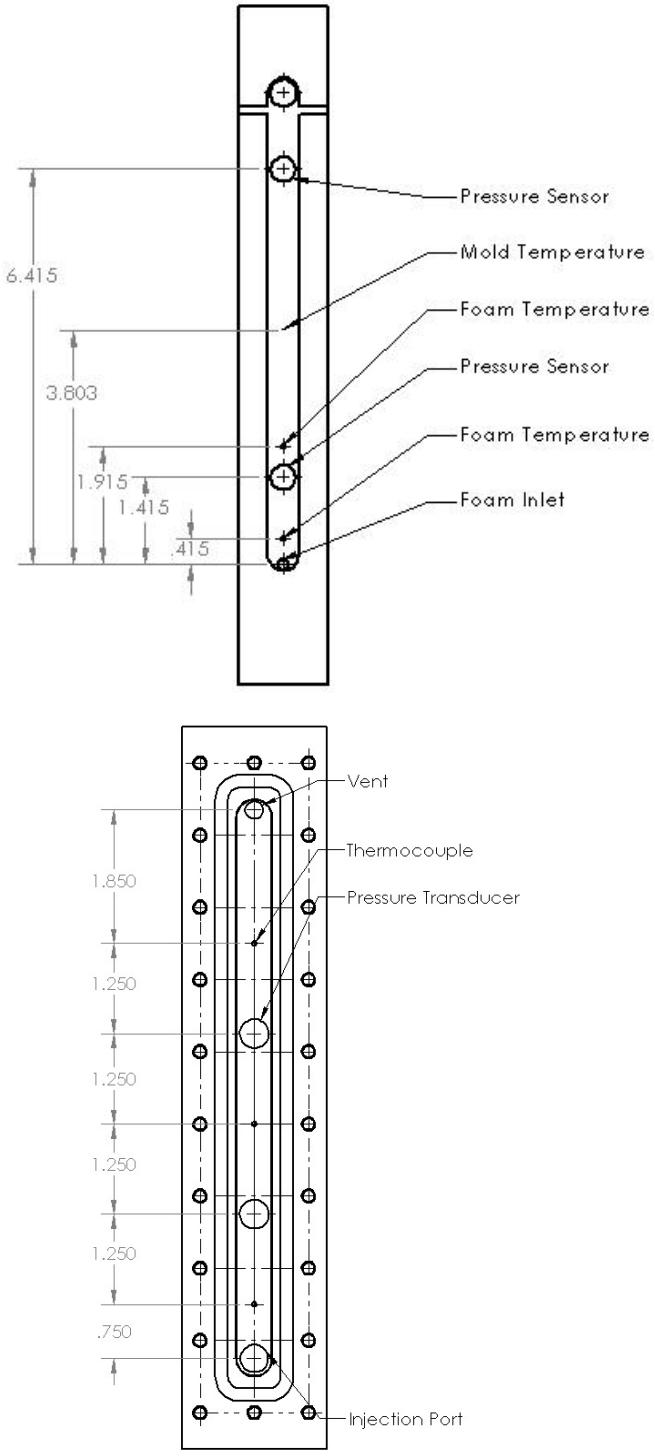

Figure 10. Sketches of two similar channel molds used to measure the evolution of gas during foaming. The mold on top uses a bar to close off the top to allow over packing of the foam. The mold on the bottom allows the channel to be various depths. Dimensions are in inches.

Experiments described here were performed with a channel depth of 0.79 cm (0.31 inches). This depth was chosen to be representative of a typical thickness of structural parts and thin enough to help control the temperature by minimizing the exothermal response and maximizing the influence of the mold temperature. However, future experiments are planned to look at the influence of channel depth on the volume change, as the drag of the walls and possible bubble breakage due to shear may be important to consider.

All tests are performed in an oven, where the mold is preheated to the desired testing temperature. For all tests the precursor foam material is preheated to 30 °C (similar to procedures performed at KCP). The material is mixed for 45s inside the injection syringe with an overhead mixer fitted with a small spatula rotating at 1800 rpm. Mixing directly in the injection syringe allows a much faster transfer of the material into the mold after mixing.

Figure 11 shows frames from a typical front-tracking video at an oven temperature of 30°C. Note that the foam started expanding in such a short time that it was difficult to capture the initial time data, even at this relatively low temperature where the reactions are slower.

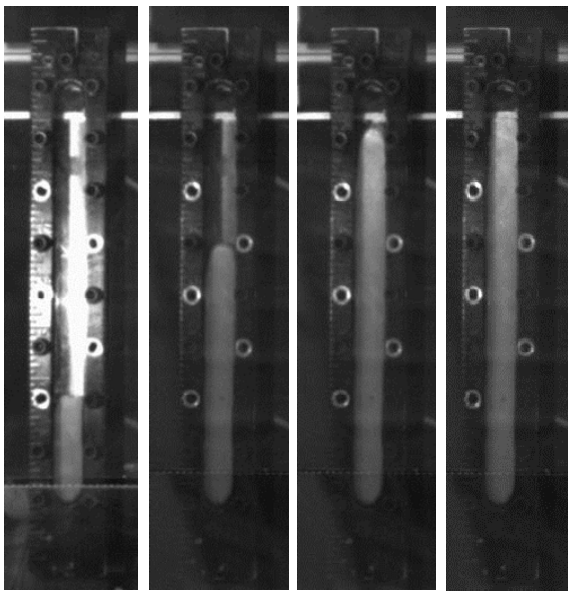

Figure 11. Video showing structural foam PMDI-10 expanding in a mold at 30 °C. The frames correspond to time= 13, 73, 158, and 245 s after the end of mixing the resin and the curative together for 45 seconds. Even at this relatively low temperature the foam had expanded significantly within the 13 seconds that it took to load the syringe injector and get the material into the mold.

Individual frames are analyzed with image processing software (Image Pro Plus, Media Cybernetics, Rockville, MD) to determine the height with time, calibrated with the known dimensions of the channel. Knowing those dimensions of the channel, we can convert the height of the foam to volume, and knowing the mass injected we can convert the volume to an overall density. Assuming volume change is caused by the generation of CO_2 gas and possible expansion or contraction due to temperature; we can calculate the generation rate of the gas forming reaction.

Example data are shown for the case of an oven temperature of 50°C in Figure 12 and Figure 13. Note that the temperature peaks before the foam stops expanding. The temperature rise is caused by the heat of reaction, discussed further in Section 5. Note also that the pressure peaks after the foam stops expanding; implying that the bubbles may become pressurized after the polymerization restrains the bubble expansion. However, the pressure is measured at the wall, and it is not clear how that pressure is related to that within the bubbles. For lack of a better estimate, we use this wall pressure to calculate the moles of gas.

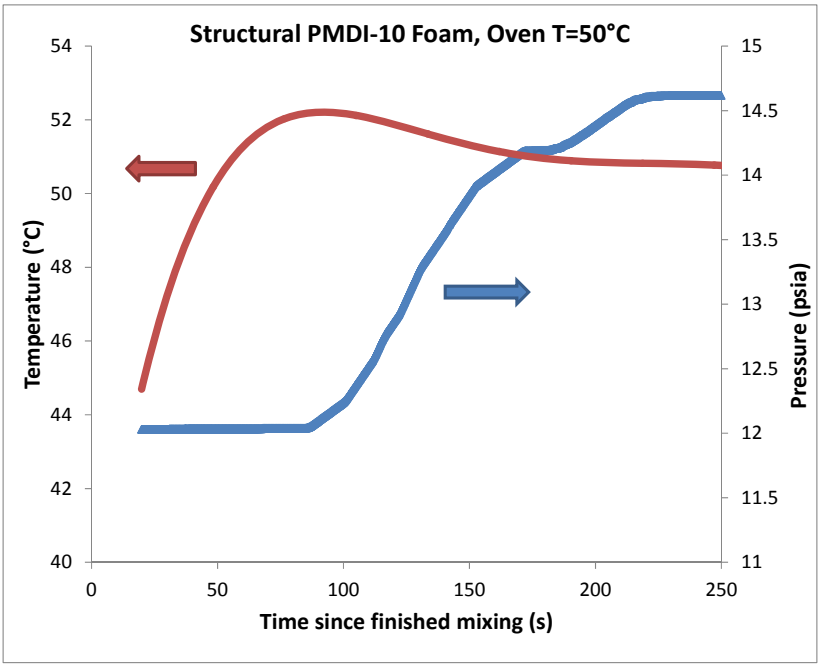

Figure 12. Temperature and pressure measurements used to calculate the number of moles of CO_2 produced at a nominal temperature of 50°C.

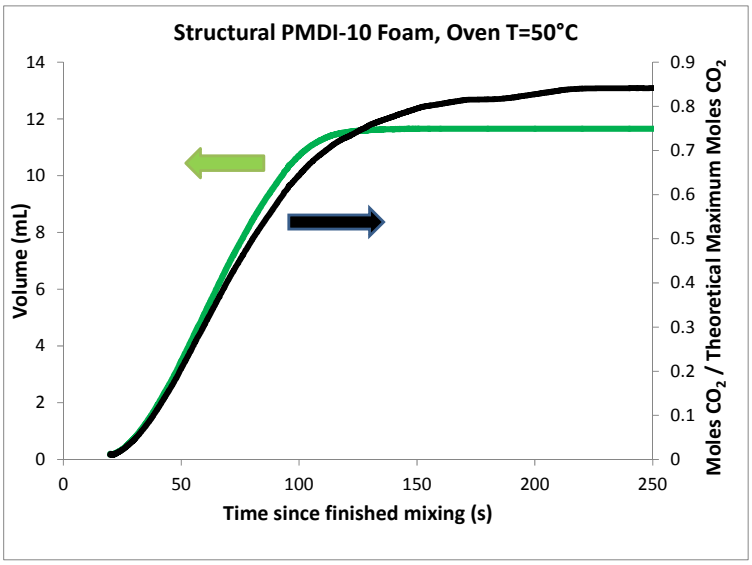

Figure 13. Measured volume and the moles of CO_2 produced calculated from the ideal gas law.

The extent of the foaming reaction α is defined here as the number of moles of CO_2 divided by the maximum number possible from stoichiometry (Table 1). As there is an excessive amount of isocyanate, the limiting reactant to produce CO_2 is water. One mole of CO_2 is produced from each mole of water (H_2O) in the foam kit formulation. For BKC 44306 PMDI-10 foam, the initial mass fraction of H_2O is 0.0031, which implies that the maximum number of moles of gas possible to be produced is the mass of foam precursor material injected into the mold times 0.0031/18.05, where 18.05 is the molecular weight of H_2O. Note that this assumes that there is no additional water absorbed into the resin components as received from the manufacturers or that water is not absorbed or lost to the atmosphere during storage or processing.

3.3.2 Error Analysis

Because the foam rise experiments to determine n_{CO2} required multiple measurements, an error analysis was undertaken to estimate the uncertainty in the results [Crowder et al. 2011; Joint Committee for Guides in Metrology 2008]. From a propagation of error analysis using the ideal gas law as the equation (f) for the estimate of n_{CO2}, one can write the uncertainty u in the moles of CO_2 as a function of the uncertainty in each measurement, where the subscript indicates the measured quantity and the bar indicates the mean value:

$$u_{nco_2}{}^2 = \sum_i \left(\frac{\partial f}{\partial x_i} \right)^2 u(x_i)^2 = \left(\frac{\overline{V}}{R\overline{T}} \right)^2 u_P^2 + \left(\frac{\overline{P}}{R\overline{T}} \right)^2 u_V^2 + \left(\frac{\overline{PV}}{R\overline{T}^2} \right)^2 u_T^2 . \quad (21)$$

Measurements of P include error in the raw measurements (calibration of the pressure sensors) and normalization of the pressure reading to the measured barometric pressure at the initial time:

$$P = P_{raw,t} - P_{raw,init} + P_{barom} . \quad (22)$$

From the manufacturer's information the pressure gauges are good to ±0.15psi and the barometer to ±0.025psi. Following the example of equation 21, the uncertainty in *P* can be estimated from:

$$u_P^2 = \sum_i \left(\frac{\partial P}{\partial x_i} \right)^2 u(x_i)^2 = u_{P_{raw,t}}^2 + u_{P_{raw,init}}^2 + u_{P_{barom}}^2 . \quad (23)$$

The uncertainty in each measurement is estimated as Type B uncertainties with square distributions, i.e., the possible error range divided by the √3. These values and those described below are listed in Table 2 for a typical experiment at 50°C.

The volume is a combination of the volume measured through image processing (what can be seen in the channel), plus the volume in the tubing that cannot be seen, minus the initial volume of the liquid phase plus the air entrained during mixing. The latter is determined by taking the mass injected and dividing it by the initial density of the material.

$$V = V_{IP} + V_{hidden} - V_{liquid} = V_{IP} + V_{hidden} - (mass / \rho_{init}) . \quad (24)$$

We estimate the accuracy of the image processing by measuring the perceived area (height × width) with image processing and comparing it to the known value of the rectangular area at a certain height. The volume of the foam (V_{IP}) is then estimated from the area of the foam (including curvature at the bottom from the mold shape and the top from the shape of the free surface) multiplied by correction factors for the width and height measurements. Knowing the typical correction factor, we assess the error to be about 5% of the value with a normal distribution. The hidden volume was measured by pouring a known mass of water into the system. This was repeated seven times, and, therefore, we approximate the error in the mean of the measurements to be that of normally distributed data, i.e. the standard deviation divided by the square root of seven. The initial density of the material (which depends on the amount of entrained air) has been estimated both by trying to quickly measure the volume of a known

amount of the mixed foam kit and by measuring the density of the dry material (mixed with the same protocol as used for the full foaming kit) after it cures to a solid. The former method is very difficult to execute, and the latter method was deemed much more quantifiable and reproducible, and, therefore, is used to estimate the initial density. This assumes that no air escapes while the foam is curing and that there is negligible cure shrinkage. However, the average value was in agreement with our estimates from looking at the initial volume immediately after mixing. We again approximate the error to be that of normally distributed data, i.e. the standard deviation divided by the square root of the number of data points, in this case 13. From the difference in measurements of the mass in the syringe before injection and the mass recovered after the foam cured, we believe that the error in the mass injected is larger than the manufacturer's error range of the balance. We estimated the error to be ±0.1 g and assumed a square distribution of a Type B error. Combining these errors, we get the uncertainty in V:

$$u_V^2 = u_{V_{IP}}^2 + u_{V_{hiddent}}^2 + \left(\frac{1}{\overline{\rho}}\right)^2 u_{mass}^2 + \left(\frac{\overline{mass}}{\overline{\rho}^2}\right)^2 u_{\rho init}^2 \,. \tag{25}$$

The temperature is taken to be that measured by the bottom thermocouple. However, before the foam reaches the bottom thermocouple, we estimate the foam temperature to change linearly with time from the initial temperature of the preheated material (30°C) to the temperature recorded when the foam hits the bottom thermocouple. Although only an estimate, we do not try to quantify the error in this approximation. The uncertainty in the temperature u_T is estimated from the manufacturer's published error range, again with a square distribution.

The expanded uncertainty in the measurement of the number of moles of CO_2 at the end of the experiment is the uncertainty given by equation 21 times the Student-t value for the overall degrees of freedom. Because of the large number of degrees of freedom, we use the Student-t value 1.96 for a 95% confidence limit. The expanded uncertainty in n_{CO2} is then about 3.7×10^{-5} out of 4.7×10^{-4} moles measured at the end of the experiment, or about 8% of the final value for a typical experiment at 50°C. This is an estimate of the minimum uncertainty expected. It is important to take into account all the assumptions made in the experiments and error analysis, especially the assumption that all of the CO_2 produced increases the volume and/or the pressure and that the pressure in the bubbles is that measured at the walls. The actual uncertainty must be higher, therefore.

Table 2. Distributions for Input Quantities and Standard Uncertainties

Input Quantity	Mean or typical value	Standard uncertainty Type A	PDF Type A	Standard uncertainty Type B	PDF Type B	degrees of freedom
P_{raw}	14.2			0.087	square	∞
P_{barom}	12.2			0.014	square	∞
T	323.15			0.029	square	∞
V_{IP}	10	5% of reading	normal			1
V_{hidden}	1.9	0.01	normal			6
mass	2			0.058	square	∞
ρ_{init}	1.0	0.05	normal			12

The rate of change of n_{CO2} has even more associated error, because to estimate this, one must differentiate the data (similar to equation 20). We take data every 0.1 seconds, so the differences between data points are small relative to the overall time of the experiment (at least several hundred seconds). The times of the P and T measurements and the frames of the video are all synchronized with the beginning and end of mixing (when an electronic signal is sent to the data acquisition computer). Although the experiment is timed, including the duration to mix and inject the material, it is still uncertain when the reaction actually starts. We take "time=0" to be the end of mixing. We do this consistently with all experiments (IR, rheology, etc.) so this uncertainty merely shifts all models by the same reference time.

3.3.3 Parameter Fitting

We found that the Michaelis-Menten reaction form (equation 8) seemed to give the richness necessary to fit the data. Parameters are once again chosen to best fit both the extent and rate of foaming at several temperatures, similar to what was done in the previous subsection (3.2.2). The best fit of the data was achieved with the following parameters:

$n = 1.5$

$m = 6$

$A_1 = 8.769638$

$-E_1 / R = -2269.2$

$A_2 = 0.000976$

$-E_2 / R = 1904.6$

$t_{nucleation} = 26$

where A_1 is in units of s^{-2} and $t_{nucleation}$ is in s.

Figure 14 shows the Arrhenius fit and Figure 15 through Figure 17 show the comparison of the data to equation 8 (and its numerical integral) at several temperatures. The model has difficulty matching the drastic slowdown of the foam rise behavior at later times at all temperatures. Nevertheless, the predicted density from the kinetic equation coupled to equations 12 and 13 compares well to the direct measurements (Figure 18).

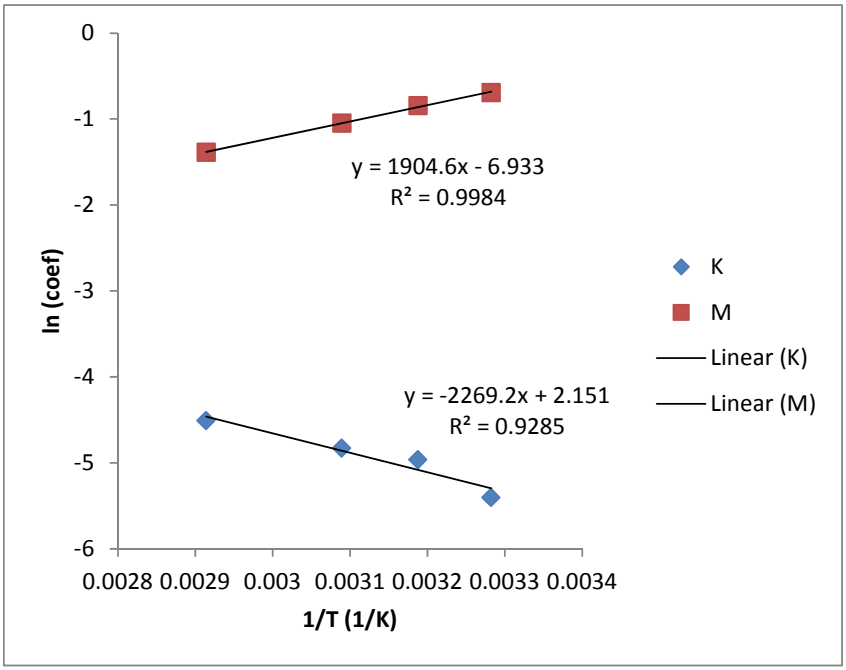

Figure 14. Arrhenius behavior of coefficients K and M in equation 8.

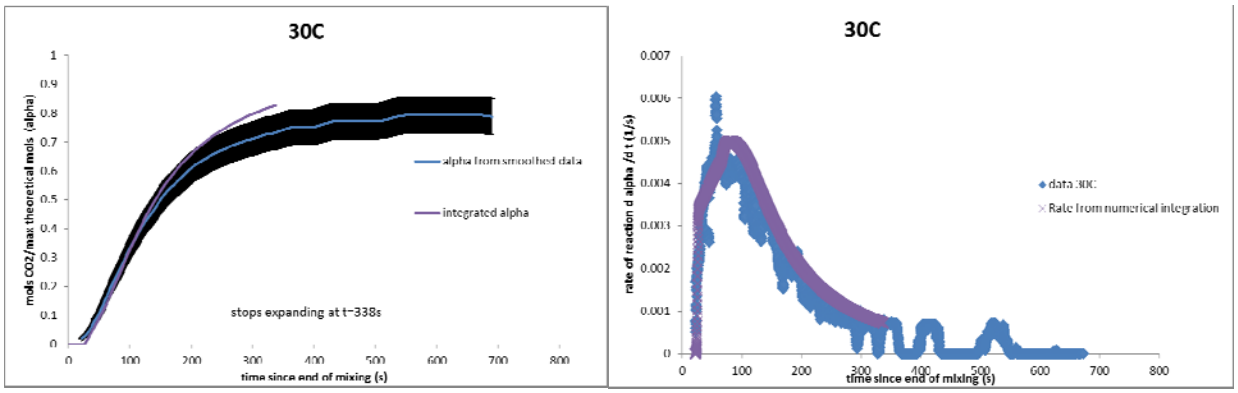

Figure 15. Model compared to data for BKC 44306 PMDI-10 foam at an oven temperature of 30°C. Black bands indicate 8% error bars.

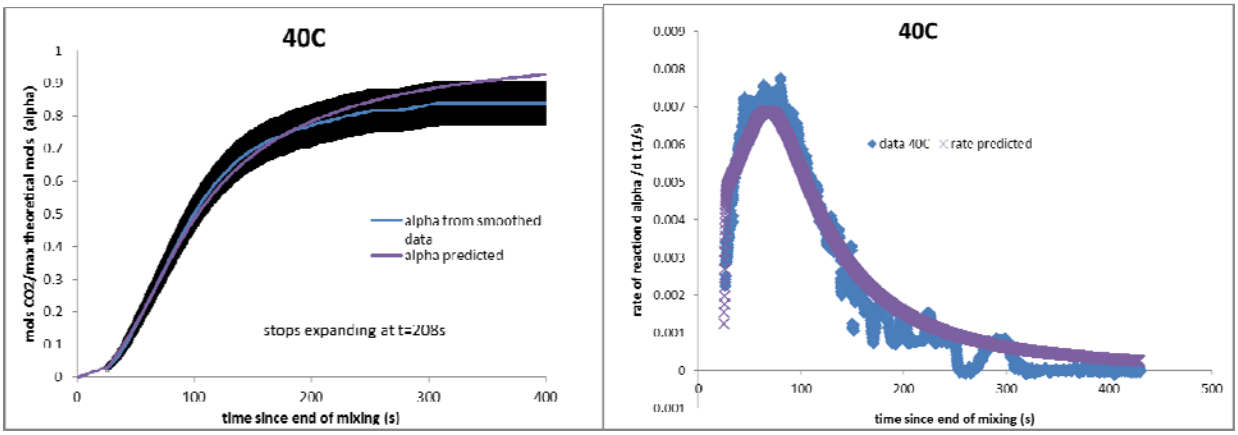

Figure 16. Model compared to data for BKC 44306 PMDI-10 foam at an oven temperature of 40°C. Black bands indicate 8% error bars.

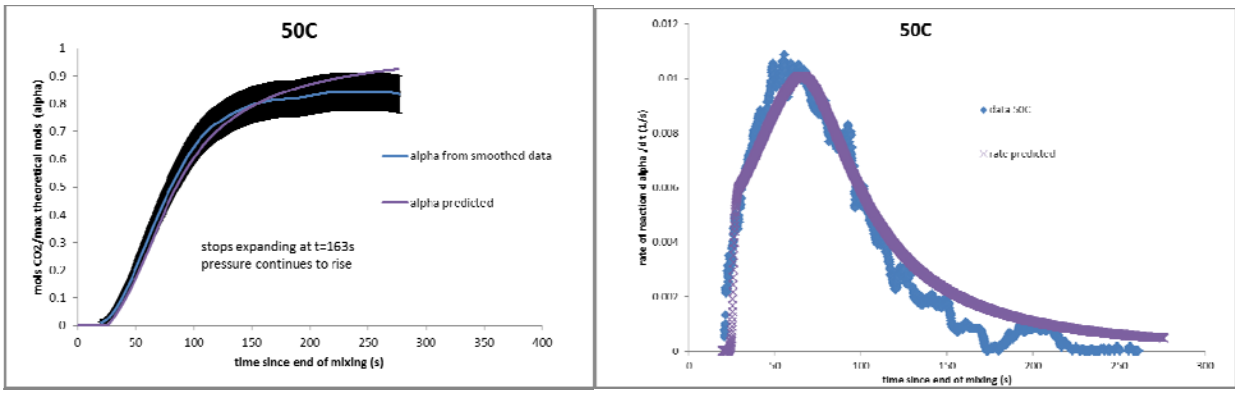

Figure 17. Model compared to data for BKC 44306 PMDI-10 foam at an oven temperature of 50°C. Figures on the left are *α vs.* time and on the right are rate of reaction *vs.* time. Black bands indicate 8% error bars.

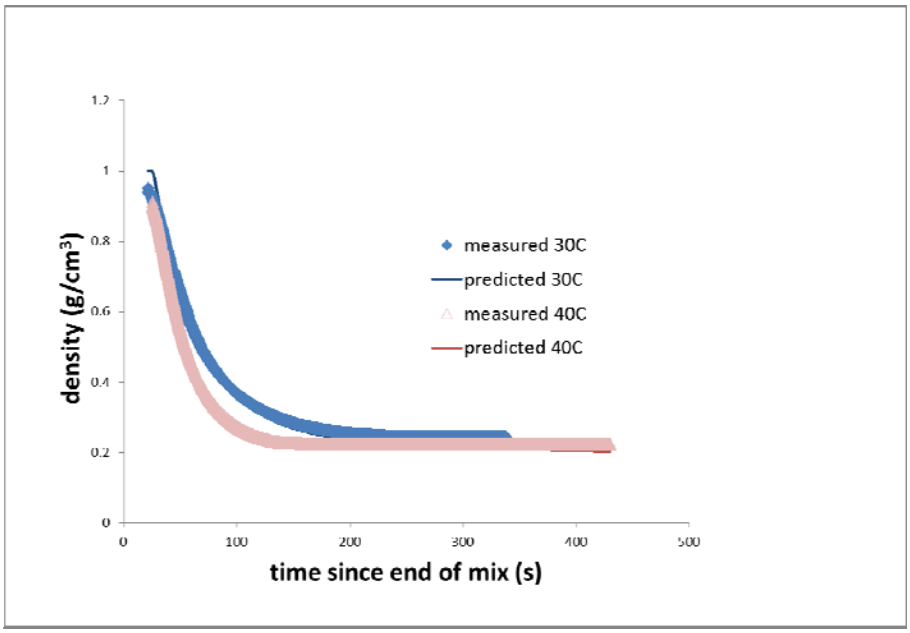

Figure 18. Predictions of density (equations 8 through 13) compared to measured density with time in the channel.

3.3. Decoupling the Foaming and Polymerizing Reactions

The use of extent of reaction in the kinetics equations outlined above relies on the ability to decouple the curing and foaming reactions even though they both consume isocyanate. We hypothesize that this is possible because isocyanate is in excess, especially at early times. The data show that the foaming reaction is faster than the curing reaction, giving credence to the validity of this hypothesis (Figure 19).

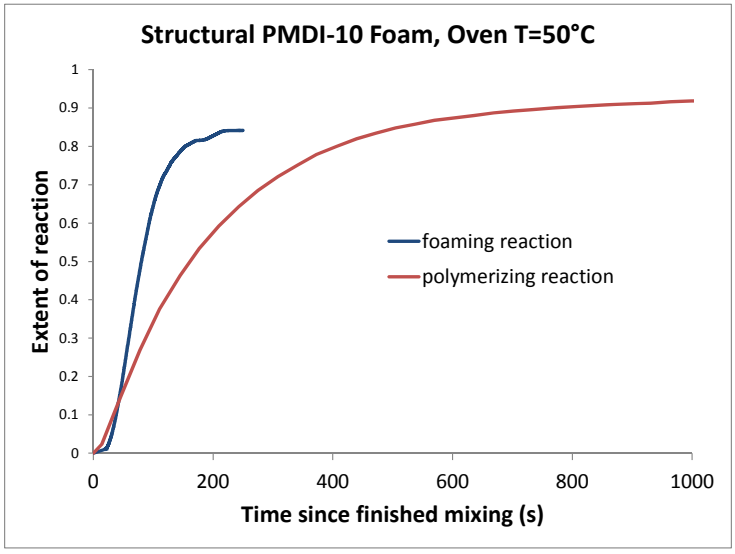

Figure 19. Rates of two main reactions in producing BKC 44306 PMDI-10 polyurethane foam.

When using mixture theory, we need to know the material behavior of the continuous phase alone. In a reacting, foaming polymer this can be problematic. We hypothesize that properties of the continuous phase and the effects of curing can be approximated by those of a dry material, where no water is available to fuel the gas producing reaction. Shown in Figure 20 are earlier IR spectroscopy data taken on dry material, which showed limited influence of the gas producing reaction on the polymerization rate for a similar polyurethane foam used for encapsulation (44307 series PMDI). Although it is impossible to remove all the water in a "dry" formulation, the cured material is much more transparent and shows many fewer bubbles, most of which we speculate are entrained air from mixing the two parts of the foam kit together.

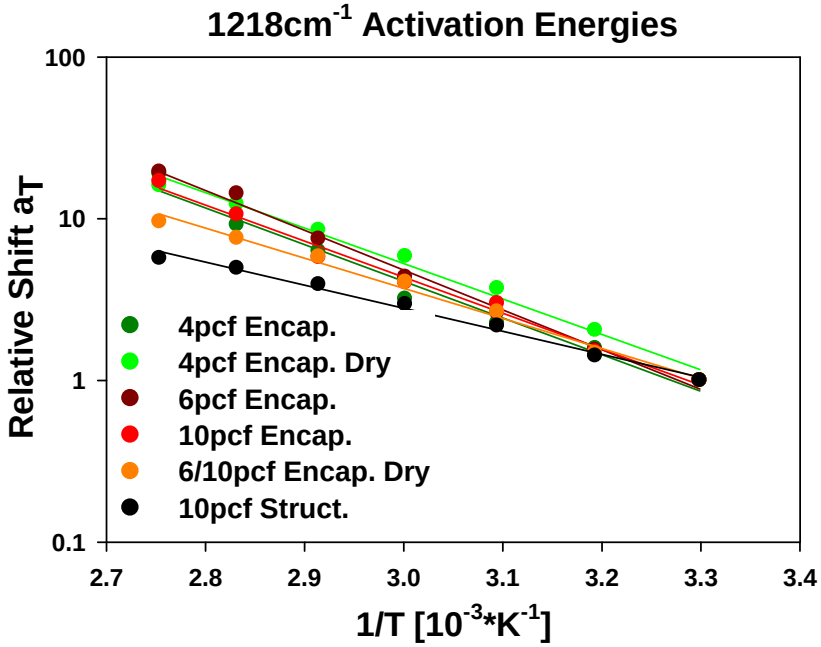

Figure 20. Arrhenius plot derived from IR data (the 1218 cm^{-1} peak) for several PMDI foams used for encapsulation (44307 series), wet and dry (foaming and non-foaming), compared to data on the BKC 44306 structural wet formulation.

Interestingly, although the foaming reaction seems to have very little influence on the curing rate, the curing reaction can have a strong influence on the foaming reaction. The foaming reaction between water and isocyanate in a model system (an epoxy resin of similar viscosity and without polyol, the crosslinking reactant) occurs much slower than in the real system [Mondy et al. 2010]. However, note that those data were taken in cups with a much larger diameter (~5cm); therefore, there could be a significant effect of the temperature rise caused by exothermic

polymerization reaction. In light of this earlier study, we did not attempt to measure the foaming reaction rate in a model system, but instead settled on measuring the foaming reaction in the real system in the nonisothermal experiments described above.

4. RHEOLOGY

4.1. Introduction

The rheology of the reacting polymer foam is complex, changing in time because of the changing temperature, the curing of the continuous phase, and the growing gas fraction. For example, Figure 21 shows rheological measurements of the structural PMDI-10 foam during free rise expansion at 30°C. These measurements were taken on a TA AR-G2 with parallel plates, either dynamically (in oscillation) at a frequency of 1 Hz and an oscillatory stress of 5 Pa (top) or in steady shear at several constant shear rates (bottom). The gap between plates, here, was 1.0 mm. The foam was allowed to expand and overflow the fixture during the course of the experiment. Therefore, there is both shear flow and elongational flow (due to the flow in the r direction) occurring during the experiments, and the recorded moduli and viscosities are only apparent values. More details of the experiments will be given in the following subsections. The regions (I – IV), outlined in the figure after similar work by Bouayad et al. [2009], show clear differences in material behavior; although, the labels are speculations.

The loss modulus (G'') and storage modulus (G') cross multiple times. For a Newtonian fluid, G'=0 and the viscosity is equivalent to G''/ω, where ω is the angular frequency of the oscillations. For a purely elastic solid, G''=0. At early times (region I), the liquid material has few cross links and little gas content, and, as such exhibits a loss modulus higher than the storage modulus (i.e., it is more viscous than elastic). The early time viscosity also obeys the Cox-Merz rule, which states that the shear viscosity and the magnitude of the complex viscosity η^* are equivalent [Cox & Merz 1958]:

$$\eta = \left|\eta^*\right| = \frac{\left|G^*\right|}{\omega} = \frac{\left|(G'+iG'')\right|}{\omega}. \tag{26}$$

This "rule" holds for most liquids, including many polymeric systems, but often breaks down for materials such as foams, whose microstructure dominates the rheology.

We speculate that in region II, the material becomes more like an elastic solid as the gas content increases to create a foam, as opposed to a bubbly liquid. At this point the viscosity measured in steady shear at low shear rates is quite a bit higher than the complex viscosity. Also in this region, the shear viscosity depends on the shear rate. Higher shear rates (>0.01 s^{-1}) tear the foam structure and result in apparent shear thinning. It may be rearrangement of the structure that results in a measurable apparent viscosity above the presumed gel point (as opposed to the theoretically infinite viscosity above the gel point).

In region III, the polymerization of the continuous phase begins to dominate the rheology. G'' is once again higher than G', as the viscosity of the continuous phase becomes very high. At later times, close to the vitrification point, the shear viscosity no longer exhibits such sensitivity to the shear rate, as the viscosity becomes less dependent on the foam structure and is dominated by the continuous phase viscosity. The data beyond the presumed vitrification point, in region IV, are suspect as the compliance of the rheometer is reached; the viscosity is essentially infinite beyond the vitrification point.

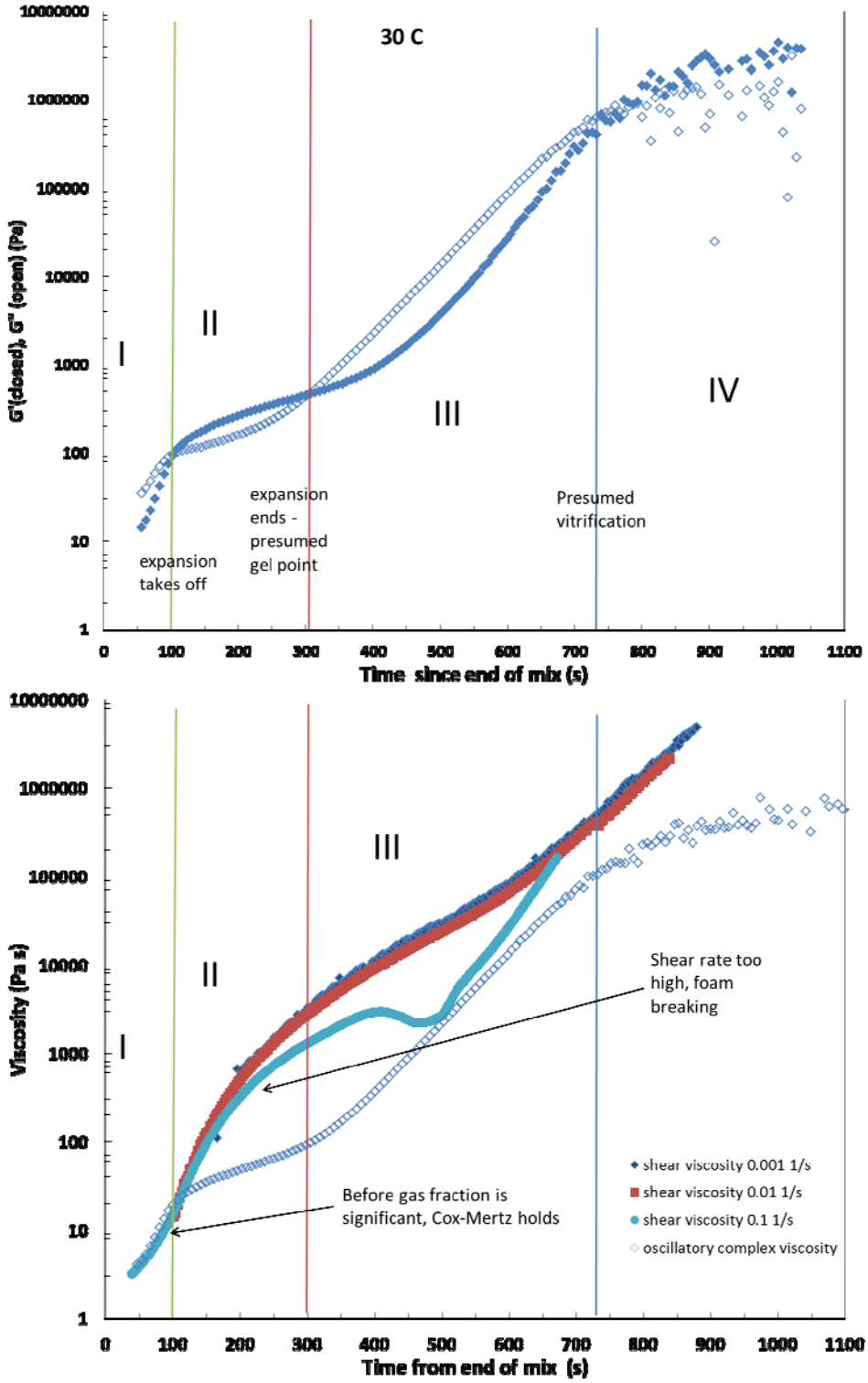

Figure 21. Oscillatory measurements of loss and storage modulus (above) and steady shear measurements of apparent viscosity (below).

In order to separate the effects of polymerization and gas bubble evolution on viscosity, we used a dry formulation, as discussed in the previous section, to approximate the material of the continuous phase. In the following subsection we detail the experiments on the dry material and determine parameters for equations 15 and 16. After that we then describe experiments with the full foaming system and examine the appropriateness of using equation 14 for a model of the foam rheology.

4.2. Continuous Phase

4.2.1. Dynamic Viscosity

The goal of characterizing the rheology of the dry material is to estimate the viscosity of the continuous phase, η_{cure}. The material is mixed with a similar protocol as the foaming material used in subsection 3, *i.e.*, in a 10 ml test tube with an electric mixer equipped with a simple spatula-shaped blade at 1800 rpm for 45 s. The components are preheated to 30°C. The rheometer plates are preheated to the operating temperature so that the material will more quickly reach that temperature once loaded onto the bottom plate. Nevertheless, it takes time (roughly 60 to 90 s) to load the material.

The oscillatory stress was controlled at values ranging from 0.1 to 10 Pa (at 1 Hz) and showed no significant effect of the stress value, indicating that we were within the linear viscoelastic regime. Moduli were measured at four temperatures (30, 40, 50, 70°C) and a dynamic viscosity was determined from equation 26.

As will be discussed in the next subsection, we were hoping to find a rheological signal to define the gel time and then infer the extent of reaction at that time to populate equation 15. Beyond the gel point, the dynamic viscosity becomes very high, and the strain could become exceedingly small. Although the rheometer used is naturally stress controlled, a feedback loop allows operation in strain-controlled mode as well. Therefore, experiments where the strain was controlled to be 0.1% were later performed to determine if the late-time viscosities measured by controlling the stress were reasonable and if higher viscosity measurements could be made using the strain-controlled mode. The strain-controlled data shown in Figure 22 are similar but

distinguishable from the stress-controlled data. However, as will be shown in the next subsection, the difference can be attributed to the difference in the time taken to load the rheometer. The later data (strain controlled) were taken on material that had been loaded into the rheometer faster (after much experience) and so reached the hotter (50°C) temperature faster, resulting in higher moduli at all times leading to vitrification. Measurements of the moduli were essentially limited in both modes to about 1×10^6 Pa.

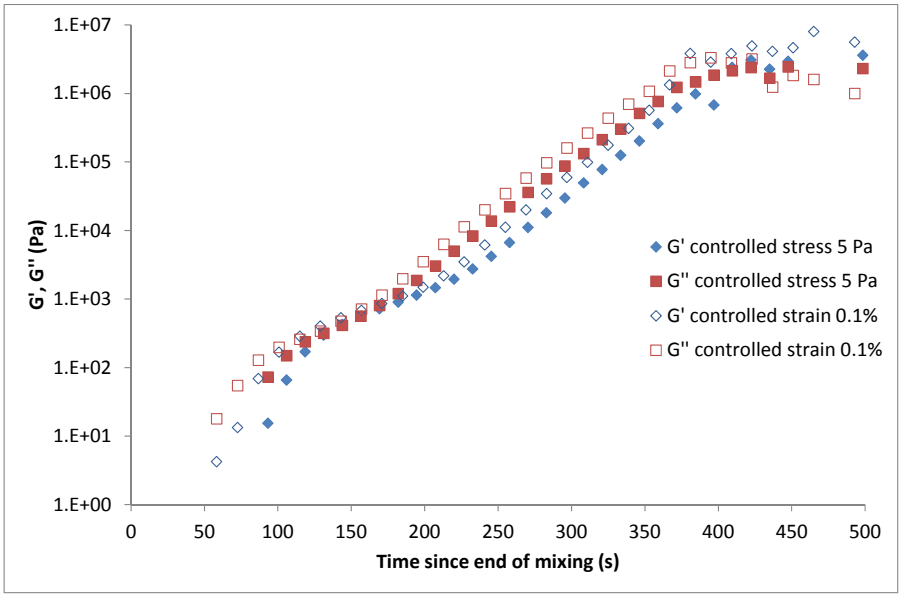

Figure 22. Loss and storage moduli data at 50°C and 1 Hz for either a constant strain of 0.1% or a constant stress of 5 Pa.

Figure 23 summarizes the data used for the parameter fitting described in the next section. Viscosities above about 5×10^5 Pa s are merely reflecting the limitations of the rheometer. All data were taken at 1 Hz. The viscosities did depend on the frequency somewhat (Figure 24). Because the higher frequencies missed some features of both the early-time and late-time behavior, we used the 1 Hz data for parameter fitting.

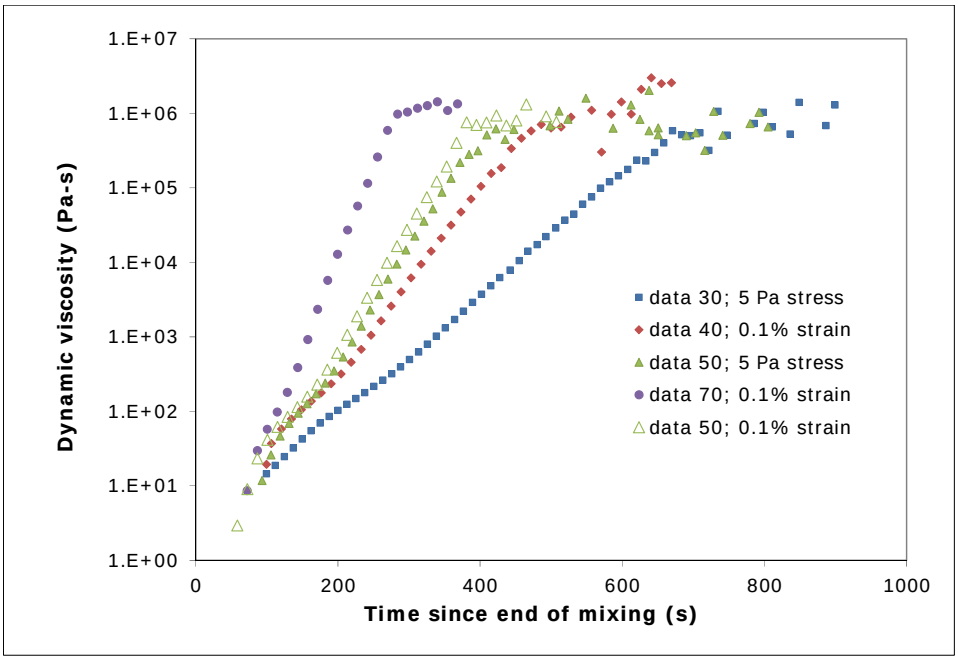

Figure 23. Viscosity of the dry BKC 44306 PMDI (nonfoaming) material (taken at 1 Hz).

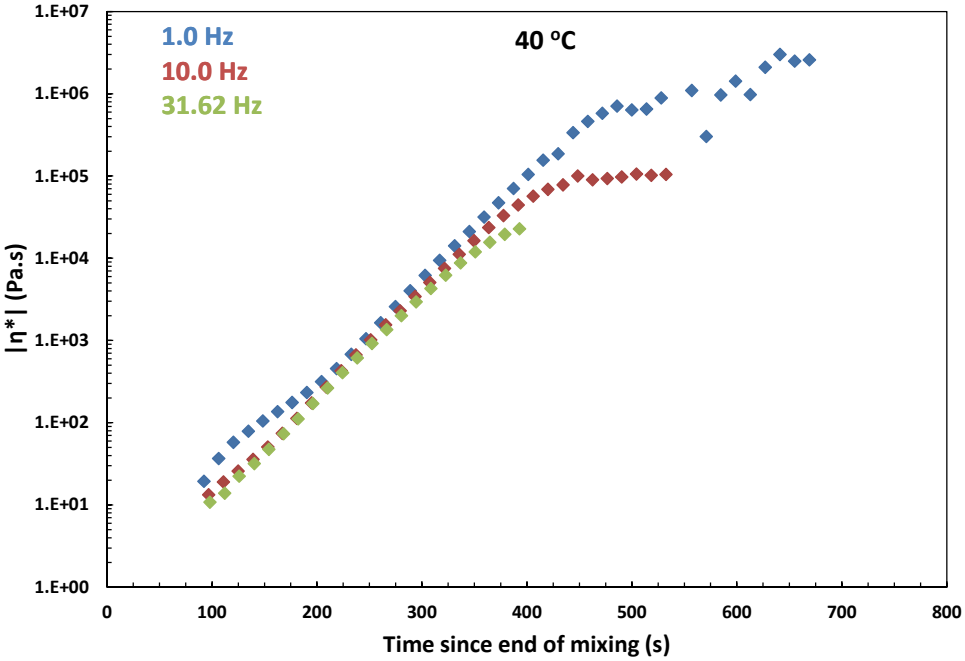

Figure 24. Dynamic viscosity dependence on frequency.

4.2.2. Parameter Fitting

Equations 15 and 16 are used to describe the data. The best fit of the data was achieved with the following parameters, as will be shown in this sub-subsection:

E_η / R (K)= -1549.4

η_{00} (Pa-s)= 600.

z = 1.0

x = 6.0

$$\xi_c = \left(\frac{CT}{CT + e^{-BT}} \right)$$

C = 1×10^{-9}

B = 0.0525

where T is in Kelvin.

The Arrhenius parameters are determined in a similar manner to that described in Section 3.2.2 (Figure 25 and Figure 26).

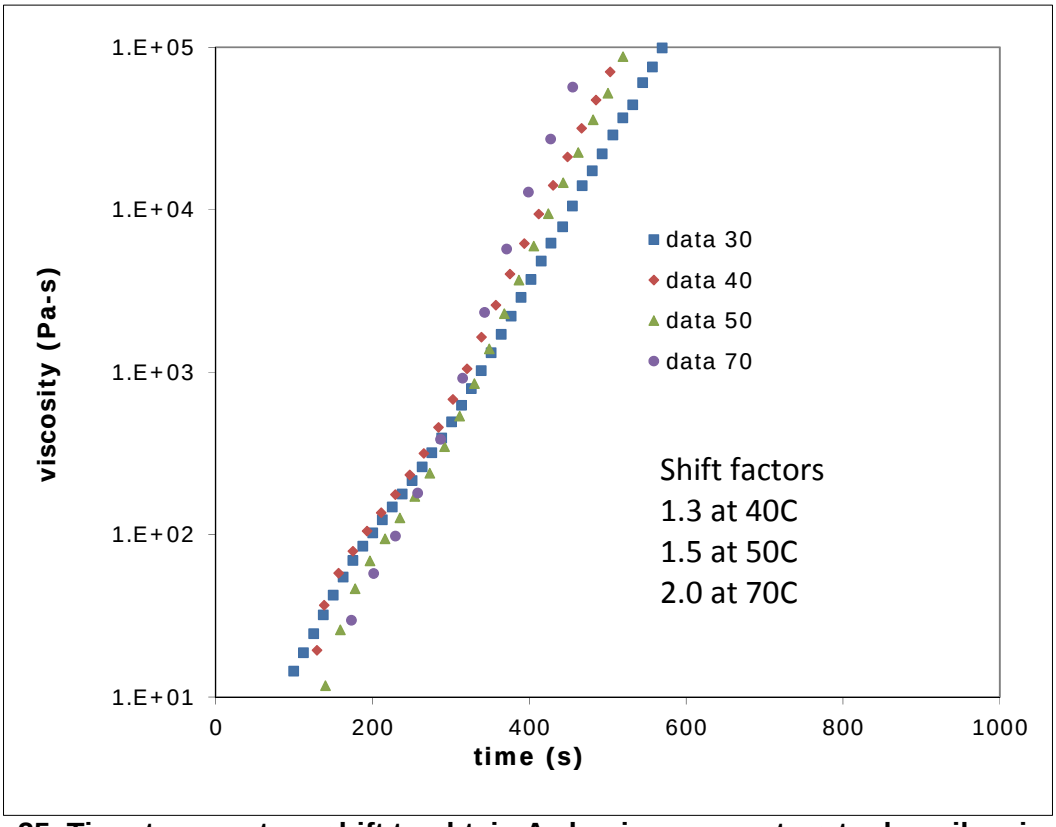

Figure 25. Time-temperature shift to obtain Arrhenius parameters to describe viscosity for temperatures from 30-70 °C.

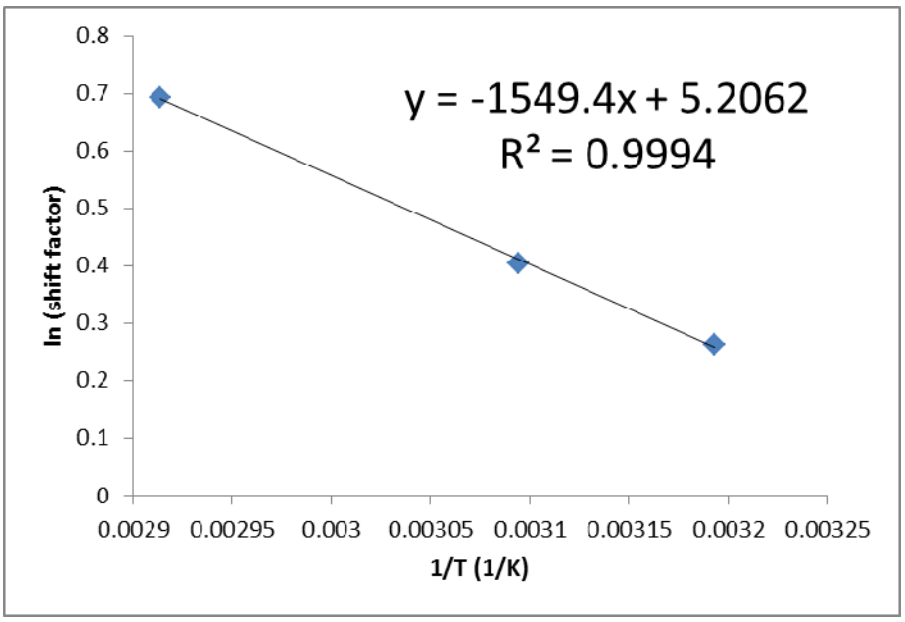

Figure 26. Activation energy (E_η/R) given from viscosity time shift factors. Here, E_η/R=-1549.4 K

From the dynamic viscosity data we estimated the time of gelation at several temperatures (30, 40, 50, 70°C). A typical method to approximate the gelation time involves plotting the ratio of G''/G' *vs.* time for data collected at various frequencies. The time at which all data cross (where G''/G' is independent of frequency) is typically the gelation time [Chambon & Winter 1987]. However, this fails for our rheology data, and instead we estimated the gelation time to be near the time the foam expansion ends and on the shoulder of the G'' curve. This is near the second crossing of G' and G'' at 30°C at low frequencies (1 Hz) as illustrated in Figure 21; however, that seems to be fortuitous because the timing is not consistent across frequency and temperature. This method is similar to that described by Harran and Laudouard [1986]. The gelation times are then compared to the extent of polymerization at those times in the IR experiments to estimate ξ_c as a function of temperature in equation 15. ξ_c is then refined as an adjustable parameter to better fit the viscosity data. Figure 27 shows the best fit values and the equation $\xi_c = \left(\frac{CT}{CT + e^{-BT}}\right)$. This form was chosen simply to ensure that the critical extent is always between zero and one.

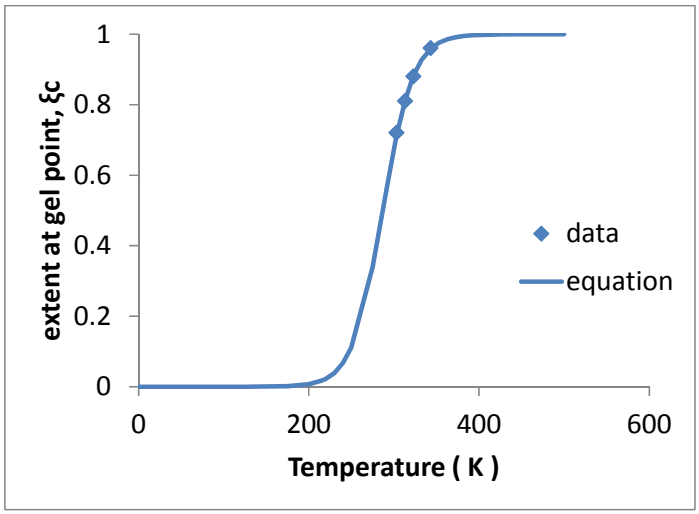

Figure 27. Fit for the critical extent of reaction at the gel point.

The resulting model for the continuous phase viscosity (equations 15, 16, with the parameters listed at the beginning of this subsection, and equation 20, with the parameters listed in 3.2.2) can be seen in Figure 28. Here we assume that the temperature of the material is 30°C until it is loaded into the rheometer, at which time it quickly reaches the testing temperature. The effect of this time can be seen in the 50°C data, where the 0.1% strain data was taken on material loaded 35s earlier than that of the 5 Pa stress data. The earlier temperature rise leads to higher predictions in viscosity, as is also seen in the data. Note that the viscosity at vitrification is infinite, although the rheometric data tends to become noisy and roughly constant as the machine reaches the limit of its ability to measure the behavior.

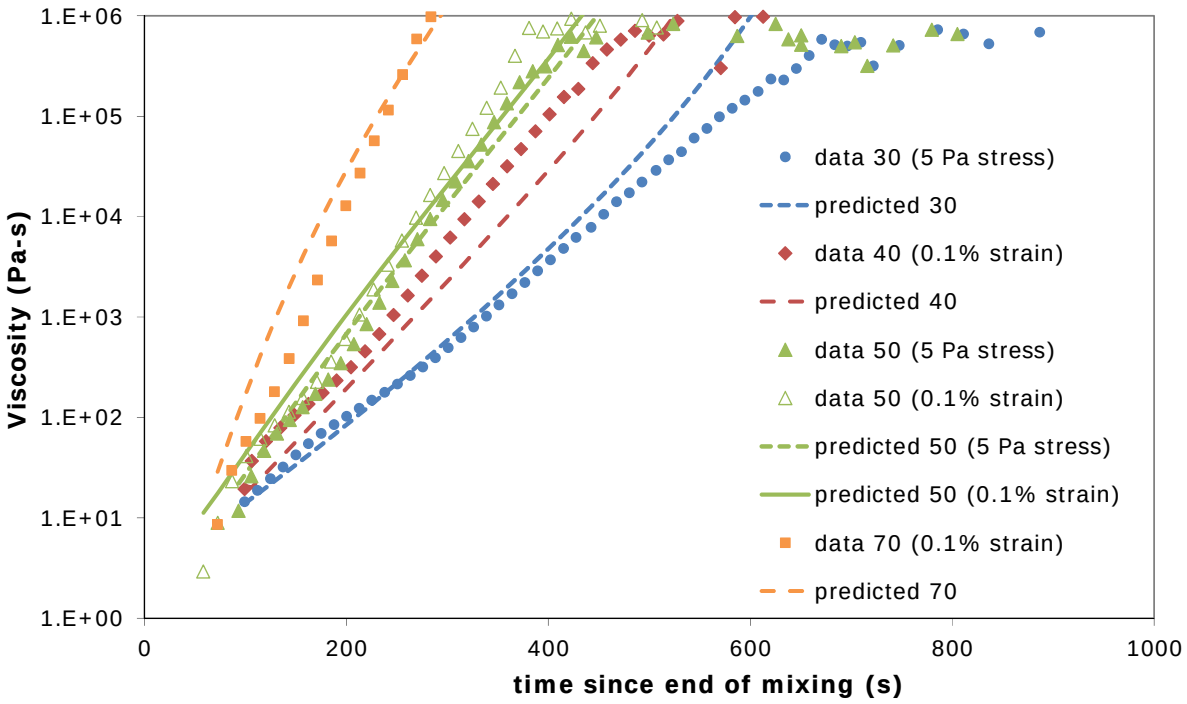

Figure 28. Comparison of rheology data for the dry foam material and equation 15 for the continuous phase viscosity.

4.3. Foaming Material

4.3.1. Steady Shear Viscosity

As illustrated in Figure 21, the foaming material does not follow the Cox-Merz rule; therefore, we test its rheology using steady shear in a parallel plate geometry. Earlier tests on the 44307 PMDI-4 encapsulation foam showed that polyurethane foam is very shear thinning, presumably due in large part to bubble breakage at the higher shear rates [Mondy et al. 2013a]. The data were reproducible at the two lowest shear rates (0.001 and 0.01 s^{-1}), but at higher shear rates ($\geq$ 0.1 s^{-1}) the bubble breakage caused large scatter and a much reduced apparent viscosity, especially at later times when the gas fraction was high. For the structural BKC 44306 PMDI-10 foam it was confirmed that the measured shear viscosity was independent of shear rate at 0.01 s^{-1} and below (Figure 29). At the lowest shear rate (0.001 s^{-1}) the rheometer could not get consistent data at early times. The currently implemented model ignores shear thinning; therefore, we do not explore that effect here, but instead take the data at 0.01 s^{-1} as representative of the foam viscosity.

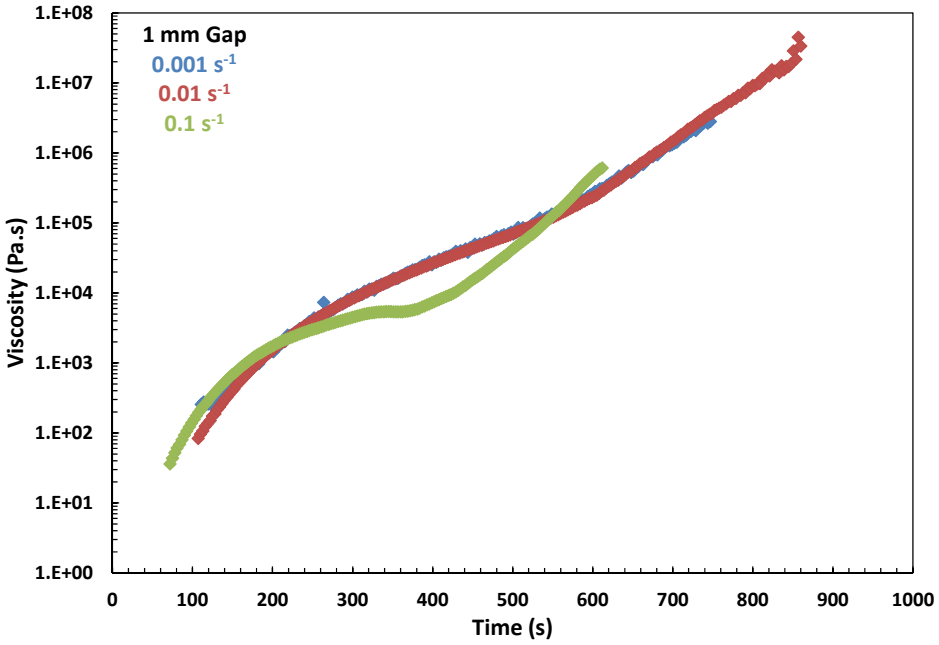

Figure 29. Apparent viscosity for the BKC 44306 PMDI-10 foam at various steady shear rates.

The choice of the height of the gap between the parallel plates can be important because it must result in a representative number of bubbles across the gap and yet not be so large that the liquid fails to span the gap or the temperature control is compromised. Thinner gaps also give a more uniform shear rate in this geometry. Preliminary tests showed that the foam sometimes failed to span the gap at early times with gaps larger than 2mm. Measurements of the temperature within the foam showed that at a gap of 1mm, the foam temperature reached the plate temperature almost immediately and maintained a steady value during foam expansion. SEM imaging [Mondy et al. 2013b] has shown that the bubble size is on the order of 100 μm; therefore, a gap size of 1 mm allows on the order of 10 bubbles to span the gap. Foams also are susceptible to slip at walls, and slip can be detected by varying the gap between the parallel plates of the rheometer [Yoshimura & Prud'homme 1988; Ekere, et al. 2001]. Figure 30 shows that there is an effect of gap size with steady shear (dynamic testing showed no discernable effect of gap size within this range, however). A slip layer can result in the measured apparent viscosity being lower than the real viscosity. Correcting for the slip layer using the method of Ekere et al. (2001) requires only two gap sizes. These corrections resulted in higher viscosity values but with a similar spread in the results depending on which two gap sizes were used to collect the data. The corrections are difficult to apply when the material is changing (due to cure and gas evolution) in time. (Ekere and coworkers only looked at stable values of apparent viscosity despite the fact

that their test material was somewhat thixotropic.) The inconsistencies may also come from the fact that the foam is continuously overflowing the fixture, during which the rheological response can be dominated by the radial flow of the foam. Finally, Zhang et al. [1998] showed that excess foam outside the fixture produced about a three-fold higher apparent modulus than if the foam were trimmed. Unfortunately, continuously trimming the foam is impractical in our experiments. Initially there is no foam outside the fixture and then the amount grows with time, making its effect difficult to quantify. Because the increase in apparent viscosity values due to the excess foam outside the fixture is potentially larger than the decrease in values potentially caused by slip, we chose to ignore the possible effect of slip.

Somewhat arbitrarily, then, we chose a gap of 1.0mm to test equation 14. Despite the very large uncertainty in the absolute value of the viscosity at any one time, and the sensitivity shown in the previous subsection to the loading time, the measurements were surprisingly reproducible, even when taken weeks apart. The viscosity changes about 5 orders of magnitude during the foam expansion; therefore, even a three-fold uncertainty in the absolute value is small compared to the effect of cure and gas fraction.

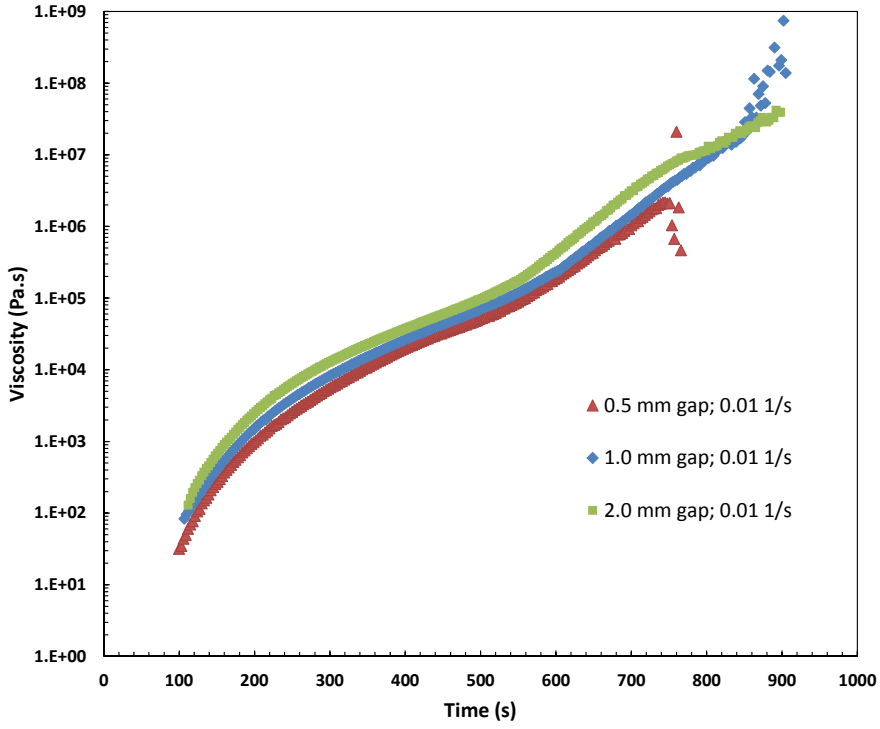

Figure 30. Apparent viscosity measured at 0.01 s^{-1} with three different gaps

Measurements taken (at 0.01 s^{-1} and with a gap of 1 mm) at five temperatures from 30 to 70°C in increments of 10°C are shown in Figure 31. Measurements were taken until the data became inconsistent around a viscosity of about 1×10^7 Pa s, which we presume is near vitrification, and is several minutes after the foam has stopped expanding. For example, at 30°C the foam stops expanding about 5 minutes after mixing the two parts, and at 50°C it stops after about 2.5 minutes.

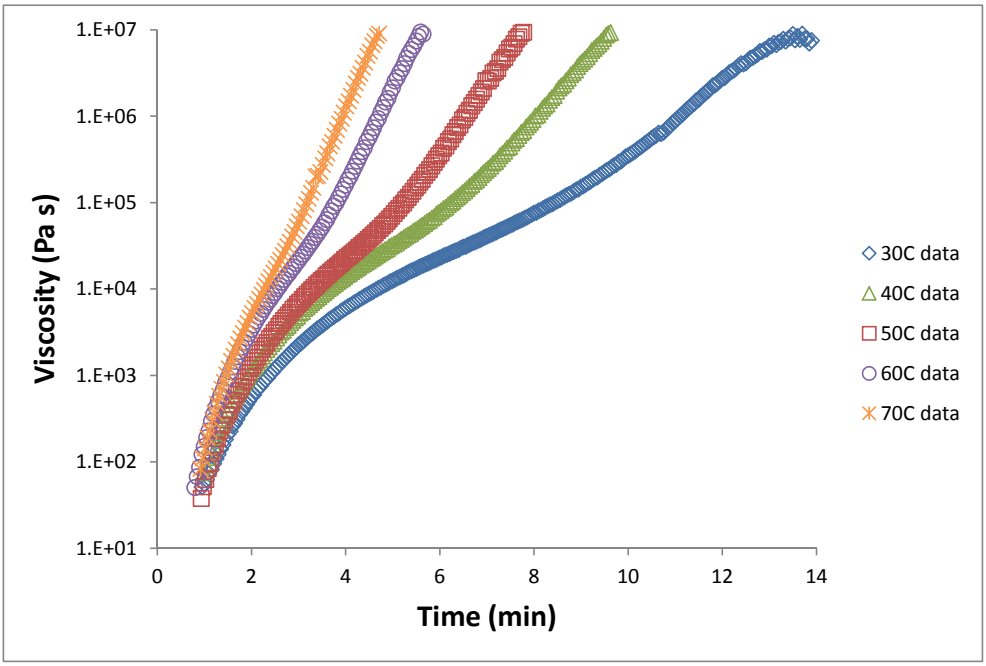

Figure 31. Apparent viscosity of the BKC 44306 PMDI-10 foaming system as measured during foam expansion (time=0 is when mixing ends).

The Taylor-Mooney equation 14 is thought to be valid for emulsions up to a discrete-phase volume fraction of about 0.5. We tested this form by using the model results of the previous subsection for the continuous phase viscosity as it changes with time combined with the predicted gas fraction derived with the model presented in Section 3.3.3. This presumes that the fit to foam density in our channel would be valid for the density in the rheometer, which has a smaller characteristic width. Results obtained when assuming a constant temperature of 30, 40, or 50°C are shown in Figure 32. Although the foam is molded between 30 and 40°C, the exothermic reaction can drive the temperatures higher in thick sections of a mold. The predicted extent of polymerization is shown for reference (pink line), as are the times (vertical lines) that

the foam is predicted to hit a gas fraction of 0.50 and 0.75. The blue (predicted) curve matches the green (measured) curve reasonably well, especially considering the uncertainty in the rheology data, until the foam has almost stopped rising (around 300s). From equation 13, one can see that for a typical structural foam over packed so that the final density is 40 pcf (0.64 g/cm^3), the gas fraction will only reach about 0.45 at 30°C. In this case the Taylor-Mooney formulation would work for a simulation as long as the gas fraction did not go higher locally. On the other hand, notice that the gas fraction of a free-rise 10 pcf (0.16 g/cm^3), foam at 30°C is about 0.86. In that case the predicted viscosity is too high, as the measured viscosity begins to be dominated by the continuous phase viscosity beyond the gel point. This may be due to bubble breakage, however, and an artifact of the measurement technique. As previously mentioned, the model and parameters presented here are designed to be used only during the foam expansion.

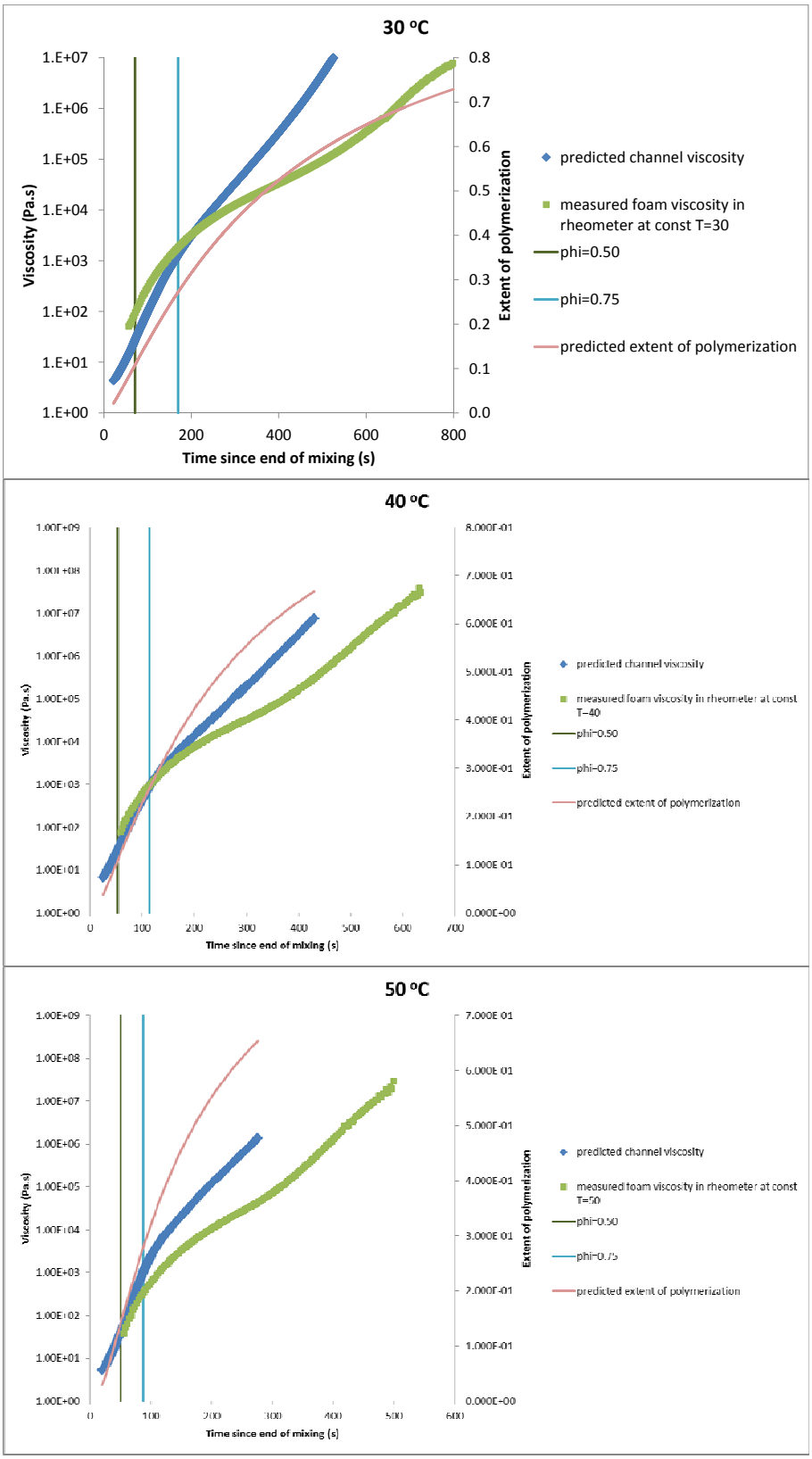

Figure 32. Predictions of foam viscosity using the Taylor-Mooney form coupled with predictions of extent of polymerization and concomitant change in continuous phase viscosity and extent of the gas formation reaction.

5. THERMAL

5.1. Heat of Reaction

The heat of reaction was measured with DSC for both the dry material and the full system including H_2O, in order to determine if the assumption in equation 5 that the heat depends primarily on the polymerization reaction is reasonable. Table 3 shows the results of several tests with each material. Within the error of the measurements, the heat of reaction is the same with or without the foaming reaction, probably because the foaming reaction involves very little mass.

Table 3. PMDI BKC 44306-10 heat of reaction by DSC

"Dry" nonfoaming		***PMDI BKC 44306 PMDI-10***	
Run #	**J/g**	**Run#**	**J/g**
1	189.7	1	173.6
2	155.0	2	169.9
3	186.9	3	178.9
4	205.4	4	201.8
5	188.6		
Average	185.1	Average	181.1
Std. Dev.	18.4	Std. Dev.	14.3
CV (%)	9.9	CV (%)	7.9

5.2. Heat Capacity

Heat capacity measurements at temperatures between 0 and 160 °C were made on the dry nonfoaming material using DSC (Figure 33). The DSC was calibrated prior to the measurements, and the heat capacity per unit mass of a standard (indium) was measured to check the calibration. We also reproduced previous data for EPON828-DEA cured epoxy as an additional check for accuracy with a polymeric material.

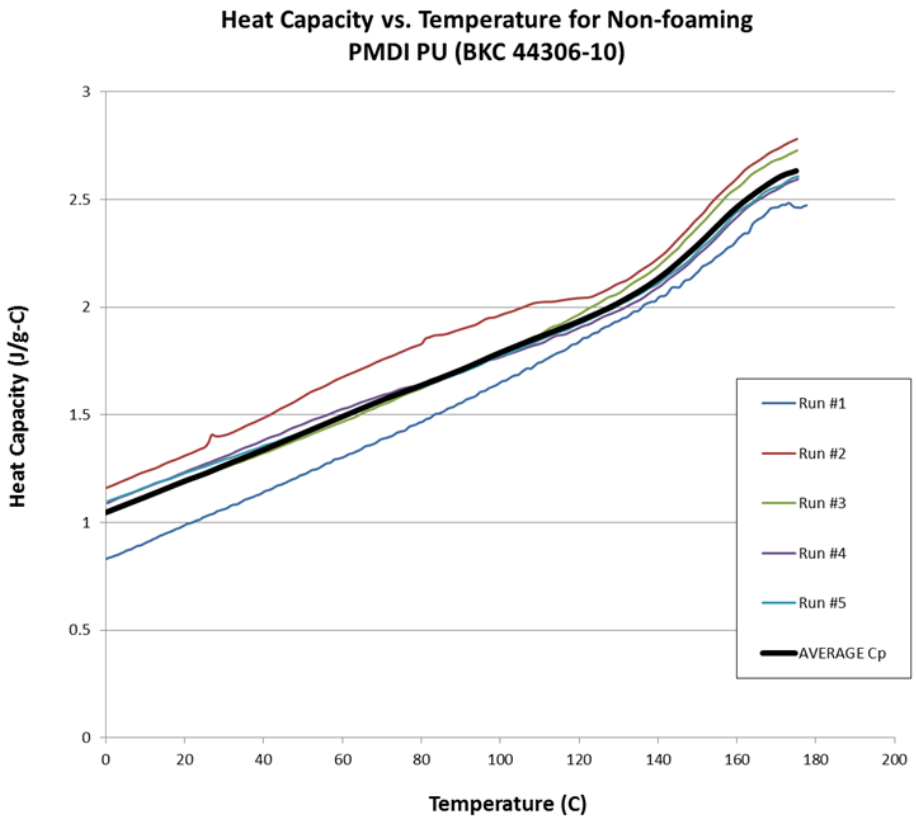

Figure 33. Heat capacity per unit mass of the dry (non-foaming) BKC 44306 PMDI.

Independent measurements at three temperatures (26, 60, and 90°C) were taken with a Hot Disk® sensor (Thermtest Inc., Fredericton, NB, Canada) on cured BKC 44306 PMDI-10 foam samples, molded in a 5 cm-diameter cylinder to final densities ranging from 0.19 – 0.42 g/cm^3. Details of these measurements are included in the Appendix. The foam samples were blown and cured according to the KCP protocol. Here, the sensor was sandwiched between two halves of the sample. This method was used in conjunction with the determination of thermal conductivity in the next subsection. The method is best suited to materials with smooth surfaces in order to get good contact with the sensor plate, so foam samples were cut and polished. Using a polynomial fit to the average data in Figure 33 as the temperature-dependent heat capacity per unit mass of the continuous phase ($C_{p,liquid}$), we can compare the measured heat capacity per unit mass of the foam samples to the mixture theory equation 18 (Figure 34). The polynomial used is:

$$C_{p,liquid} = 2.49\times10^{-7}T^3 - 2.48\times10^{-4}T^2 + 8.89\times10^{-2}T - 9.85\,, \qquad (27)$$

where T is temperature in Kelvin and the R^2 value of the fit is .999. Unfortunately, the data for BKC 44306 PMDI foam (Figure 34) appear to depend on the density of the foam, which is not

predicted by equation 18. This is in contrast to similar measurements made on the encapsulation polyurethane foam BKC 44307 PMDI, which showed little if any dependence on density, although the scatter encompassed almost the range of values in the structural data. The samples were weighed before and after measurements and the mass remained constant; therefore, the dependence on density is not attributable to off-gassing or other loss of mass during the testing temperature ramps. A second set of data were taken on dry material, this time using the same Hot Disk® instrument as recorded the lower density foam data in Figure 34. These values are also shown in the figure following the trend of decreasing heat capacity per unit mass as the density increases. At the present time this effect is unexplained.

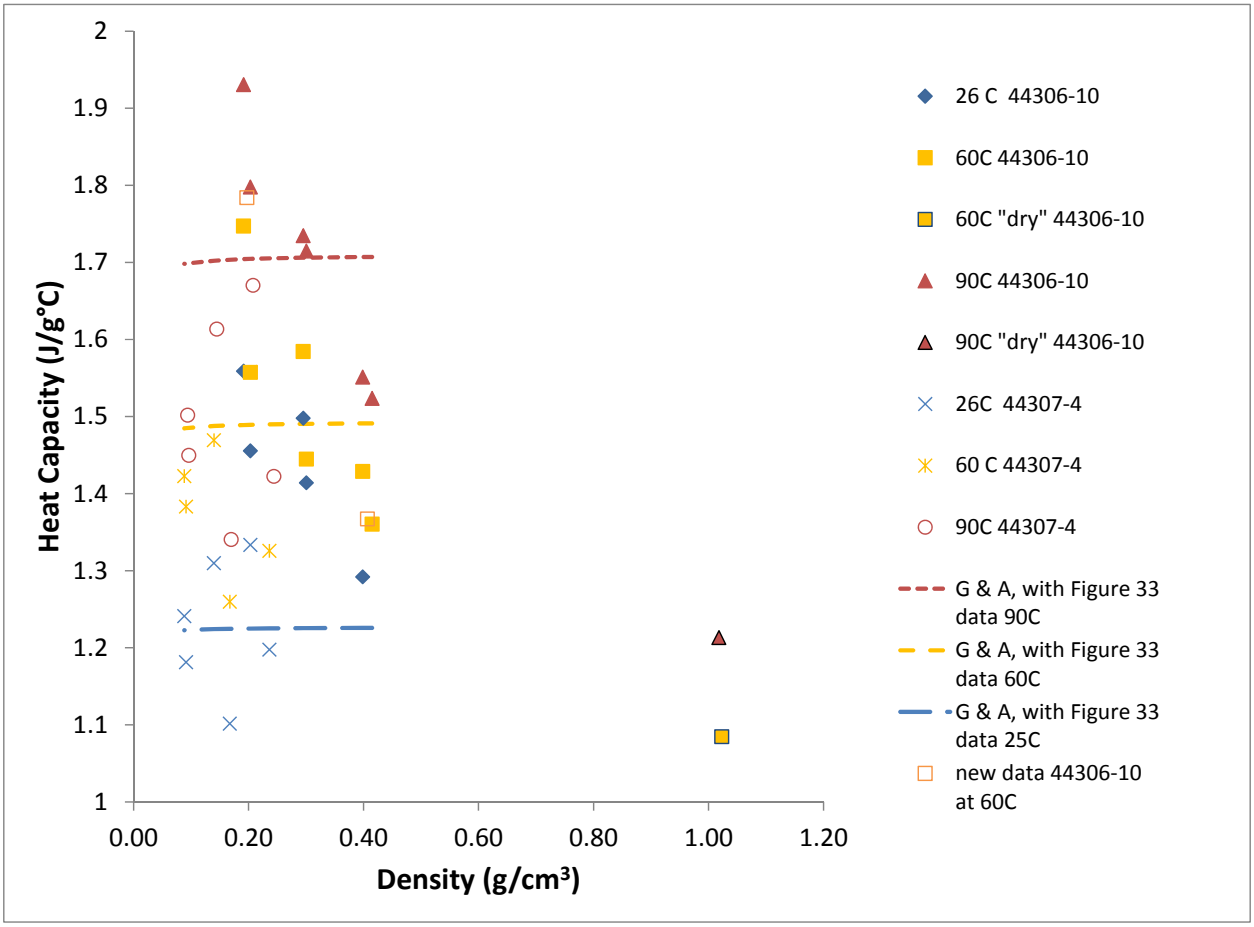

Figure 34. Measured heat capacity per unit mass of solid structural foam samples molded to four densities. Dotted lines are the results of equation 18 [Gibson & Ashby 1990] combined with DSC measurements as the value for the continuous phase.

The results of equation 18 are reasonable in the range of densities expected.

5.3. Thermal Conductivity

Thermal conductivity measurements were made on the same cured foam samples as used in the previous subsection and are described in the Appendix. Measurements were made at ambient pressure and moisture conditions using a transient method based on the theory of the transient plane source technique. Here, the Hot Disk® sensors (Thermtest Inc., Fredericton, NB, Canada), sandwiched between two sample halves, served as a heat source to increase sample temperature and as resistance thermometers for recording temperature increase over time. Figure 35 shows the thermal conductivity as a function of temperature for a nonfoaming sample. For each test a value is obtained for the upper layer (red) and the lower layer (blue). These results could potentially be used to approximate k_{liquid}. Because it is impossible to make a sample completely free of bubbles, we estimate the value of k_{liquid} by extrapolating the full set of data to the original liquid density (1.18 g/cm^3). Results are shown in Figure 36 and compared to equation 19.

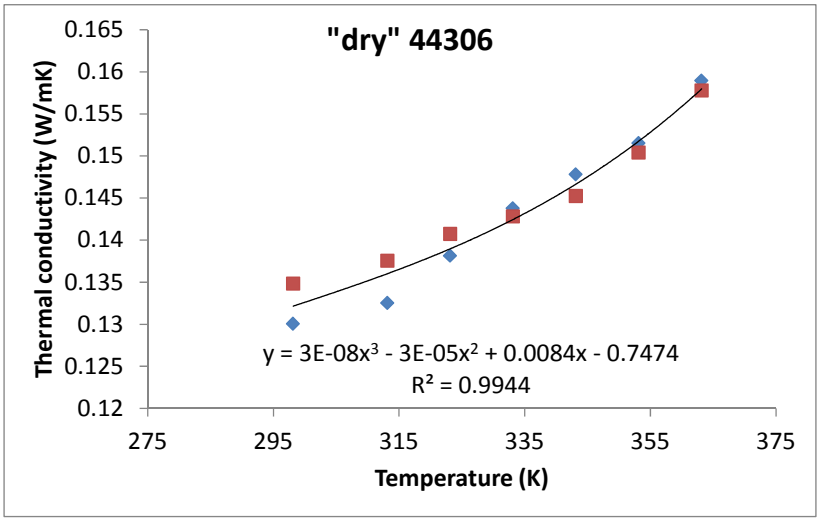

Figure 35. Thermal conductivity for a cured sample made from dried material that does not foam.

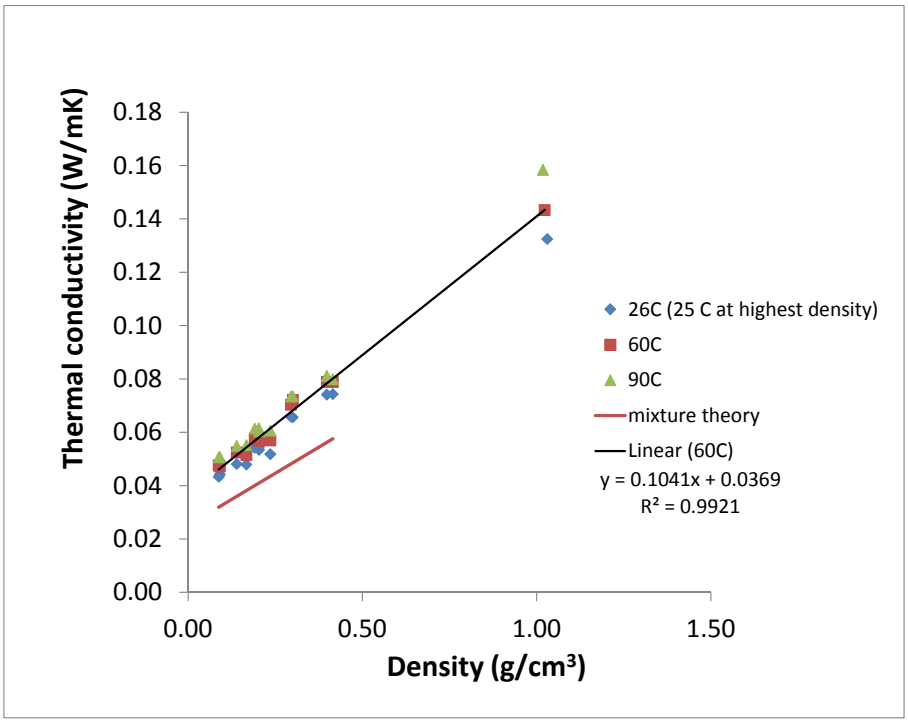

Figure 36. Thermal conductivity at three temperatures for several densities of foam. The red line shows results of equation 19 for the thermal conductivity at 60°C, using the linear equation on the graph to predict the value of k_{liquid} from the solid value at a density of 1.18 g/cm^3.

The values for the mixture theory appear to trend with density in approximately the correct way; however, these underpredict the measured data. Historical data on polyurethane foams are compared with this study's values in Figure 37 [Gill & Hanks, in Mondy et al. 2010]. Sandia National Laboratories (SNL) values are for an 8-pcf PMDI foam, probably BKC 44307 encapsulation foam PMDI-4 or PMDI-6 molded to 8 pcf. These values were taken by heating a six-inch diameter sample disk and measuring time-temperature histories in a technique described by Dobranich et al. [2005]. This technique, although still available, requires much larger samples, and a current shortage of material precluded its use in this current study. The 9.4-pcf foam was tested with a laser flash technique by the Thermophysical Properties Research Laboratory (TPRL), and the uncertainty in these values is unknown. Both sets of historic data are below the more recently obtained data. However, the actual densities of the historic samples are unknown.

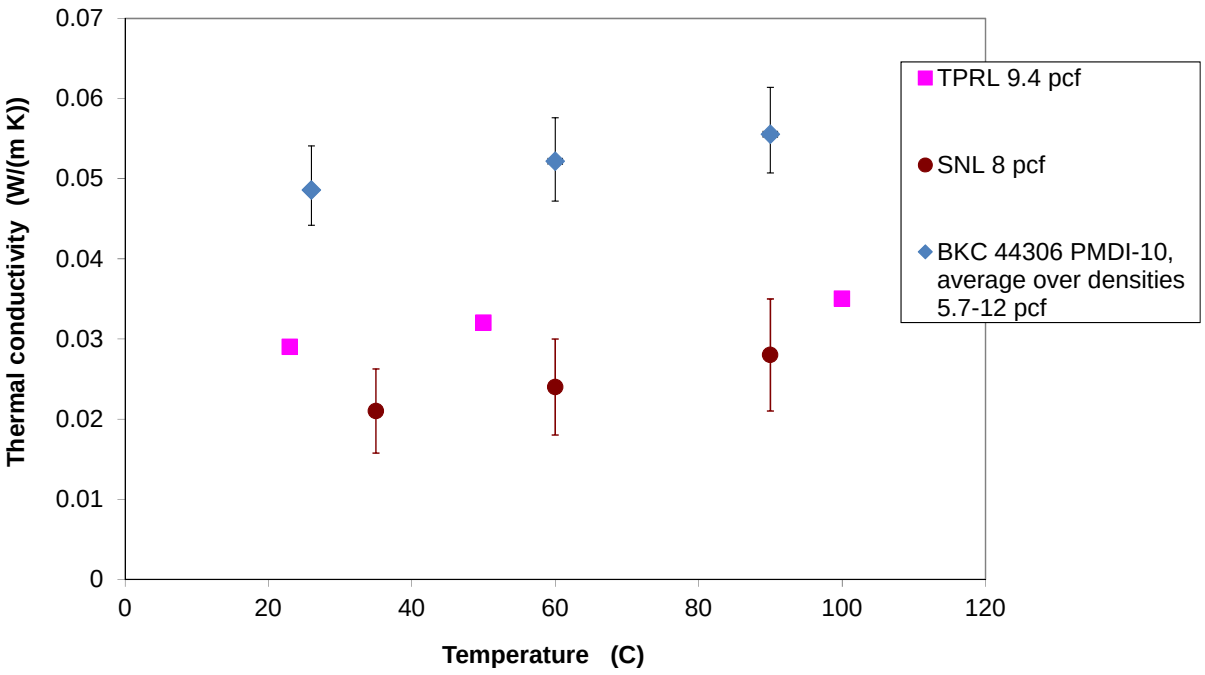

Figure 37. Thermal conductivity of polyurethane foams [Gill & Hanks, in Mondy et al. 2010] from Sandia National Laboratories for an 8 pcf PMDI foam and from the Thermophysical Properties Research Laboratory for a 9.4 pcf polyurethane foam measured with a laser flash technique compared to the average result from a subset of this study over the density range listed (an average density of 9.2 pcf). Error bars for BKC 44306 are the range of values measured over this density range.

6. DENSITY VARIATIONS

One goal of this work is to provide data to validate an improved model that can better predict density variations in the final structural foam part. To this end we have measured the density with height of several of the bars molded in the volume-*vs.*-time experiments described in Section 3.3, as well densities within as a more complex mold developed by KCP as a quality assurance tool. With the simple bar geometry we can cut the bar into pieces, measure, and weigh them to obtain densities within a section of the bar. We can also use x-ray computed tomography (CT) to determine the spatial density variations. Both types of data collection have advantages and drawbacks. Taking the final part out of the mold can lead to error in mass and volume, as mold release can infiltrate the pores or a rough surface can make volume measurements inaccurate. The CT has higher resolution and can be used easily on complex geometries, but edge effects can influence the calibration. The average density can also be

compared to the value obtained through the image processing in Section 3.3 to help evaluate the uncertainties in the measurements.

6.1. Bar Geometry

Three sections approximately 0.25 cm high were cut from representative bars molded in the experiments described in Section 3.3. Figure 38 shows the locations of these samples. The maximum height of a bar made in this mold is 7 3/8 inches (18.73 cm), but most free-rise experiments result in shorter bars. The foam made at 30°C was very fragile and the samples in the middle region crumbled before density could be measured. Results are compared to the image processing measurements in Figure 39, showing that the overall density is a function of the mold temperature during the foam expansion. The spread in the data is a consequence of the density variation from top to bottom of the bar, as shown in Figure 40. In all cases the density is highest near the bottom of the bar and lowest near the top, consistent with possible "creaming" of the lighter material to the top and draining of liquid to the bottom, but opposite of what has been observed with lower density encapsulation foams.

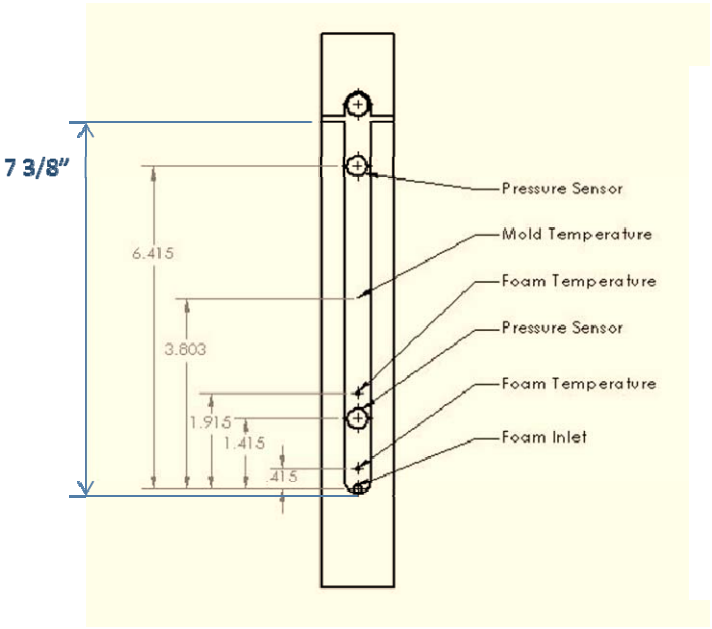

Figure 38. Locations (right) of the three samples cut from bars of BKC 44306 PMDI-10 relative to the inlet port for the experiments described in Section 3.3 for the mold pictured on the left. All dimensions pictured are in inches.

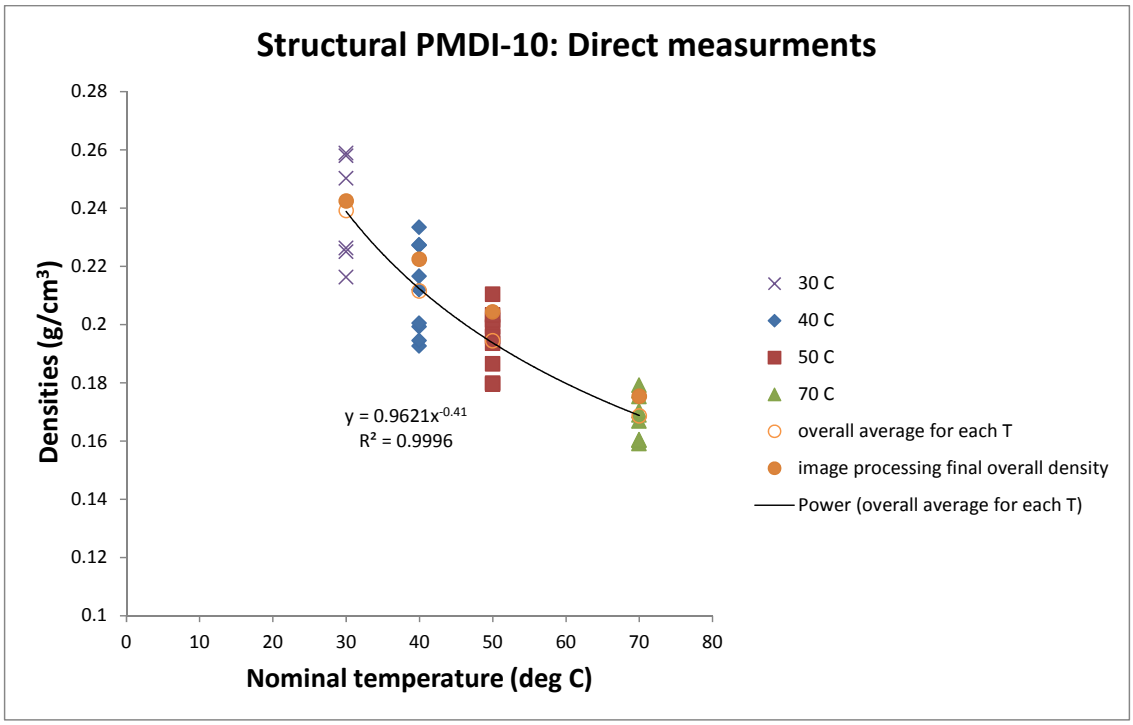

Figure 39. Densities measured in Section 3.3 from image processing at the end of foam expansion and from cutting representative samples at several locations (three replicas at each location).

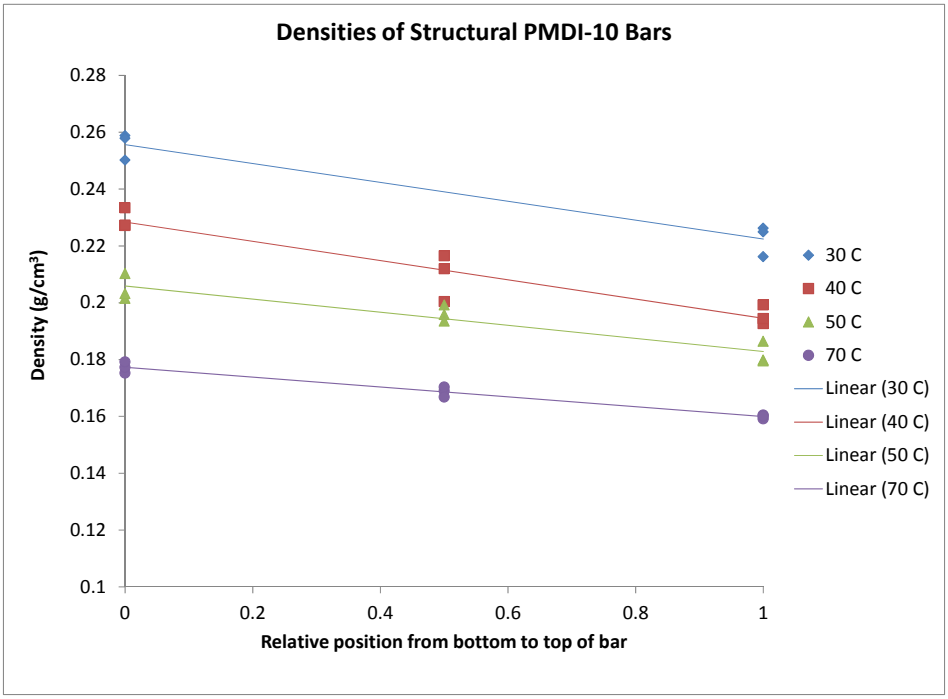

Figure 40. Densities of samples taken at locations described in Figure 37. Lines are to guide the eye.

X-ray CT was also performed on representative bars. An x-ray image from this work is shown in Figure 41, where samples #1 and 2 are the same free-rise BKC44306 PMDI-10 foam samples molded at 30 and 50°C, respectively, as in the previous figure. Sample #3 is the same foam molded at 30 °C but overpacked to a nominal density of 0.32 g/cm3 (20 pcf), although some leakage occurred leading to a slightly lower density. In all samples fairly large voids can be seen.

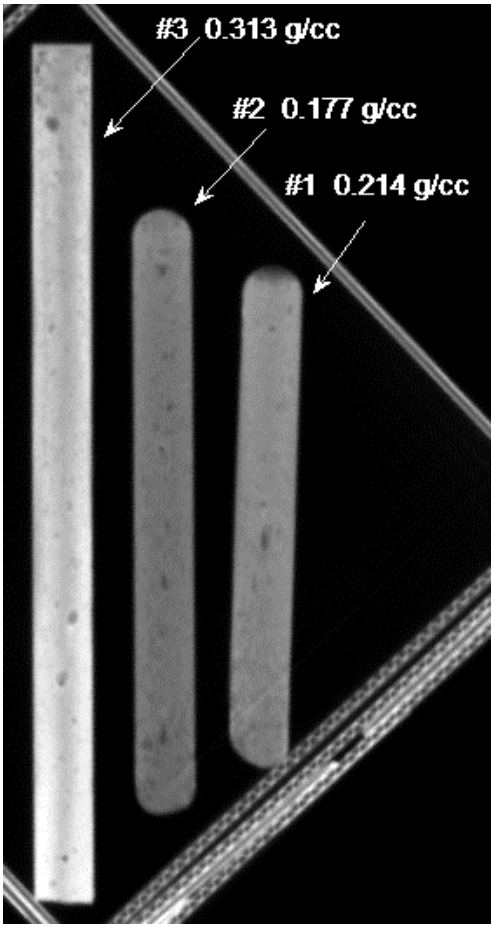

Figure 41. X-ray image of several bars of BKC 44306 PMDI-10 foam. 1) free rise at 30°C, 2) free rise at 50°C, 3) 2 times over packed at 30°C.

Four samples of foams were molded to different densities, cut and weighed, for use as calibration objects. The average intensity of the x-ray image of each of these calibration objects was then calibrated to the sample density, as shown in the calibration (Figure 42). The profiles of intensities measured in the bars show variations from the arrangement of larger bubbles, as the examples from samples #1 and 2 in Figure 43 show. The x-ray data seems to be consistently

lower than the image processing or direct weight measurements, although much more subtle variations can be seen by using the x-ray CT technique.

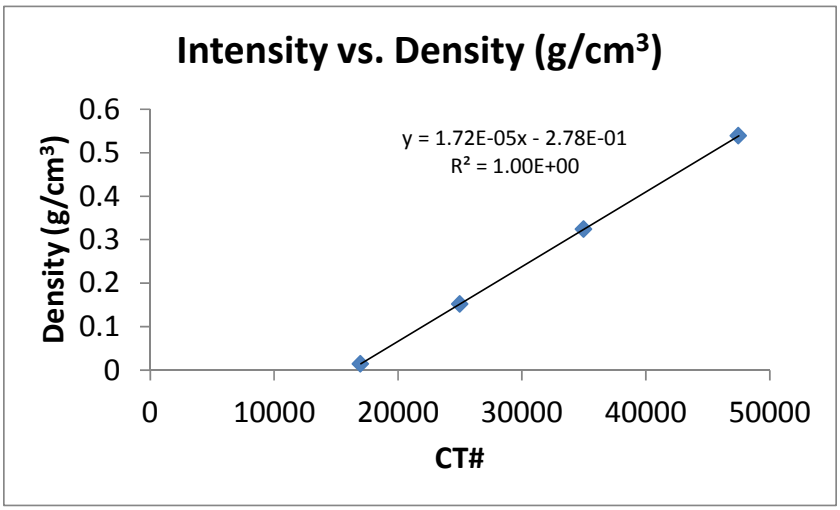

Figure 42. Calibration of x-ray intensity, showing almost perfect correlation to material density.

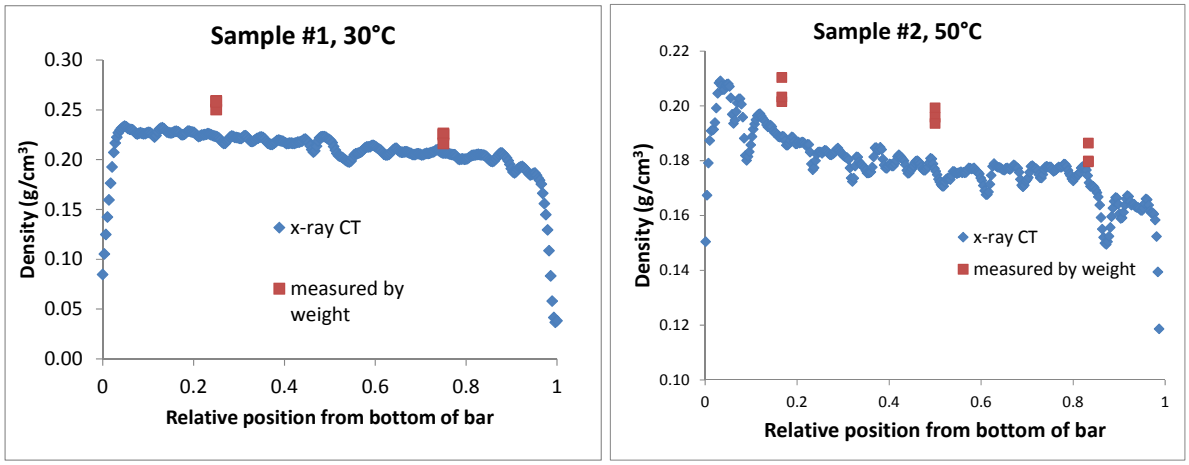

Figure 43. X-ray measurements of density profiles compared to the direct weight of samples cut from sections of the bar.

Sample #3 shows the same trend in density from highest at the bottom to lowest at the top, even though the foam was double packed (Figure 44).

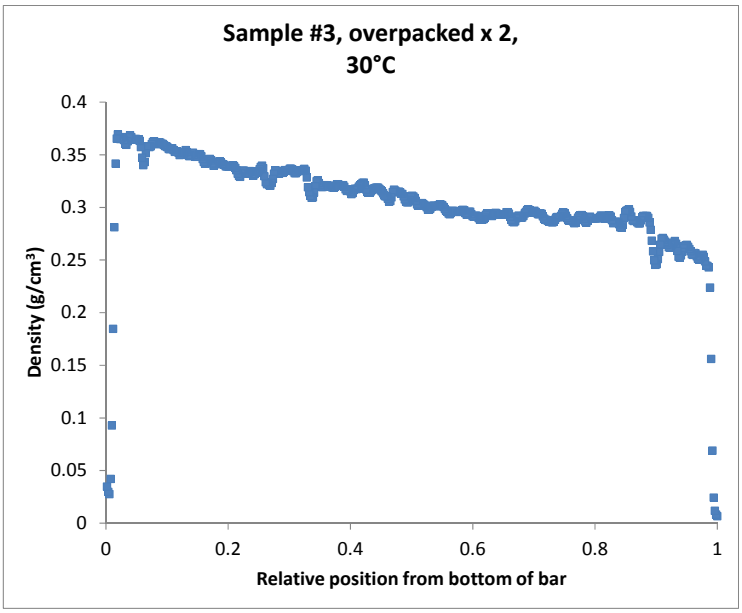

Figure 44. X-ray measurements of density profile in a bar packed to double density.

6.1. KCP Quality Assurance Mold

A second mold that we will call the "KCP" mold was based on a quality assurance tool developed by the Kansas City Plant (Figure 45). A complex channel is machined in an aluminum block and a clear acrylic cover is held on the front face with screws. To monitor the quality of the foam during an encapsulation process at Kansas City, this mold is filled with the foam encapsulant and monitored to make sure that it fills the part. Filling is through injection ports in the left hand corner of either the inner cup shape or the outer serpentine shape. The outer mold, consisting of narrow sections and serpentine routes for the foam to penetrate, was used for our studies. This outer mold is about 1.9 cm (3/4 inch) deep and has a volume of about 59 cm^3. The serpentine area at the top is usually broken off when getting the part out of this mold, so is not imaged in the x-ray CT shown in Figure 46. In this image, one can see that the density is not monotonically decreasing with height, but instead has regions of higher density after narrow contractions. The lowest region is also the largest and susceptible to a higher temperature from the exothermic reactions, lowering the resulting density.

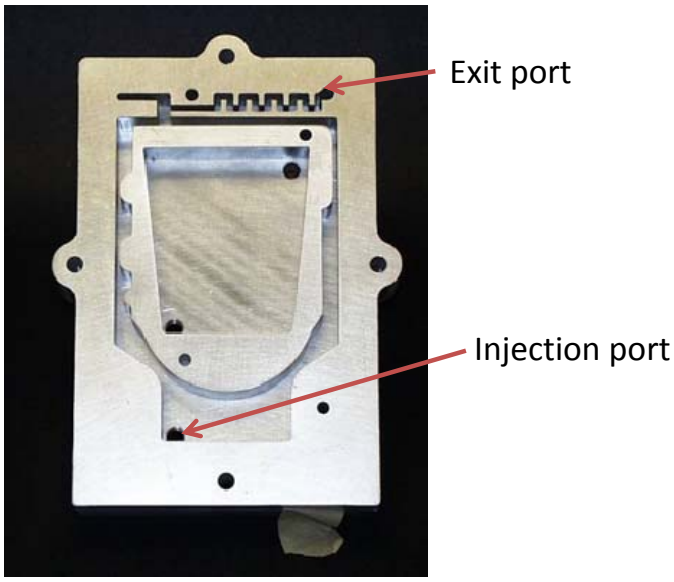

Figure 45. KCP mold.

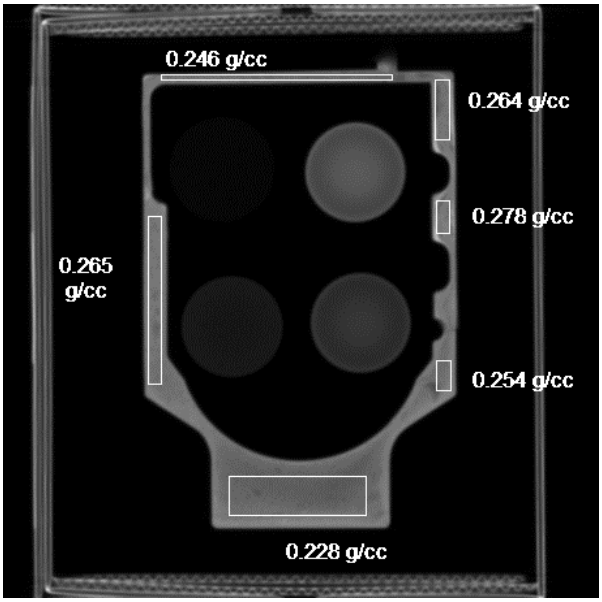

Figure 46. X-ray image of KCP mold and the reference objects used to calibrate the densities. Average densities within the boxed regions are given.

7. SUMMARY AND CONCLUSIONS

We have presented data needed to develop and parameterize models with which to predict the polymerization and foaming of polyurethane. The polyurethane of interest, BKC 44306 PMDI-10, is used to manufacture structural parts. It is a chemically blown foam, where carbon dioxide

is produced via the reaction of water and isocyanate. The isocyanate also reacts with polyol in a competing reaction, which produces the polymer.

The polymerization is tracked with IR spectroscopy, and the foam blowing reaction is studied by measuring the volume and pressure increase with time and temperature. The IR data are fit to a condensation chemistry form with four parameters. The data are described well by this model for the first 1000 seconds or so. However, gelation slows the kinetics and the equation predicts continued polymerization at a rate faster than observed. Therefore, for use in models attempting to capture behavior after the foam expansion phase, a more complex reaction rate form is needed and will be the subject of future studies.

The foam-rise experiments used to determine the reaction rate of the gas forming reactions are less definitive than the IR results, since some of the carbon dioxide could be lost to the atmosphere due to bubble breakage at the surface. Also, the temperature is not constant in the experiments to measure foaming volume. In addition, we are only measuring the pressure at the walls and not measuring the true pressure of the gas in the bubbles. Interesting observations include: 1) the temperature peaks before the foam stops expanding and 2) the pressure peaks after the foam stops expanding. This implies that the foam expansion is stopped by the polymerization effect on the rheology. It also implies that the uneven heating seen in a complex geometry can result in uneven bubble sizes and inhomogeneous densities that could be locked in place by gelation. Also, the bubbles may become pressurized after the polymerization restrains the bubble expansion. This has implications in foam structural stability and material compatibility effects from gas leakage out of the foam during aging and will be another subject of further study. The data fit reasonably well to a Michaelas-Menten reaction rate form, although here, too, the reaction rate near the end of the conversion is too fast.

A viscosity model has been developed that is dependent on the extent of the two primary reactions, since it is based both on the properties of the polymerizing continuous phase and the gas fraction, both of which vary with time and temperature. The rheology of a constantly evolving material, especially one whose volume is changing, is difficult to measure and the resulting measurements are difficult to interpret. The continuous phase is approximated by a

material that is identical to the BKC 44306 PMDI-10 but has been formulated without water to prevent the foaming reaction. The effect of the increasing viscosity of the continuous phase as it polymerizes is modeled in a similar manner to that used in the past for curing epoxies [Adolf 1996], and this condensation chemistry form fits reasonably well but not perfectly. The most difficult aspect to choosing the parameters is choosing the critical extent of reaction, which depends on temperature. We use this as another fitting parameter, although we make sure that the values are reasonable in relationship to the extent of polymerization when the foam expansion stops.

The shear viscosity of the full foaming system is also measured and related to that of the dried material through a Taylor-Mooney relationship. Here, no attempt is made to quantify shear thinning or other rheological changes due to the microstructural changes such as bubble stretching and breakage. This is an area that needs further study, especially in light of density measurements that indicate microstructural changes must occur in squeezing flow in narrow channels. For low shear rates the predictions of viscosity match reasonably well to data for a gas volume fraction of between 0.5 and 0.75 (usually within the gas volume fractions expected in a real application). Note that these predictions require using the reaction kinetic model to estimate the continuous phase viscosity and the gas formation kinetic model to estimate the gas volume fraction and then the Taylor-Mooney relationship to predict the overall foam viscosity. At higher gas fractions the viscosity predictions are too high, but the foam movement has essentially stopped anyway and is insensitive to the absolute value of these high viscosities.

Thermal properties are also difficult to resolve for evolving multiphase systems. We approximate the properties from those of the final solid foam. Even for the solid, it is difficult to accurately measure properties in porous materials. We present new measurements for heat capacity and thermal conductivity and compare them to values obtained in the past for similar materials. Uncertainties in these values are apparently fairly large because they depend on the measurement technique. Sensitivity of computational model results to these values should be explored through a sensitivity analysis.

Density gradients in the final part made in two geometries are also measured. In complex geometries the gradients are not monotonic with height, but obviously depend on the flow and the temperatures reached during foam expansion.

The choice of catalyst and operating temperature can influence the relative rates of the two primary competing reactions. The competing reactions rates could affect the residual stresses left in the part and the behavior of the foam as it ages. For example, the dimensional stability of the material could be affected if the continuous phase remains somewhat elastic and the previously pressurized gas contracts when cooled or diffuses out of the matrix. Future work will explore these possibilities in more detail. We also intend to study the viscoelastic nature of the polyurethane to develop more sophisticated rheological models, which will help us to better understand and quantify when foam expansion is stopped and bubble pressurization.

8. REFERENCES

D. Adolf. 1996, *Measurement Techniques for Evaluating Encapsulant Thermophysical Properties During Cure*, Sandia National Laboratories, SAND96-1458.

Bouayad, R.; J. Bikard; J.-F. Agassant. *Int. J. Mater. Form* 2009, **2**,243.

Bird, R. B.; W. E. Stewart; E. N. Lightfoot. *Transport Phenomena*, John Wiley and Sons, New York, USA, 1960.

Chace, A. Personal communication to L. Mondy 12/4/2013.

Chambon, F.; H. H. Winter. *J. Rheology* 1987, **31**, 683.

Cox, W.P. ; E.H. Merz. *Journal of Polymer Science* 1958, **28**, 619.

Crowder, S.; H. Parks; J. Newcomer. Good Measurement Practices, Sandia National Laboratories class ENGR224, August 2011.

Dobranich, D.; W. Gill; K. Dowding. 2005. *Determining Thermal Properties of Low-Density Porous Materials Using a Transient Inverse Heat Transfer Approach*, Sandia National Laboratories, Albuquerque, NM, SAND2005-2950C.

Dow Plastics, "Voronol 490" Form No. 109-01280 (Published 8/2001); "Papi 27" Form No. PA-26-333-0301 (Published 3/2001).

Ekere, N. N.; D. He; L. Cai. *IEEE Transactions on Components and Packaging Technologies* 2001, **24,** 468.

Gibson, L. J.; M. F. Ashby. *Cellular Solids: Structure and Properties,* 2nd Edition, Cambridge Solid State Science Series, Cambridge University Press, Cambridge, UK, 1990.

Harran, D.; A. Laudouard. *J. Appl. Polymer Sci.* 1986, **32**, 6043.

Hilyard, N. C.; A. Cunningham, *Low Density Cellular Plastics: Physical Basis of Behavior*, Chapman & Hall, New York, USA, 1991.

Joint Committee for Guides in Metrology, JCGM 101:2008, Supplement to the "Guide to the Expression of Uncertainty in Measurement (GUM)," ANSSI/NCSL Z540-2.

Levenspiel, O. *Chemical Reaction Engineering*, John Wiley & Sons, New York, 1972.

Martin, J. P.; D. B. Adolf; J. P. Wilcoxon. *Phys. Rev. A* 1989, **39**,1325.

Martinez, M. J.; A. M. Kraynik. "Bubble Growth during Uniform Expansion of a 2D Foam," Proc. of AIChE Annual Meeting, Nov. 1992, p. 192 (extended abstract); personal communication 2005.

May, C. A., Ed., *Epoxy Resins Chemistry and Technology*, 2nd Edition, Marcel Dekker: New York, 1988.

Mondy, L. A.; M. Celina; J. Kropka; R. R. Rao; E. Russick; N. Giron; R. Cote; J. Castaneda; J. Aubert. 2010, *Novel Foam Encapsulation Materials and Processes*, Sandia National Laboratories, SAND2010-6868.

Mondy, L. A.; R. R. Rao, M. C. Celina, A. Quintana, B. Shelden, N. B. Wyatt, E. M. Russick. Proceedings of the Polymer Processing Society 29th Annual Meeting, Nuremberg, Germany, July 15-19, 2013a.

Mondy, L. A.; A. M. Grillet; N. B. Wyatt; R. R. Rao; M. Celina; M. M. Soehnel; B. Shelden; C. C. Roberts; S. Altobelli. "Evolving Rheology of Polyurethane Foam during Expansion," presentation at the 85th Annual Meeting of the Society of Rheology, Quebec, Canada, October 13-17, 2013b.

Prud'homme, R. K.; S. A. Khan. "Experimental Results on Foam Rheology," in *Foams, Theory, Measurements and Applications*, R. K. Prud'homme and S. A. Khan (Eds.); Marcel Dekker, Inc., New York, 1996; 234.

Rao, R. R.; L. A. Mondy; M. C. Celina; D. B. Adolf; J. M. Kropka; E. M. Russick. Proceedings of the Polymer Processing Society 26th Annual Meeting, Proceedings, Banff, 2010.

Seo, D.; J. R. Youn; C.L.I. Tucker. *Int. J. Numer. Meth. Fluids* 2003, **42,** 1105.

SpecialChem, http://www.specialchem4polymers.com/tds/dabco-dc197/air-products/195/index.aspx

Tesser, R.; M. Di Serio; A. Sclafani; E. Santacesaria. *J. Appl. Polymer Sci.* 2004, **92**, 1875.

Wilson, S. D. R. *Acta Mechanica* 1997, **120**, 217.

Yoshimura, A; R. K. Prud'homme. *J. Rheology* 1988, **32**, 53.

Zhang, X. D.; D. W. Giles; V. H. Barocas; K. Yasunaga; and C. W. Macosko. J. Rheology 1998, **42**, 871.

APPENDIX

U
Sandia National Laboratories
ec0

Stephen J. Bauer
Distinguished Member of the Technical Staff
Geomechanics Research Department 6914

Albuquerque, NM 87185-1033
Phone: (505) 844-9116
Fax: (505) 844-3952
e-mail:sjbauer@sandia.gov

date: December 25, 2013

to: Lisa Mondy, 1512

from: S.J. Bauer, A. Urquhart, M. Hileman, 6914

Subject: **Foam and "solid" urethane thermal properties**

Abstract

Accurate knowledge of thermophysical properties of urethane foam is considered extremely important for meaningful models and analyses to be developed of scenarios wherein the foam is heated. Its performance at temperature requires a solid understanding material properties at temperature. Also, foam properties vary with density/porosity. An experimental program to determine the thermal properties of the two foams and their parent solid urethane was developed in order to support development of a predictive model relating density and theremal properties from first principles.

Thermal properties (thermal conductivity, diffusivity, and specific heat) of the foam were found to vary with temperatures from 26°C to 90°C. Thermal conductivity generally increases with increasing temperature for a given initial density and ranges from .0433 W/mK at 26°C to .0811 W/mK at 90°C; thermal diffusivity generally decreases with increasing temperature for a given initial density and ranges from .4101 mm^2/s at 26°C to .1263 mm^2/s at 90°C; and specific heat generally increases with increasing temperature for a given initial density and ranges from .1078 $/m^3K$ to .6323 $/m^3K$ at 90°C.

Thermal properties (thermal conductivity, diffusivity, and specific heat) of the solid urethane were also found to vary with temperatures from 26°C to 90°C. Average thermal conductivity generally increases with increasing temperature for a given initial density and ranges from 0.126 to 0.131 W/mK at 26°C to 0.153 to 0.157 W/mK at 90°C; average thermal diffusivity generally decreases with increasing temperature for a given initial density and ranges from 0.142 to 0.147 mm^2/s at 26°C to 0.124 to 0.125 mm^2/s at 90°C; and average specific heat generally increases with increasing temperature for a given initial density and ranges from 0.889 to 0.899 $/m^3K$ to 1.229 to 1.274 $/m^3K$ at 90°C.

Appendix

1. INTRODUCTION

Accurate knowledge of thermophysical properties of urethane foam is considered extremely important for meaningful models and analyses to be developed of scenarios wherein the foam is heated. Its performance at temperature requires a solid understanding material properties at temperature. Also, foam properties vary with density/porosity. An experimental program to determine the thermal properties of the two foams and their parent solid urethanes was developed in order to support development of a predictive model relating density and thermal properties from first principles.

Thermal conductivity, the property of a material to conduct heat, thermal diffusivity, the measure of thermal inertia, and the specific heat, the amount of heat per unit mass required to raise the temperature by one ^{o}C, were each determined in this stud. The operative mechanisms resulting in the observed changes of these thermal properties is beyond the scope of this study; minor aberrations in "smooth curves" obtained for most samples may be caused by changes for most of the data could be the result of experimental error and sample changes (chemical?) induced by heating the samples.

2. Sample Handling and Measurements

Thermal property measurements (thermal conductivity, diffusivity, and specific heat) were completed on a series of foam and urethane samples supplied by the sponsor.

Thermal measurements were made at ambient pressure and moisture conditions using a transient method based on the theory of the transient plane source technique, all property determinations were made with each measurement using the same apparatus, a Hot Disk Thermal Constants Analyzer (TCA). The apparatus employs a transient plane source device which is used to measure material thermal transport properties—thermal conductivity, thermal diffusivity and specific heat. The transient plane source method uses a plane sensor to function simultaneously as a heat source and resistance thermometer able to detect temperature changes as slight as 0.1 mK. The sensor is sandwiched between two samples of the material to be tested. Passing a current through the sensor increases its temperature by as much as a few degrees and causes a pulse of heat to enter the sample material. The ability of the sample material to conduct heat away from the sensor affects the temperature increase of the sensor. By monitoring the change in sensor temperature over time, therefore, the TCA system can deduce the thermal conductivity of the sample.

Using a nickel sensor embedded in a Kapton or mica coating, the TCA device used in this work (the ThermTest TPS1500 model) can make measurements from cryogenic temperatures to 1000K. The range of measurable thermal conductivities is 0.01–20 W/mK; the maximum measurable specific heat capacity is 5 MJ/m^{3}K. Samples can be

Appendix

as small as 3 mm in height by 13 mm in diameter, with no maximum limit. In addition to solids, measurements can be made in porous materials, powders and pastes.

The Hot Disk® sensors used for these measurements serve as a heat source to increase sample temperature and as resistance thermometers for recording temperature increase over time. The apparatus includes a programmable oven to house the sample and sensor portion of the test system, and a computer for data acquisition, data analysis, and program control (Figure 1).

Samples are heated from one temeperature to the next at 1-2 degrees C per minute and at each temperature the sample equilibrated for a few hours before a measurement was made. Measurements were made at room temperature and at specified temperature intervals up to 90°C.

The foam samples were supplied as paired discs of similar density. The solid urethane samples were supplied as cylinders, with a small amount of bubbles present, less at bottom, and a greater amount at the top. Solid urethane samples were carefully cut from cylinders of material supplied using a wire saw followed by abrasive paper, 2.0" diameter and 1" in length. The thermal measurement was made across a matched interface in each sample. Experience has it that a flat uniform surface to seat the sensor is important to obtaining reproducible measurements.

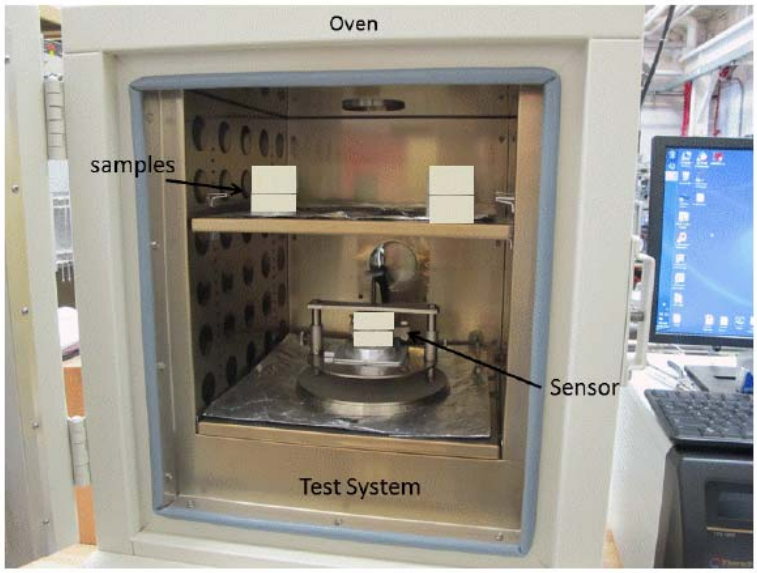

Figure 1 Thermal Measurements Test System.

Appendix

2.1 Porous Urethane Foam Sample and Thermophysical Property Measurements

The foam samples have lower density once the contact rind was removed from the flat surface; this post-grinding value is that used in subsequent presentations in this report (Table 1). Density of the foam samples ranges from 5.51 pcf to 25.94 pcf.

Thermal conductivity, thermal diffusivity and specific heat measurements are presented in Table 2. Each line of data represents that from a matched pair sample.

For a given sample (density) over the temperature range up to 90°C, thermal conductivity tends to increase, thermal diffusivity tends to decrease, and and specific heat tends to increase with increasing temperature, Figures 2, 3, and 4, respectively.

For a given measurement temperature, thermal conductivity tends to increase, thermal diffusivity tends to decrease, and and specific heat tends to increase with increasing temperature, Figures 5, 6, and 7, respectively.

	Initial						Post-grinding			
ID	Weight (g)	Diameter (in)	Height (in)	Volume (in^3)	Calc. density (pcf)	Noted density (pcf)	Weight (g)	Height (in)	Volume (in^3)	Calc. density (pcf)
44306-10	21.28	1.98	1.00	3.08	26.27	26.16	19.54	0.93	2.86	25.94
44306-10	21.13	1.99	1.02	3.17	25.32	25.21	19.15	0.94	2.92	24.90
44306-10	15.55	1.98	1.00	3.08	19.20	19.19	14.15	0.93	2.86	18.79
44306-10	15.69	1.99	1.02	3.17	18.80	18.83	14.04	0.93	2.89	18.45
44307-4	12.74	1.99	1.02	3.17	15.27	15.10	11.36	0.94	2.92	14.77
44307-4	10.63	1.99	1.00	3.11	12.99	12.90	9.26	0.89	2.77	12.72
44306-10	10.57	1.98	1.00	3.08	13.05	13.04	9.26	0.90	2.77	12.70
44306-10	10.32	1.99	1.02	3.17	12.37	12.41	9.10	0.93	2.89	11.96
44307-4	8.87	1.99	1.02	3.17	10.63	10.58	7.79	0.91	2.83	10.46
44307-4	7.40	1.99	1.00	3.11	9.04	9.08	5.94	0.83	2.58	8.75
44307-4	4.92	1.99	1.00	3.11	6.01	6.04	4.06	0.87	2.71	5.70
44307-4	4.91	1.99	1.02	3.17	5.88	5.85	3.88	0.86	2.67	5.51

Table 1. Sample dimensions and density determinations, porous foam.

Appendix

		Thermal conductivity (W/mK)			Thermal diffusivity (mm^2/s)			Specific heat (MJ/m^3K)		
ID	Calc. density (pcf)	26°C	60°C	90°C	26°C	60°C	90°C	26°C	60°C	90°C
44306-10	25.94	0.0743	0.0788	0.0799	0.1473	0.1396	0.1263	0.5046	0.5646	0.6323
44306-10	24.90	0.0741	0.0788	0.0811	0.1439	0.1385	0.1312	0.5147	0.5692	0.6180
44306-10	18.79	0.0656	0.0721	0.0735	0.1544	0.1661	0.1426	0.4250	0.4342	0.5153
44306-10	18.45	0.0658	0.0703	0.0734	0.1487	0.1503	0.1433	0.4422	0.4677	0.5121
44307-4	14.77	0.0518	0.0569	0.0606	0.1830	0.1816	0.1804	0.2830	0.3133	0.3361
44307-4	12.72	0.0534	0.0569	0.0603	0.1968	0.1796	0.1773	0.2713	0.3170	0.3398
44306-10	12.70	0.0541	0.0568	0.0615	0.1829	0.1793	0.1683	0.2958	0.3165	0.3654
44306-10	11.96	0.0541	0.0576	0.0614	0.1815	0.1723	0.1663	0.2983	0.3343	0.3694
44307-4	10.46	0.0479	0.0515	0.0552	0.2598	0.2443	0.2458	0.1844	0.2109	0.2244
44307-4	8.75	0.0481	0.0524	0.0549	0.2623	0.2548	0.2430	0.1833	0.2056	0.2258
44307-4	5.70	0.0442	0.0472	0.0507	0.4101	0.3742	0.3834	0.1078	0.1262	0.1323
44307-4	5.51	0.0433	0.0476	0.0506	0.3954	0.3791	0.3819	0.1095	0.1255	0.1325

Table 2. Thermal conductivity, thermal diffusivity, specific heat determinations, porous foam.

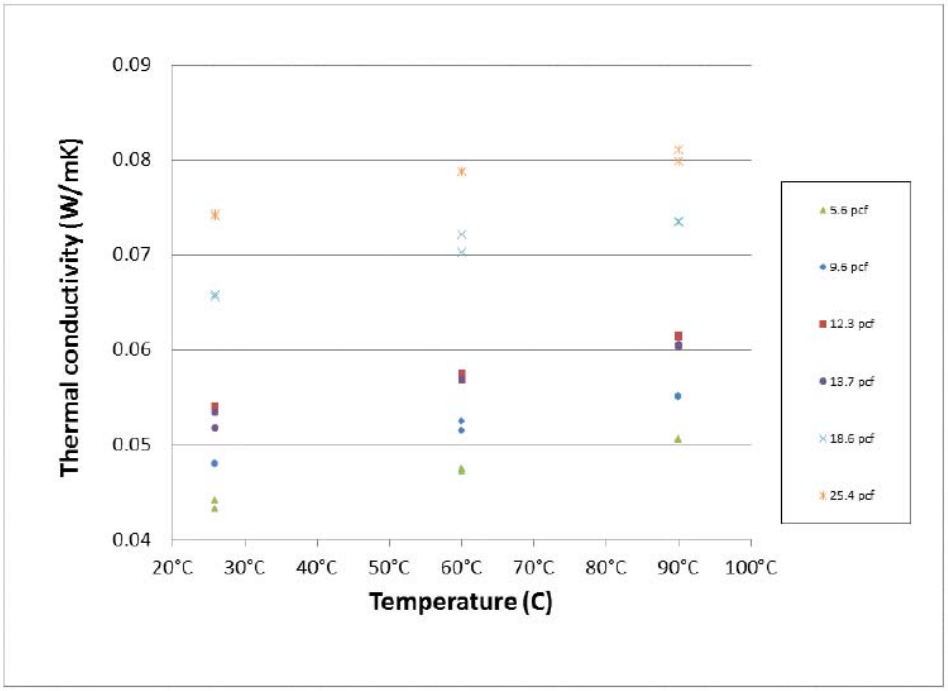

Figure 2. Thermal Conductivity vs temperature, porous urethane foam.

Appendix

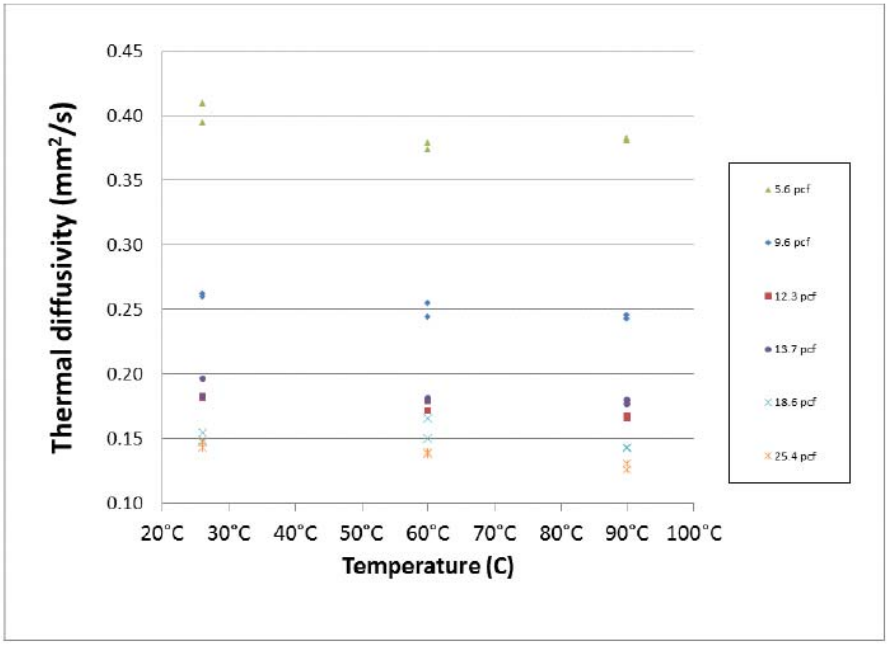

Figure 3. Thermal diffusivity vs temperature, porous urethane foam.

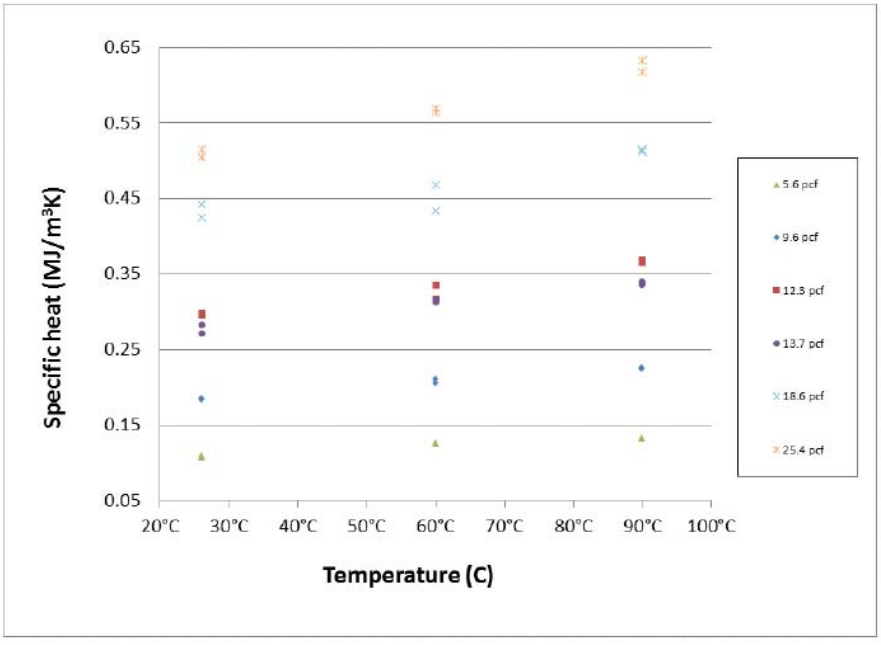

Figure 4. Specific heat vs temperature, porous urethane foam.

Appendix

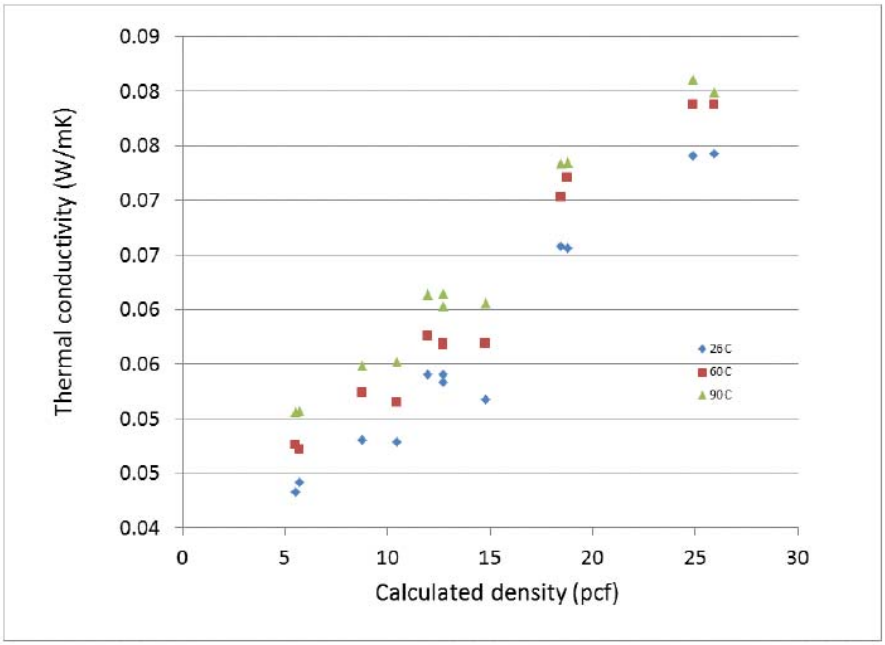

Figure 5. Thermal conductivity versus density, porous urethane foam.

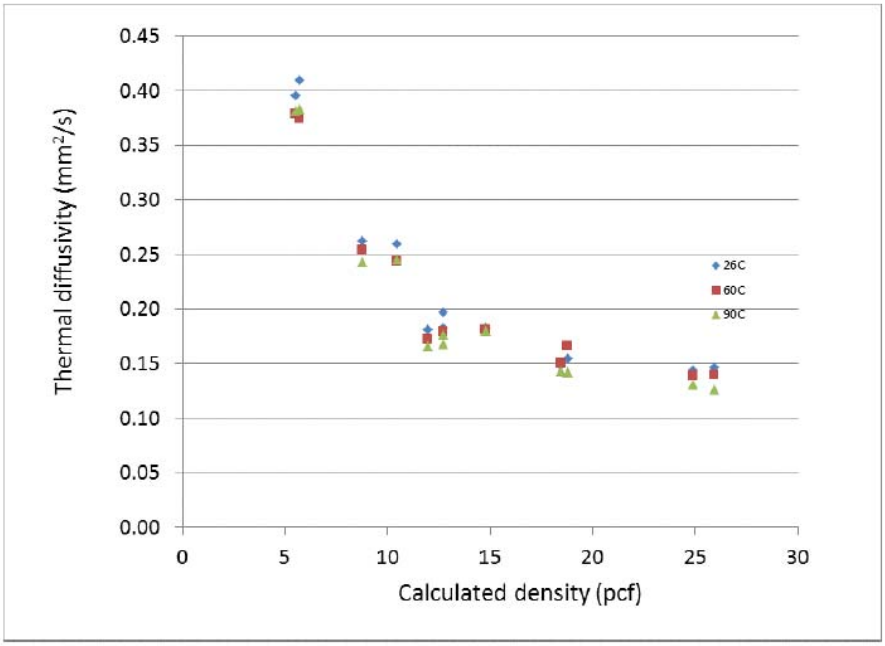

Figure 6. Thermal diffusivity versus density, porous urethane foam.

Appendix

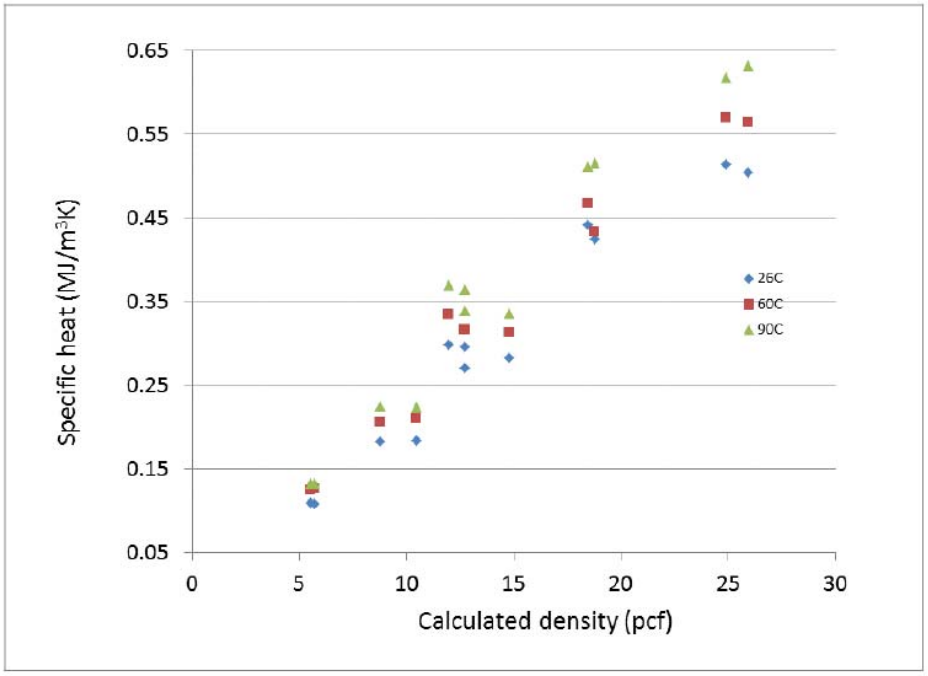

Figure 7. Specific Heat versus density, porous urethane foam.

Appendix

2.2 Solid Urethane Sample and Thermophysical Property Measurements

Results and Comments

Solid urethane sample discs are labeled for thermal analysis in Figure 8. For most sample/temperature combinations, four sets of thermal property measurements were taken and results are given in Tables 3, 4, and 5.

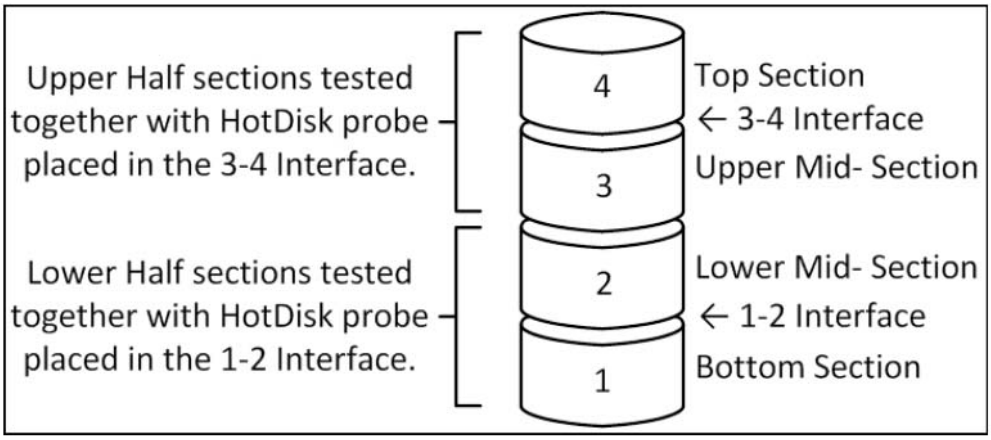

Figure 8. Schematic of sample layout

For a given sample set for both solid urethanes, (with similar initial density) over the temperature range up to 90°C, thermal conductivity tends to increase, thermal diffusivity tends to decrease, and and specific heat tends to increase with increasing temperature, Figures 9, 10, and 11, respectively. There is perhaps a plateau in the thermal diffuivity and specific heat data between 80°C and 90°C.

Thermal conductivity decreases with increasing density for both 44306 and 44307 urethanes, (Figure 12), thermal diffusivity increases with increasing density (Figure 13) and specific heat decreases with increasing density (Figure 14). Linear fits to the data are presented and appear reasonable approximations to the data set.

The measurement sets on 44306 urethane are more widely spaced than for the 44307 urethane. This may be rooted in the density variation versus temperature observed (Figure 15).The density of both urethanes tends to decrease with increasing temperature.

Appendix

3 Concluding Comments

In this study, the thermal properties of two samples each of two solid urethanes 44306 and 4430, and their foam product were measured with increasing temperature. Measurements on solid urethane may provide a data set for development of models to predict thermal properties foam equivalents as a function of temperature; Measurements on foamed urethane may provide a data set for validation of models to predict thermal properties urethane foams as a function of temperature. Time dependence, cycling versus single path increase, reproducibity for multiple samples was not considered.

Appendix

Table 3. 44306 and 44307 Solid Urethane Epoxy Sample Dimensions, Density

44306 Lower Half Data

Sample: 44306-1, Bottom section

Temp, °C	Diameter, in.	Thickness, in.	Mass, g	Density, pcf
25	1.988	1.013	54.288	65.64
40	1.992	1.014	54.297	65.32
50	1.992	1.013	54.279	65.36
60	1.993	1.015	54.256	65.14
70	1.994	1.016	54.269	65.03
80	1.995	1.016	54.222	64.90
90	1.995	1.016	54.178	64.85

Sample: 44306-2, Lower Mid-section

Diameter, in.	Thickness, in.	Mass, g	Density, pcf
1.984	1.051	55.058	64.42
1.992	1.058	55.071	63.49
1.989	1.054	55.051	63.90
1.989	1.054	55.031	63.88
1.990	1.056	55.044	63.71
1.990	1.056	54.995	63.65
1.991	1.055	54.952	63.60

44306 Upper Half

Sample: 44306-3, Upper Mid-section

Temp, °C	Diameter, in.	Thickness, in.	Mass, g	Density, pcf
25	1.987	1.056	54.994	63.85
40	1.990	1.059	55.006	63.49
50	1.989	1.059	54.984	63.53
60	1.990	1.059	54.963	63.44
70	1.992	1.060	54.976	63.27
80	1.992	1.061	54.926	63.15
90	1.993	1.059	54.879	63.15

Sample: 44306-4, Top Section

Diameter, in.	Thickness, in.	Mass, g	Density, pcf
1.987	1.024	53.232	63.73
1.991	1.026	53.244	63.37
1.990	1.025	53.222	63.47
1.991	1.026	53.203	63.32
1.993	1.028	53.214	63.08
1.993	1.028	53.164	63.02
1.994	1.028	53.12	62.91

44307 Lower Half Data

Sample: 44307-1, Bottom section

Temp, °C	Diameter, in.	Thickness, in.	Mass, g	Density, pcf
25	1.996	0.962	53.315	67.33
40	1.999	0.966	53.325	66.87
50	1.999	0.967	53.312	66.78
60	2.000	0.969	53.299	66.56
70	2.001	0.967	53.315	66.65
80	2.004	0.968	53.275	66.33
90	2.005	0.968	53.244	66.23

Sample: 44307-2, Lower Mid-section

Diameter, in.	Thickness, in.	Mass, g	Density, pcf
1.996	1.013	53.670	64.37
2.000	1.013	53.682	64.13
1.998	1.014	53.668	64.17
1.999	1.015	53.653	64.03
2.001	1.017	53.669	63.79
2.004	1.018	53.629	63.49
2.004	1.017	53.598	63.52

Sample: 44307-3, Upper Mid-section

Temp, °C	Diameter, in.	Thickness, in.	Mass, g	Density, pcf
25	1.996	1.033	54.148	63.69
40	1.999	1.037	54.161	63.26
50	1.999	1.035	54.144	63.37
60	2.000	1.036	54.130	63.23
70	2.001	1.038	54.150	63.06
80	2.004	1.039	54.105	62.76

Sample: 44307-4, Top Section

Diameter, in.	Thickness, in.	Mass, g	Density, pcf
1.995	1.033	51.643	60.80
2.000	1.037	51.656	60.28
1.999	1.038	51.638	60.26
2.000	1.040	51.624	60.07
2.000	1.038	51.642	60.20
2.004	1.040	51.595	59.79

Appendix

90	2.005	1.039	54.072	62.66		2.005	1.040	51.561	59.69

Table 4. 44306 Solid Urethane Thermal Property Determinations

Data Set 1
Interface Characteristics: 1-2

Temp, °C	TC, W/mK	TD, mm^2/s	SH, MJ/m^3K
25	0.1351	0.1570	0.8604
40	0.1170	0.1026	1.141
50	0.1329	0.1200	1.108
60	0.1399	0.1235	1.133
70	0.1433	0.1205	1.190
80	0.1474	0.1173	1.256
90	0.1515	0.1156	1.310

Data Set 2

Temp, °C	TC, W/mK	TD, mm^2/s	SH, MJ/m^3K
25	0.1221	0.1254	0.9738
40	0.1379	0.1419	0.9722
50	0.1379	0.1298	1.062
60	0.1442	0.1312	1.100
70	0.1494	0.1301	1.148
80	0.1524	0.1255	1.214
90	0.1608	0.1336	1.203

Data Set 3

Temp, °C	TC, W/mK	TD, mm^2/s	SH, MJ/m^3K
25	0.1299	0.1403	0.9262
40	0.1374	0.1402	0.9800
50	0.1408	0.1363	1.033
60	0.1453	0.1327	1.095
70	0.1488	0.1298	1.146
80	0.1536	0.1271	1.208
90	0.1618	0.1374	1.177

Data Set 4

Temp, °C	TC, W/mK	TD, mm^2/s	SH, MJ/m^3K
25	0.1330	0.1484	0.8959
40	0.1377	0.1397	0.9854
50	0.1409	0.1362	1.035
60	0.1456	0.1338	1.088
70	0.1496	0.1310	1.143
80	0.1526	0.1265	1.206
90	0.1616	0.1363	1.186

Data Set 1
Interface Characteristics: 3-4

Temp, °C	TC, W/mK	TD, mm^2/s	SH, MJ/m^3K
25	0.1255	0.1364	0.92
40	0.1295	0.1261	1.027
50	0.1396	0.1360	1.027
60	0.1379	0.1192	1.156
70	0.1365	0.1072	1.273
80	0.1471	0.1146	1.273
90	0.1525	0.1167	1.307

Data Set 2

Temp, °C	TC, W/mK	TD, mm^2/s	SH, MJ/m^3K
25	0.1373	0.1601	0.8581
40	0.1452	0.1590	0.913
50	0.1415	0.1345	1.052
60	0.1432	0.1296	1.105
70	0.1461	0.1247	1.172
80	0.1480	0.1170	1.265
90	0.1564	0.1216	1.286

Data Set 3

Temp, °C	TC, W/mK	TD, mm^2/s	SH, MJ/m^3K
25	0.1383	0.1636	0.8453
40	0.1387	0.1429	0.9711
50	0.1407	0.1351	1.041
60	0.1450	0.1314	1.103
70	0.1490	0.1290	1.155
80	0.1528	0.1252	1.220
90	0.1606	0.1330	1.208

Data Set 4

Temp, °C	TC, W/mK	TD, mm^2/s	SH, MJ/m^3K
25	0.1382	0.1634	0.8457
40	0.1368	0.1377	0.9939
50	0.1411	0.1327	1.063
60	0.1451	0.1326	1.095
70	0.1493	0.1297	1.151
80	0.1537	0.1271	1.210
90	0.1616	0.1344	1.203

Average of measurements

Average:	Density, pcf		Thermal Conductivity, W/mK		Thermal Diffusivity, mm^2/s		Specific Heat, MJ/m^3K	
Temp, °C	Lower	Upper	Lower	Upper	Lower	Upper	Lower	Upper
25	65.03	63.79	0.130	0.135	0.143	0.156	0.914	0.867
40	64.41	63.43	0.133	0.138	0.131	0.141	1.020	0.976
50	64.63	63.50	0.138	0.141	0.131	0.135	1.060	1.046
60	64.51	63.38	0.144	0.143	0.130	0.128	1.104	1.115
70	64.37	63.17	0.148	0.145	0.128	0.123	1.157	1.188
80	64.28	63.09	0.152	0.150	0.124	0.121	1.221	1.242
90	64.23	63.03	0.159	0.158	0.131	0.126	1.219	1.251

Appendix

Table 5. 44307 Solid Urethane Thermal Property Determinations

	Data Set 1 Interface Characteristics: 1-2			Data Set 2			Data Set 3			Data Set 4		
Temp, °C	TC, W/mK	TD, mm^2/s	SH, MJ/m^3K	TC, W/mK	TD, mm^2/s	SH, MJ/m^3K	TC, W/mK	TD, mm^2/s	SH, MJ/m^3K	TC, W/mK	TD, mm^2/s	SH, MJ/m^3K
25	0.1321	0.1698	0.7782	0.1323	0.1441	0.9183	0.1257	0.1256	1.001	0.1334	0.1488	0.8965
40	0.1370	0.1408	0.9731	0.1470	0.1579	0.9308	0.1407	0.1423	0.9887	0.1397	0.1402	0.9966
50	0.1415	0.1374	1.030	0.1448	0.1400	1.034	0.1436	0.1368	1.050	0.1431	0.1364	1.049
60	0.1404	0.1207	1.163	0.1461	0.1318	1.108	0.1471	0.1339	1.099	0.1365	0.1104	1.237
70	0.1412	0.1125	1.255	0.1495	0.1274	1.174	0.1517	0.1320	1.149	0.1526	0.1328	1.149
80	0.1397	0.0963	1.450	0.1495	0.1181	1.266	0.1550	0.1278	1.213	0.1558	0.1289	1.209
90	0.1523	0.1136	1.341	0.1532	0.1165	1.316	0.1613	0.1316	1.225	0.1624	0.1338	1.213

	Data Set 1 Interface Characteristics: 3-4			Data Set 2			Data Set 3			Data Set 4		
Temp, °C	TC, W/mK	TD, mm^2/s	SH, MJ/m^3K	TC, W/mK	TD, mm^2/s	SH, MJ/m^3K	TC, W/mK	TD, mm^2/s	SH, MJ/m^3K	TC, W/mK	TD, mm^2/s	SH, MJ/m^3K
25	0.1230	0.1347	0.9133	0.1264	0.1425	0.8867	0.1270	0.1441	0.8813	0.1280	0.1464	0.8738
40	0.1263	0.1229	1.028	0.1314	0.1321	0.9947	0.1330	0.1363	0.9753	0.1337	0.1366	0.9786
50	0.1362	0.1352	1.007	0.1390	0.1383	1.005	0.1376	0.1356	1.015	0.1377	0.1349	1.021
60	0.1363	0.1223	1.114	0.1403	0.1302	1.078	0.1417	0.1335	1.062	0.1421	0.1330	1.068
70	0.1505	0.1398	1.076	0.1457	0.1304	1.117	0.1450	0.1292	1.122	0.1448	0.1280	1.132
80	0.1369	0.1049	1.306	0.1449	0.1198	1.210	0.1483	0.1269	1.169	0.1495	0.1292	1.157
90	0.1501	0.1188	1.264	0.1504	0.1188	1.265	0.1549	0.1286	1.205	0.1567	0.1328	1.180

Average of measurements

Average:	Density, pcf		Thermal Conductivity, W/mK		Thermal Diffusivity, mm^2/s		Specific Heat, MJ/m^3K	
Temp, °C	Lower	Upper	Lower	Upper	Lower	Upper	Lower	Upper
25	65.85	62.24	0.131	0.126	0.147	0.142	0.899	0.889
40	65.50	61.77	0.141	0.131	0.145	0.132	0.972	0.994
50	65.48	61.81	0.143	0.138	0.138	0.136	1.041	1.012
60	65.29	61.65	0.143	0.140	0.124	0.130	1.152	1.081
70	65.22	61.63	0.149	0.147	0.126	0.132	1.182	1.112
80	64.91	61.28	0.150	0.145	0.118	0.120	1.285	1.211
90	64.87	61.18	0.157	0.153	0.124	0.125	1.274	1.229

Appendix

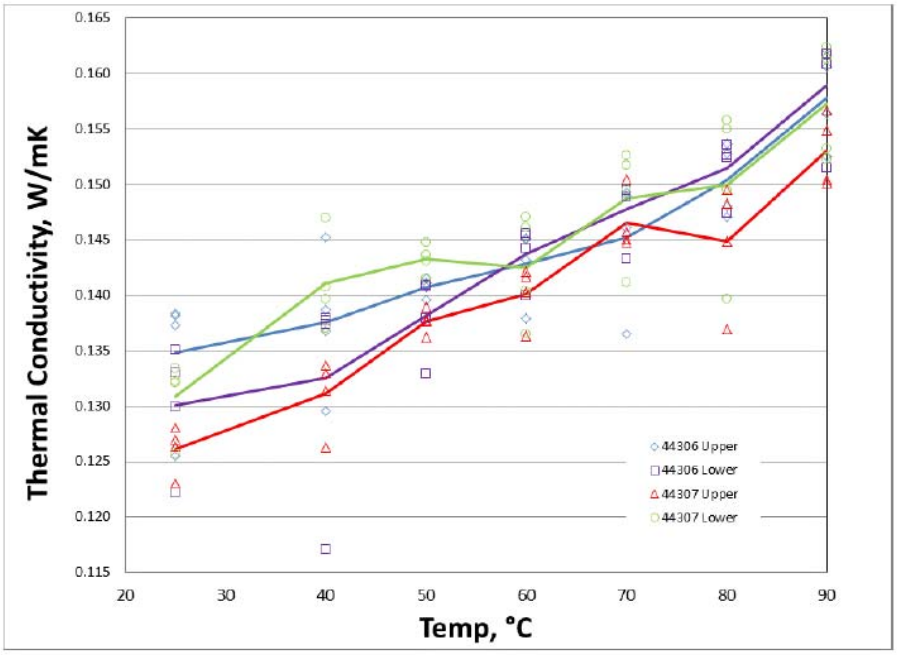

Figure 9. Thermal Conductivity vs temperature, solid urethane

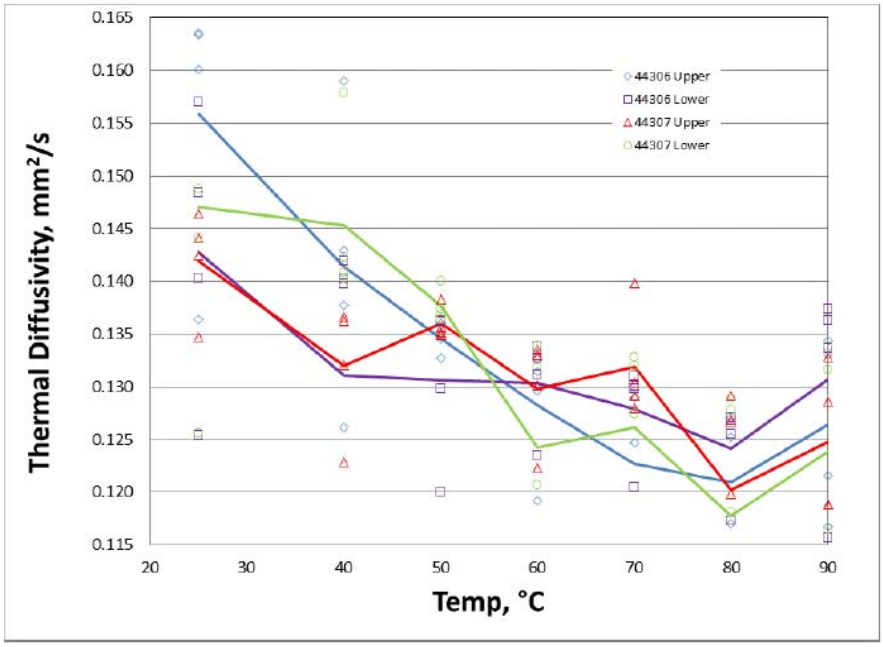

Figure 10. Thermal diffusivity vs temperature, solid urethane

Appendix

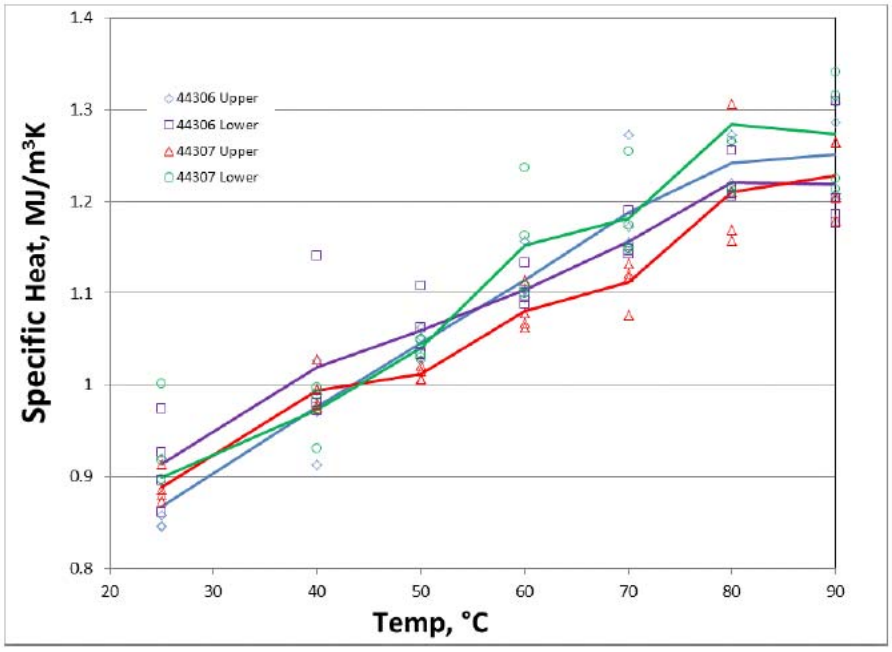

Figure 11. Specific heat vs temperature, solid urethane

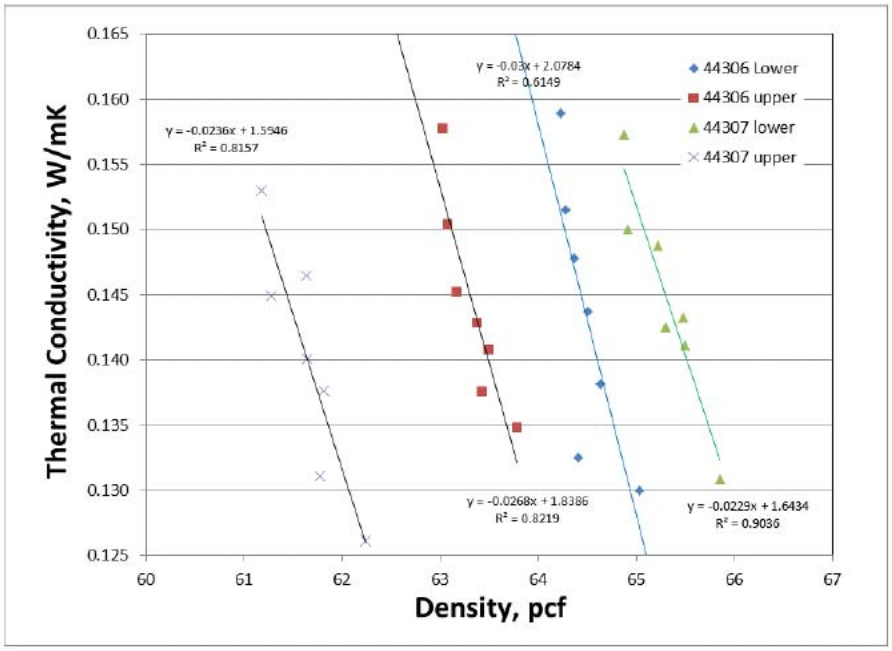

Figure 12. Thermal conductivity versus density, solid urethane

Appendix

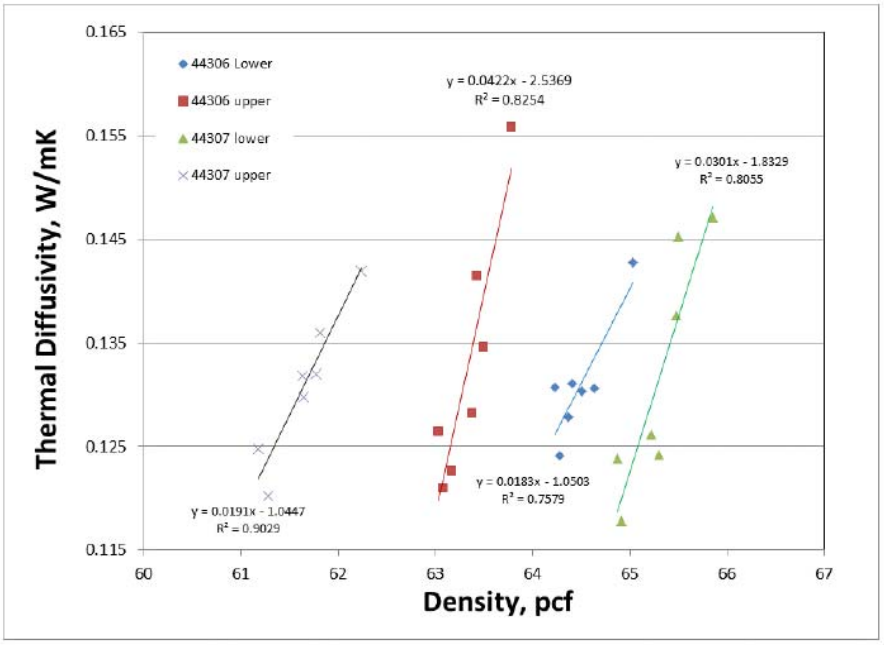

Figure 13. Thermal diffusivity versus density, solid urethane

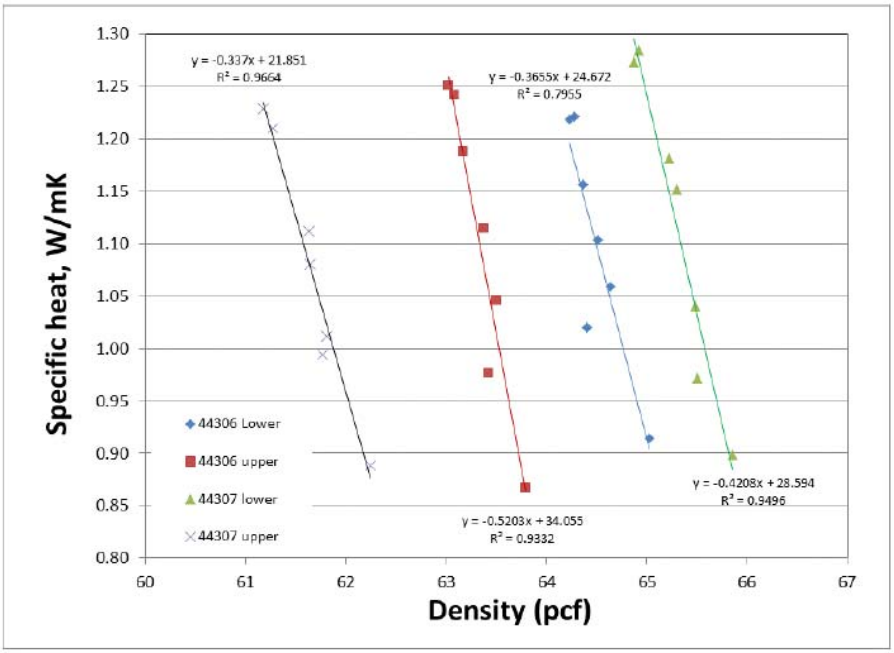

Figure 14. Specific Heat versus density, solid urethane

Appendix

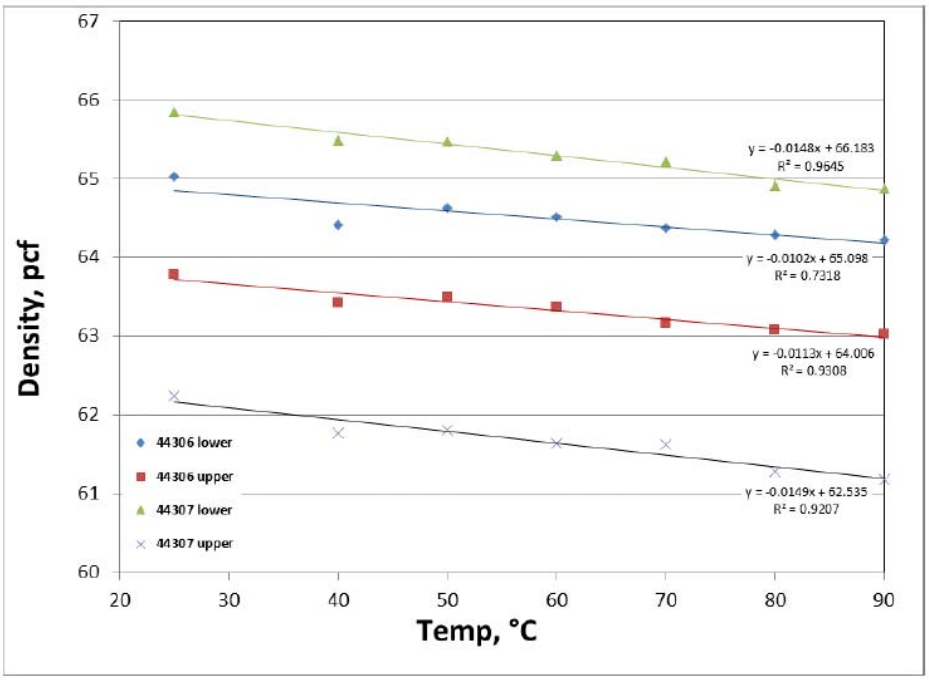

Figure 15. Density versus temperature, solid urethane

Copy to:

M. Lee 6914

DISTRIBUTION (ELECTRONIC COPIES)

1	MS0899	Technical Library	9536
1	MS0161	Legal Technology Transfer Center	11500
1	MS0346	Lisa Mondy	1512
1	MS0346	Christine Roberts	1512
1	MS0346	Anne Grillet	1512
1	MS0346	Melissa Soehnel	1512
1	MS0346	Tracie Durbin	1512
1	MS0382	Shayna Begay	2153
1	MS0382	Heather Boldt	2153
1	MS0386	Joe Fonseca	2128
1	MS0555	Kyle Thompson	1522
1	MS0807	David Michael Smith	9328
1	MS0836	Timothy O'Hern	1512
1	MS0836	Bion Shelden	1512
1	MS0836	Rekha Rao	1514
1	MS0836	Daniel Rader	1514
1	MS0888	Edward Russick	1833
1	MS0888	James McElhanon	1835
1	MS9042	Amanda Dodd	8365
1	MS9403	LeRoy Whinnery	8223
1	MS0958	Nicholas Wyatt	1835
1	MS1033	Stephen Bauer	6914

1	MS1033	Michael Hileman	6914
1	MS1033	M. Lee	6914
1	MS1411	Mat Celina	1819

External:
James Tinsley, NNSA's Kansas City Plant Operated by Honeywell Federal Manufacturing & Technologies, LLC, D/891 Advanced Engineering Simulations & Analysis, Kansas City, Mo.


Sandia National Laboratories